2015

New developments in magneto-optic interferometric switching

John William Pritchard
Iowa State University

New developments in magneto-optic interferometric switching

by

John W. Pritchard

A dissertation submitted to the graduate faculty
in partial fulfillment of the requirements for the degree of

DOCTOR OF PHILOSOPHY

Major: Electrical Engineering

Program of Study Committee:
Mani Mina, Co-Major Professor
Jiming Song, Co-Major Professor
Robert J. Weber
David Jiles
James Cochran

Iowa State University

Ames, Iowa

2015

"Logic will get you from A to B. Imagination will take you everywhere."

- Albert Einstein

COPYRIGHT

DEDICATION

To my family, my mentors, and all those who supported my ambitions and dreams.

TABLE OF CONTENTS

Page

LIST OF FIGURES

LIST OF TABLES

ABSTRACT

In the next few decades, it is likely that high bandwidth wireless and optical technologies will be placed in the spotlight as the dominant avenues for communication all over the world. It is arguable that this is currently the case, and that the expectation for higher data transfer speeds, more secure and reliable transmission, and longer communication range is on an exponential rise. Thus, much effort and emphasis is being put on these technologies to advance as quickly as possible.

For optical systems, the majority of research has been focused on the realization of all-optical transmission, that is, transmission such that no energy conversions (e.g. optical-electrical) take place in the transmission process. In many cases this has been achieved utilizing electro-optic (EO) and magneto-optic (MO) phenomena in special materials. Here, the use of interferometric techniques can enable optical switching and routing with the help of applied electric or magnetic fields to the special materials as light traverses through them.

There are many challenges in the design of these switches. For magneto-optic interferometric devices, the magnetic field generator tends to be quite large compared to the optical transceivers deployed today. Due to their large size, current and voltage requirements tend to be excessive as well. It is important to continue to reduce the size and power requirement of these devices to ensure compatibility with current systems.

In this work, new improvements to the magnetic field generators and new configurations of MO interferometric switches and routers are proposed and implemented. Additionally, studies toward a monolithically integrated MO switch are presented which include preliminary design and simulation of on-chip rib waveguides, couplers, and magnetic field generators at the micron scale.

CHAPTER 1
INTRODUCTION

Modified from the paper published in *Magnetics Technology International Magazine*

John W. Pritchard and Mani Mina

Imagine, for the sake of a thought experiment, that you are sometime in the near future at your laptop computer, in the comfort of your own home. Data communication has advanced greatly. Instead of plugging in those familiar copper wires to get online, you connect your optical patch cable from a spare port on your router directly to your laptop. Your speed test peaks at multiple terabits per second, and your satisfaction is achieved when your favorite series of video lectures is downloaded in mere seconds. This is the dream that engineers and physicists are pushing to realize. However, this dream does not end at your home.

1.1 Background and Motivation

Many applications in engineering have solutions that involve complicated systems. As technologies are refined over the years, we repeat (or copy) fundamental designs to prevent “reinventing the wheel” and make it easier to build even more complicated systems. This is common throughout many efforts in human invention, and enables fast development of technologies [1]. In such inventions involving electricity and magnetism, systems can acquire and generate information. Often times, multiple systems need to exchange this information with each other to work well. As the fundamental designs are tuned and refined, it is important that the transmission and reception of the generated or acquired information is refined as well. These tasks may

not be done in parallel, which tends to create bottlenecks in the complicated systems. However, once both are refined, the entire system becomes a fundamental design, and new technologies are born.

The process of technological development is not new, but as discoveries are made the details change, and these fundamental designs may be replaced by completely different ones that are improved by orders of magnitude. This is the case with the replacement of wire-based communication systems by fiber-based systems. However, the replacement process is not seamless. There is currently a mix of wire- and fiber-based systems. Thus, the exchange of information between systems may require a conversion between transmission media. For fast, long-distance communication, optical communication technologies are currently the best choice. However, end-user systems convert the optical information to electronic so machine-to-machine (M2M) communication is achieved. This conversion is currently a bottleneck because electrical systems are not able to match the bandwidth capability of their optical counterparts. Therefore, it is of great interest in the research community to reduce this bottleneck and provide an all-optical platform for communication [2] [3] [4].

1.2 Challenges in Optical Communications

Optical communication is one of the oldest forms of long distance communication technologies and is a rapidly advancing field. From smoke signals to light houses to visual Morse code to wavelength-division multiplexing (WDM), optical communication predates the middle ages and is still ever present. With the invention of silica optical fiber as the propagation medium for light and with the invention of integrated circuit technology, advanced multiplexing techniques could be utilized and higher bandwidth systems could be achieved. Furthermore, with the advancement of material purification techniques, low loss fiber (less than 0.1dB/km) was invented and optical communication became the leading low-loss, high-speed data communication technology [2].

For such high speed communication platforms, encoding and decoding the signals has always been some of the main challenges. Small changes in optical signals need to be preserved and interpreted to provide the users cutting edge capabilities. In order to improve the speed the challenge is to not change the communication media and stay in the all-optical platform, however there are several ways of achieving this [4]. One of the most exciting approaches for such information encoding and decoding is via interferometric methods. Such methods mix light waves and allow for the creation and extraction of vital information. These interferometers serve as the building blocks for the advanced optical transceivers of tomorrow.

The optical-electrical-optical (OEO) interface (Figure 1.1) remains the major bandwidth bottleneck of optical communication networks. To reduce the effects of the OEO interface, the currently deployed electronic transceivers are to be replaced by all-optical ones [5] [6], which can be built from combinations of interferometric modulators. Other types of all-optical systems have been proposed, but are becoming less dominant due to manufacturing efforts and long term reliability [7].

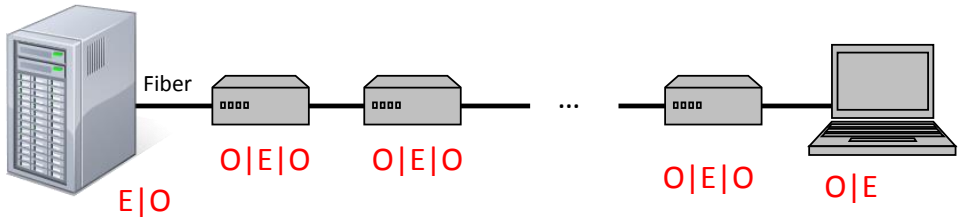

Figure 1.1: Simplified fiber-optic networking showing OEO interfaces.

1.3 Interferometry and All-Optical Switches

Traditionally, interferometers are used to study the properties of materials placed in an optical path of the interferometer. Interferometers can allow one to observe how light interferes, which, in many cases, is due to changes in the state of polarization (SoP) of the light (which is usually referred to as the direction of the electric part of the optical wave) [8]. The rotation of the SoP of an incoming wave of

light can be caused by reflection on (optical Kerr effect) or transmission through (optical Faraday effect) the material. Based on the resulting interference pattern, material properties can be determined. Similarly, by changing the properties of the material the interference pattern can be modified. This concept of manipulating the properties of materials to observe different interference patterns serves as the basis for all-optical switching.

Many all-optical switches of interferometer design utilize the Faraday effect. However, different interferometer configurations can be used. Popular interferometer configurations include the Mach-Zhender, Sagnac, and Resonator (Figure 1.2). Although others would suffice, these have shown to be best suited for switching applications [9] [10].

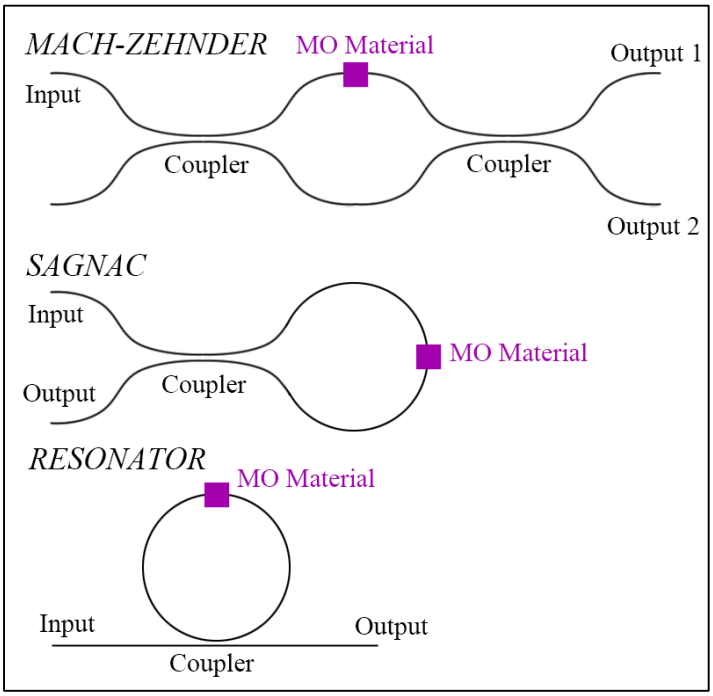

Figure 1.2: Mach-Zehnder (top), Sagnac (center), and resonator (bottom) interferometer configurations

All three configurations utilize a material that exhibit the Faraday effect to create a phase difference between propagating waves and cause constructive or destructive interference. The manner in which this is done make each configuration

unique. The Mach-Zhender uses a coupler to split an incoming signal, rotate the SoP of one, and then combine the signals with a second coupler to create interference at the output. The Sagnac uses one coupler that splits an incoming signal, each signal's SoP is then specially rotated, the signals re-enter the same coupler and interfere at the output [11]. The resonator uses a coupler to couple light onto a ring-resonating path which builds in amplitude, is delayed with respect to the incoming signal due to the loop path travelled, and thus creates interference at the output [12].

Two types of the Faraday effect can be used to achieve all-optical switching. The electro-optic (EO) Faraday effect causes a rotation in the SoP of light due to an applied electric field, and the MO Faraday effect utilizes an applied magnetic field to cause Faraday rotation. Currently, EO devices dominate all-optical switching in industry. However, with the increasing need for low-cost, low-power systems, MO devices are showing to be a sensible alternative. To realize this, a couple of the most important hurdles that need to be overcome are the inclusion of the MO Faraday rotator (MOFR) and the optimization of the magnetic field generator (MFG).

The MFG is generally a coil wrapped around the MOFR, and an electronic driver circuit supplies current to create the required field. The flux density for a single coil can then be approximated to be [13]

$$B \approx \frac{\mu_0 NI}{\sqrt{l^2+4R^2}} \qquad (1.1)$$

where μ_0 is the permeability of free space, N is the number of coil turns, I is the current through the coil, l is the length of the coil, and R is the coil radius. For fiber-based designs, the inclusion of the MOFR is relatively simple. A small slab of the material can be placed between the two fiber patch cables with index matching gel at the interfaces. The MFG can then be a coil wrapped around a fiber guiding sleeve (Figure 1.3). For silicon-based devices, it is not so simple. Special techniques are required to include suitable MO material such that monolithic integration is achieved.

This affects fabrication capabilities. However, recent advancements in the design of integrated optical isolators have shown significant progress [14].

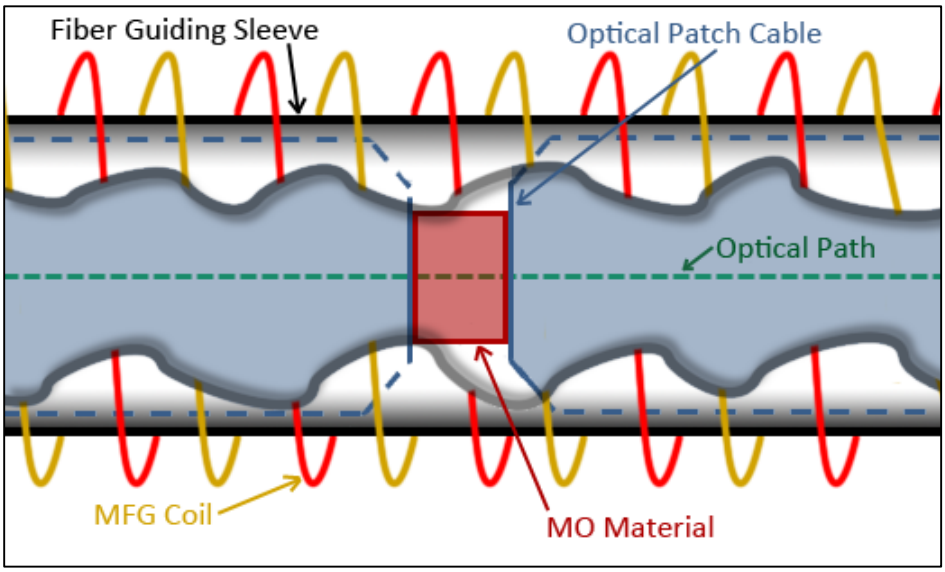

Figure 1.3: Cross section of inserted MO material in a fiber-based system

The MFG for fiber-based systems is relatively simple, but is not as fast as desired. Commercial devices can achieve optical pulse widths on the order of 10 microseconds, and recent works have shown pulse widths achieved near 150 nanoseconds [15]. Yet, the complimentary EO devices can achieve pulse widths less than 1 nanosecond. While there are theoretical limits that may not allow MO devices to reach 1 nanosecond pulse width, with the monolithic integration of an MO switch the magnetic domain switching limit can be approached (within an order of magnitude compared to EO switches) and these switches can be more useful.

Each type of switch has different a role in the optical communication network. EO switches are advantageous in their ability to perform processing and "bit banging" operations – tasks that require very high switching speed mechanisms [16]. However, it is common in optical networks to require signal routing schemes and dynamic optical isolation as well. These schemes do not need very fast switching speeds, but instead require "on" and "off" times to be relatively long. In this case, MO switches that utilize

hard magnetic materials can be used as a low-power solution. A hard ferrite will “latch” its magnetization direction to the direction of the applied field. This can be used to create an MO switch that can define a signal path and latch to the path for a long period of time without the continued presence of a magnetic field. If an EO switch was used in this way, the electric field would need to be present the entire time the signal path was defined, dissipating a lot of power in the process. The power-saving feature of an MO switch can directly translate to a cost-saving feature (since power requires money), but this is only advantageous if the money saved can match the cost to manufacture such a switch.

1.4 Toward a Monolithically Integrated Magneto-Optic Modulator

It is a continued effort to properly include MO material on silicon-based devices to realize a monolithically integrated MO switch (Figure 1.4). Commercial fiber-based devices with MO material have been developed, but their resulting size does not allow for large scalability. With the monolithic integration of a MOFR on silicon, the potential for fully integrated and efficient all-optical systems on a chip (SoC) can be realized. One of the main challenges in monolithically integrating a MOFR on silicon has been in matching the crystal structure of the MO material to silicon’s. In theory, this can be done by annealing the device after MO material deposition. However, the annealing temperature required for such a task results in the optical waveguide experiencing exceedingly high optical absorption properties. In recent works, this has shown to be resolved by employing special pulsed laser deposition (PLD) techniques [14]. Once these processes have been refined and adapted to standardized CMOS processing, the next step is to implement an integrated MFG.

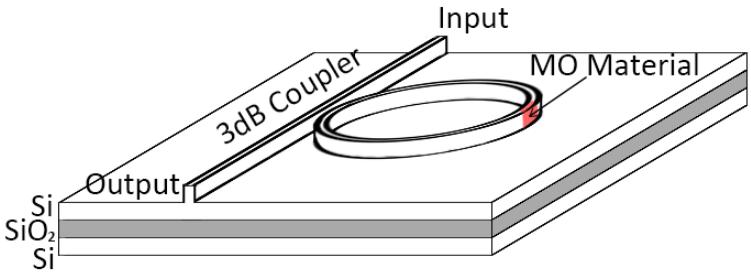

Figure 1.4: Concept integrated MO interferometric switch of resonator configuration

On-silicon, high-amplitude MFGs oriented transverse to the silicon wafer plane have not been studied extensively. In-plane coils have been designed and implemented quite often in RF systems, however the fields generated (or received) are generally smaller than that required to achieve sufficient Faraday rotation. Thus, it is of interest to design a transverse-plane MFG that is suitable for MO switching applications. If the silicon-on-insulator (SOI) platform using rib waveguides is chosen as the optical propagation technology, then the coil would likely be of square geometry (Figure 1.5). The field through such a coil may be approximated by assuming circular geometry and using Equation 1.1.

Figure 1.5: Example of a solenoid of rectangular geometry

The research and development on the monolithic integration of MO technologies will open doors to new topics of interest, furthering our knowledge of the intimate relationship between light and magnetism. In addition, pursuing challenges of MFGs of such small form-factor will help us better understand domain dynamics and how to utilize them on a microscopic scale to create more interesting devices.

1.5 Conclusion

The main goal in this work is to understand the challenges faced by MO switch or router designers, and offer solutions that enhances these devices from an efficiency, switching speed, and responsivity perspective through research, exploration, and discovery.

The efforts required to create fiber-based magneto-optic (MO) interferometric switches and routers include determining and implementing the appropriate:

1. Laser source and detection equipment
2. Interferometer configuration
3. Magneto-optic material
4. Magnetic field generation circuitry (switching technology and coil)

In this work, the laser source and detection equipment have operating wavelengths of 1550 nm. This wavelength was chosen for its wide use in communication networks (due to its low-loss characteristics in silica fiber). The other three points must then be tailored to operate at 1550 nm as well.

Three different optical interferometer configurations were explored: the Mach-Zehnder, Sagnac, and Resonator. The Sagnac and Resonator have experimental data reported, and the Mach-Zehnder is presented analytically. These interferometers were studied in both switching and routing applications.

Two magneto-optic materials were investigated, one of low-moment type and the other of latching type. These thick film materials were fabricated at and purchased from Integrated Photonics Inc.

Finally, many different ways of magnetizing the MO material were explored and reported, which make up the core contributions of this work. This exploration resulted in different circuit topologies, coil configurations, and has been recognized as a valuable endeavor by other academic institutions, in particular Toyohashi University of

Technology in Aichi, Toyohashi, Japan. This relationship which produced an MFG product is described in Appendix A.

CHAPTER 2

MAGNETO-OPTIC INTERFEROMETRIC SWITCHING AND ROUTING

The main activities in this work include using fiber-optic components with magneto-optic materials and electronic circuitry to create all-optical switches and routers. It is important to differentiate between the switches and routers, although they are related. This chapter describes each and discusses the specific optical components and systems required to realize them.

2.1 Switches, Routers, and Interferometers

Optical switches are devices that turn light on or off (Figure 2.1, left). Routers are devices that redefine the path of an optical signal (Figure 2.1, right). There are many ways to achieve optical switching and routing. One common method to create an optical switch is to periodically provide physical obstructions in the path of the light. A common method to create an optical router is to provide some form of reflection to change the optical path (e.g. tilted mirrors). Each of these methods have drawbacks, usually because the switching or routing entities are mechanical in nature. Interferometers are advantageous as they utilize the interactions between electromagnetic waves and specially designed transmission media to create switching and routing effects without classical mechanical devices.

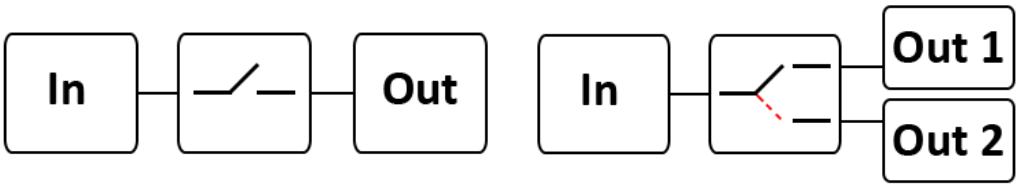

Figure 2.1: Basic diagram illustrating a switch (left) and a router (right)

In general, an interferometer is a device that is used to combine electromagnetic waves resulting in their constructive or destructive interference at the

output (Figure 2.2). For optical networking devices, this phenomenon can be represented by a systems-level diagram (Figure 2.3). Adding phase shifting elements to this system in one of the optical paths allows for control of the interference (Figure 2.4).

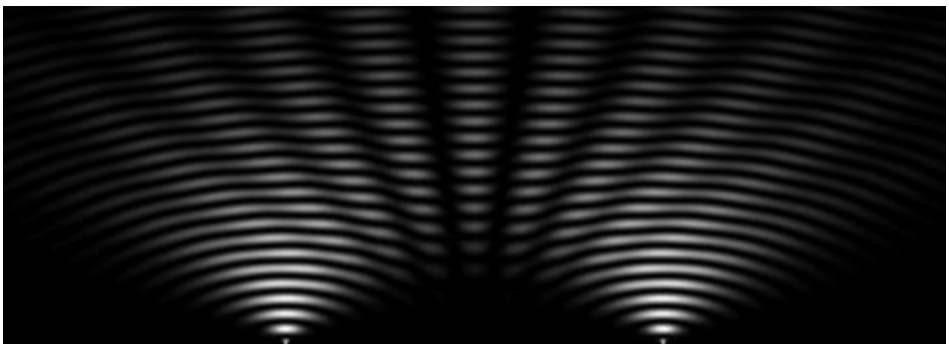

Figure 2.2: Interference pattern from two point sources [17]

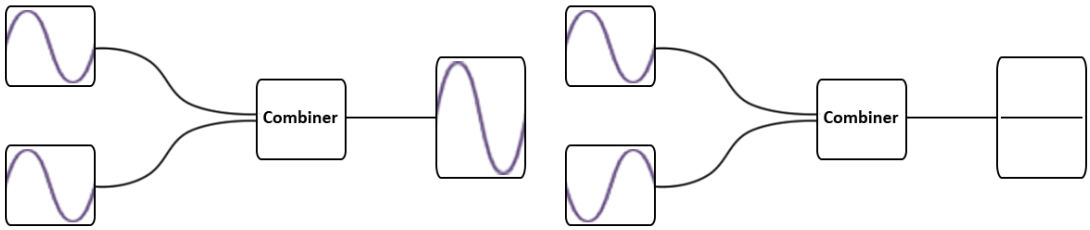

Figure 2.3: Systems level diagram of interferometer showing constructive interference due to in-phase waves (left) and destructive interference due to waves 180° out of phase (right).

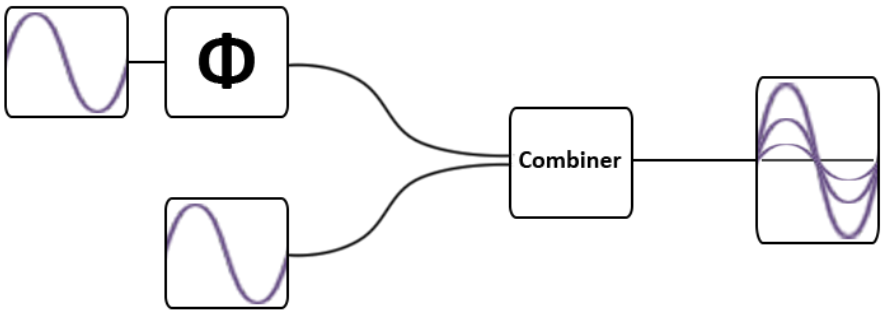

Figure 2.4: Systems level diagram of interferometer showing variable interference depending on the state of the phase shifting element Φ.

These systems illustrate the fundamental concepts that are at the core of the work presented in this dissertation. Each block in the diagrams has an equivalent optical component associated with it. The following sections will discuss the specific optical components needed to realize interferometers, and special focus will be put on the different types of interferometers and magneto-optic materials (phase-shifting elements).

2.2 Fundamental Components

Some of the main components required to create a fiber-optic switch or router using interferometry include a laser, coupler, isolator, circulator, and phase-shifting element (magneto-optic material).

A laser (light amplification by stimulated emission of radiation) is a source of electromagnetic radiation with good coherence and a narrow spectral width. Coherence can be defined as the measure of how constant the phase difference is between two optical signals (of the same frequency). Good coherence means the phase between two signals is relatively constant. This is a very useful property in interferometric switches and routers since obtaining stable output requires relatively constant phase (or, good coherence).

Couplers are devices that combine or split EM waves (this is represented by the "combiner" block in Figure 2.3 and Figure 2.4). They can take many forms, but often times in optical systems couplers are four port devices consisting of waveguides that converge with a very small space in-between (e.g. Figure 2.5). A 90° phase shift is introduced to the coupled signal, and the "through signal" experiences no change in phase. For example, a signal that enters a 3 dB coupler results in two signals at the output "arms," one with half the input power having 0° phase shift and one at the coupled output also with half the input power but now having a 90° shift in phase relative to the input. A device with such properties can be useful in combining phase shifted signals to provide meaningful output.

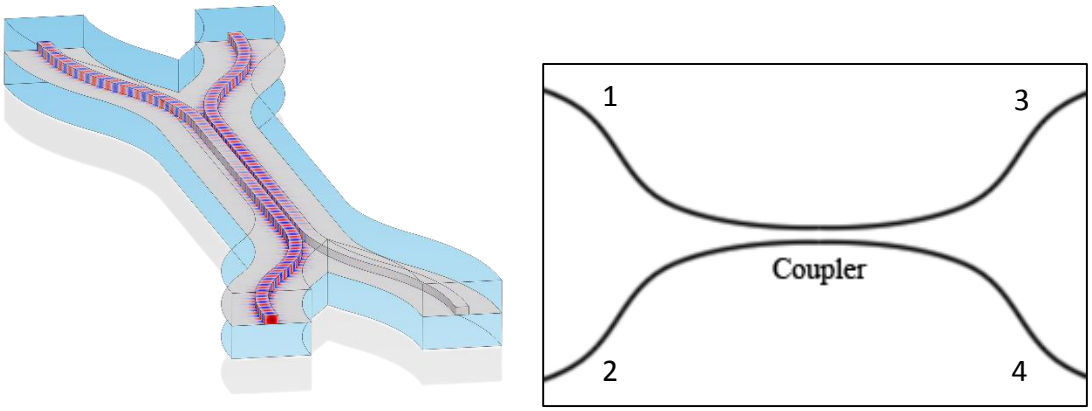

Figure 2.5: 3D illustration of an on-chip coupler [18] (left) and schematic representation (right)

Another unique and useful device is the circulator. Circulators are three-port devices that are able to "circulate" signals from port to port. For example, an EM wave entering port 1 is circulated to port 2. An EM wave entering port 2 is circulated to port 3 (terminated at port 1). This is made possible by using nonreciprocal materials to reroute the signals (Figure 2.6). Additionally, a circulator can be used as an isolator, a device that allows an EM wave to propagate in only one direction. If port 3 were to be terminated, the only path that is able to be circulated is from port 1 to port 2.

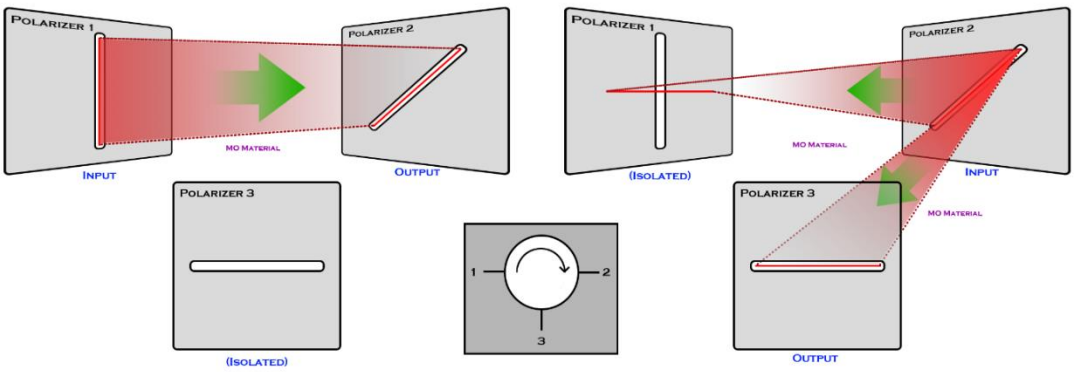

Figure 2.6: Illustration of a linearly polarized wave being passively routed in a circulator from port 1 to 2 (left) and port 2 to 3 (right) with the schematic symbol shown (middle)

Phase shifting elements can be used in these systems to offer even more flexibility. One passive phase shifting element is the delay line, an elongated optical waveguide that can introduce a shift in phase relative to a short waveguide, due to the difference in time it takes to complete the path traveled (Figure 2.7, left). An active phase shifting element could be an electro-optic or magneto-optic material (Figure 2.7, right). The material can rotate the input signal's state of polarization which, when combined with another signal at a coupler, has a similar effect as a phase shift. These materials are advantageous as their feature size can be much smaller than passive phase shifters. For example, an in-fiber delay line can be on the order of several meters long whereas a magneto-optic material can be on the order of millimeters in length. The magneto-optic material is one of the key elements in these interferometers that enables all-optical switching and routing.

Figure 2.7: Commercial fiber-optic delay line [19] (left) and magneto-optic material [20] (right)

2.3 Magneto-Optic Material

At the heart of the magneto-optic interferometric switches and routers used in this work is the magneto-optic material. Thus, a discussion of what the material is and how it works is warranted. The purpose of this section is to describe what MO material is, how it interacts with light, and why that interaction is important for these experiments. A few of the main topics that arise when dealing with MO materials in interferometric switching include what type of magnetic material is best suited for

magneto-optic applications, what the optical input and output characteristics of the material are, and how the interaction between light and the MO material occurs. This requires a discussion of ferrites, the Faraday effect, and the origin of Faraday rotation.

2.3.1 Ferrites

The MO materials used throughout this work are ferrites, special ferrimagnetic materials with high specific Faraday rotations (rotation of the plane of polarization of an electromagnetic wave per unit length). All ferrimagnetic materials exhibit this property, but the ferrites have very strong interactions compared to others. This makes them important for the design of microwave and optical devices.

Ferrimagnetism is a phenomenon seen in ferrites in which neighboring magnetic moments are oriented antiparallel and have different magnitudes, thus resulting in a net magnetization of the bulk material (Figure 2.8). The difference in magnitude of neighboring moments (which differentiates ferrimagnetism from antiferromagnetism) is a result of indirect coupling of neighboring metallic ions. In most ferrimagnetic oxides, the indirect coupling is a result of negatively charged oxygen ions separating the metallic ions. The coupling is indirect because the distance between the two metallic ions is great enough, due to the oxygen ion in-between, that direct exchange is not appreciable. In these cases, the magnetic order results from various complicated exchange mechanisms (indirect exchange interaction) in which the intermediate ions play a significant role. These mechanisms also lead to varying thermal agitation effects per lattice site, ultimately leading to differing net magnetizations [21].

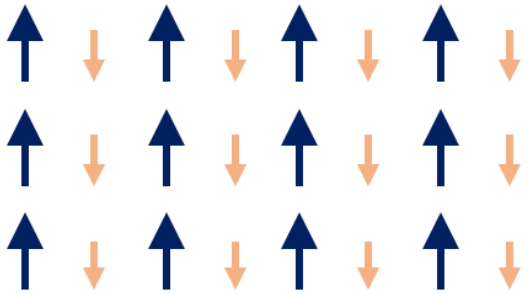

Figure 2.8: Ferrimagnetic ordering

There are many different groups of ferrimagnetic materials. One group has the general formula $MO{\cdot}Fe_2O_3$, where *M* is a transition metal such as manganese, nickel, cobalt, zinc or magnesium. Another group is made up of the hexagonal ferrites such as barium ferrite and strontium ferrite. A third group are the garnets which have the chemical formula $5Fe_2O_3{\cdot}3R_2O_3$, where *R* is a rare earth ion [22].

Although there are many different types of ferrimagnetic materials, those mentioned are commonly found in practical applications. The particular materials used in this work are bismuth-substituted terbium iron garnets (Bi:TIG) [23] and bismuth substituted yttrium iron garnets (Bi:YIG) [24]. These garnets are specially designed ferrites to be used in optical systems operating at a wavelength of 1550 nm. When an external magnetic field is applied and 1550 nm light is passed through these materials, the light experiences the Faraday effect [25].

2.3.2 The Magneto-Optic Faraday Effect

The Faraday effect is a phenomenon discovered by Michael Faraday in which the plane of polarization of an electromagnetic (EM) wave is rotated as it passes through an activated medium (Figure 2.9). The mode of activation can be due either to an electric field or magnetic field, depending on the material. If an EM wave is operating at optical frequencies and the mode of activation is due to an electric field, the phenomenon is called an electro-optic effect. If the mode is due to a magnetic field,

the phenomenon is called a magneto-optic effect. In both cases the material used is known as a Faraday rotator.

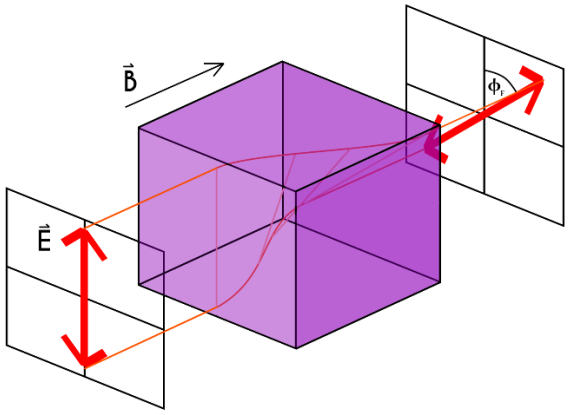

Figure 2.9: Faraday Rotation [26]

In the case of ferrimagnetic materials which exhibit the magneto-optic Faraday effect, these materials are called magneto-optic Faraday rotators (MOFRs). The angle of rotation the MOFR is capable of (φ_F) is a function of the magnetic field strength applied to the material (H), the propagation length in the material (L), and the Verdet constant (V)

$$\varphi_F = VHL \qquad (2.1)$$

Here, the Verdet constant is an optical constant describing the strength of the Faraday effect for the material used [27]. Given a particular dimension for the Faraday rotator, materials can have different Verdet constants and consequently will require different field strengths to achieve rotation.

Discovering and introducing new materials that exhibit higher specific Faraday rotation with less magnetic materials is an effort of great interest to engineers and scientists designing nonreciprocal optical and microwave devices. This engagement requires the fundamental understanding of how the Faraday effect is manifested at the atomic level.

2.3.3 The Origin of Magneto-Optic Faraday Rotation

This section closely follows the phenomenological model presented in [28]. Due to the unique chemistry that ferrites are composed, nonreciprocal electromagnetic properties are observed that allow strong interactions between the magnetic dipole moments of electrons and an optical wave. These interactions affect important parameters including the transmission coefficient, permeability, phase constant, and phase velocity.

Consider a ferrite composed of magnetic moments in a fixed position. Applying an external magnetic field allows the moments to align with the applied field, as long as they all align together. Under this applied field the dipoles precess about the dipole's center, whose torque can be calculated given the gyromagnetic ratio γ and angular momentum $\boldsymbol{P}$ (Figure 2.10). The frequency at which this precession occurs is known as the Larmor precession frequency (ω_0). When many magnetic moments are subjected to DC, RF, or optical fields, magnetic resonance is introduced. This magnetic resonance is a fundamental phenomenon that is of great interest to the optical and RF device research community.

Assume that a static field $\boldsymbol{B_0}$ is applied to the ferrite and a small AC field $\boldsymbol{B_1}$ is superimposed onto the static field. The AC field creates a forced precession on the dipole which changes its angular momentum. Considering a circularly-polarized clockwise (CW) and counter-clockwise (CCW) applied AC field, the effects of the forced precession can be seen (Figure 2.11). The resultant field $\boldsymbol{B_t}$ has different angles with respect to the z-axis depending on the polarization of the AC field. For *N*-dipoles, it can be observed at a macroscopic scale that differently polarized fields have different interactions with the ferrite material. In other words, since ferrites have permeability tensors that are not isotropic, the differently polarized waves that traverse the material will experience different rotations. For example, a linearly polarized wave is composed of equal but oppositely rotating circular polarizations (CW and CCW). Thus, a linearly

polarized wave will experience a rotation in its state of polarization as it travels through a ferrite since its CW and CCW components experience different permeability.

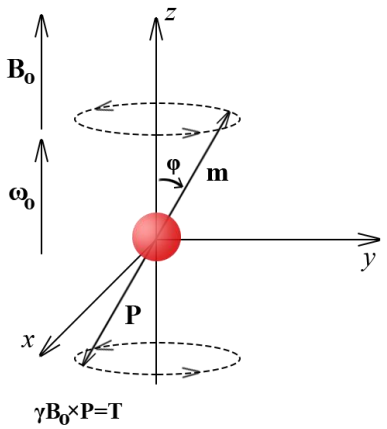

Figure 2.10: Precession of a magnetic dipole in a ferrite [28]

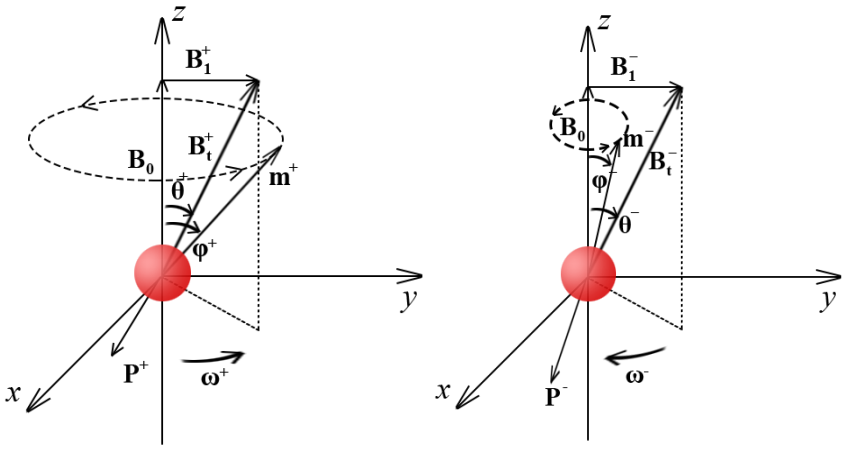

Figure 2.11: Forced precessions due to AC fields of CW (left) and CCW (right) polarizations [28]

The interaction between light and the MO materials described is one of the fundamental phenomena that enable MO all-optical switches. The physical interactions at the atomic scale lead to macroscopic effects that can be described mathematically using a rotation matrix. This matrix can then be used along with Jones calculus to solve the input and output characteristics of the Mach-Zehnder, Sagnac, Resonator, and other interferometer configurations.

2.4 Interferometer Configurations

The interferometers used throughout this study are the Mach-Zehnder, Sagnac, and Resonator. All three configurations have been widely used in research venues, but the Sagnac and Resonator have been more recently implemented as fiber-based all-optical switches [9]. Each analytical solution for the interferometers is presented using Jones calculus [29] [30].

2.4.1 Mach-Zehnder Interferometer

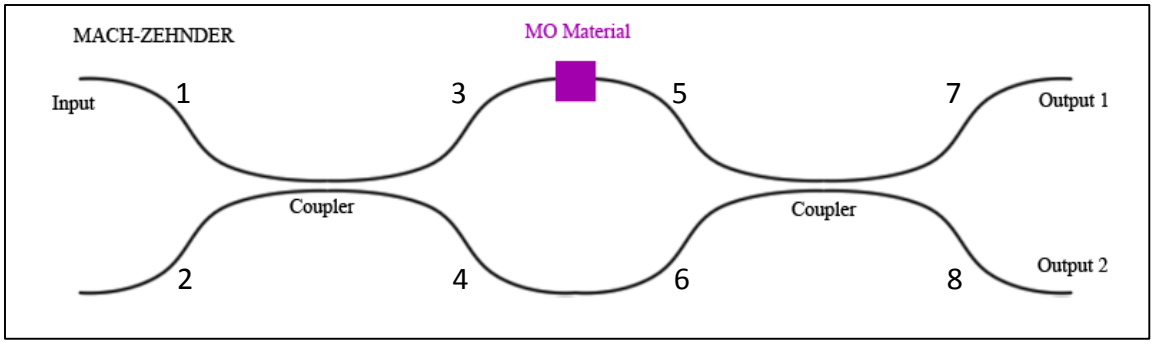

Figure 2.12: Mach-Zehnder Interferometer

The Mach-Zehnder interferometer is an all-optical router that uses two couplers in which the center arms are phase shifters. It is common to use the arms as delay lines to shift phase, but Faraday rotators can also be used to rotate the state of polarization (SoP) of incoming light and result in constructive or destructive interference at the output. Sufficiently changing the phase of the incident wave on one of the arms can cause enough interference to result in the optical signal switching output ports. In this section, Jones calculus analysis is used to determine the output of a Mach-Zehnder interferometer with an MO Faraday rotator placed in one of the arms. Outputs as a result of 0°, 90°, and 180° Faraday rotations are solved. The electric field entering ports 1 and 2 of the coupler are denoted E_{1i} and E_{2i}, respectively. That exiting port 1 and 2 are denoted E_{1o} and E_{2o}, respectively. Similar notations are used for ports 3 – 8 and are denoted accordingly.

Each coupler is designed to split signals by 3dB (half power). The output of the first coupler can be solved for using the Jones coupler matrix, assuming $E_{2i} = 0$:

$$\begin{bmatrix} \vec{E}_{3o} \\ \vec{E}_{4o} \end{bmatrix} = \frac{1}{\sqrt{2}} \begin{bmatrix} 1 & j \\ j & 1 \end{bmatrix} \begin{bmatrix} \vec{E}_{1i} \\ 0 \end{bmatrix} = \frac{1}{\sqrt{2}} \begin{bmatrix} \vec{E}_{1i} \\ j\vec{E}_{1i} \end{bmatrix} \quad (2.2)$$

Note the output signals are half power (which corresponds to a field strength reduction of $\frac{1}{\sqrt{2}}$) and the coupled signal has a 90° phase shift associated with it ($j\vec{E}_{1i}$). The signal traversing through the MO material can then be solved for, representing the MO material as a Jones rotational matrix:

$$\begin{bmatrix} E_{3o,xMO} \\ E_{3o,yMO} \end{bmatrix} = \begin{bmatrix} \cos\theta_F & -\sin\theta_F \\ \sin\theta_F & \cos\theta_F \end{bmatrix} \begin{bmatrix} E_{3o,x} \\ E_{3o,y} \end{bmatrix} = \frac{1}{\sqrt{2}} \begin{bmatrix} E_{1i,x}\cos\theta_F - E_{1i,y}\sin\theta_F \\ E_{1i,x}\sin\theta_F + E_{1i,y}\cos\theta_F \end{bmatrix} \quad (2.3)$$

The lumped transmission and phase components due to travelling the length of the arm is not considered until a later step. From above, the wave exiting the MO material can be rewritten, for convenience:

$$\vec{E}_{3o,MO} = \frac{1}{\sqrt{2}} \left[\left(E_{1i,x}\cos\theta_F - E_{1i,y}\sin\theta_F \right)\hat{x} + \left(E_{1i,x}\sin\theta_F + E_{1i,y}\cos\theta_F \right)\hat{y} \right] \quad (2.4)$$

This wave traverses the rest of the arm and arrives at the input to port 5. It is then found that the input to port 5 is:

$$\vec{E}_{5i} = T_1 e^{j\Phi_1} \vec{E}_{3o,MO}$$
$$= \frac{T_1 e^{j\Phi_1}}{\sqrt{2}} \left[\left(E_{1i,x}\cos\theta_F - E_{1i,y}\sin\theta_F \right)\hat{x} + \left(E_{1i,x}\sin\theta_F + E_{1i,y}\cos\theta_F \right)\hat{y} \right] \quad (2.5)$$

The wave exiting port 4 also traverses the rest of the other Mach-Zehnder arm to enter port 6:

$$\vec{E}_{6i} = T_2 e^{j\Phi_2} \vec{E}_{4o} = j\frac{T_2 e^{j\Phi_2}}{\sqrt{2}} \vec{E}_{1i} \quad (2.6)$$

Notice that the transmission and phase components have now been included to E_{5i} and $\vec{E}_{6i}$. Assuming equivalent transmission coefficients and phase terms ($T_1 = T_2 = T$ and $\Phi_1 = \Phi_2 = \Phi$), the final form of the solution to the Mach-Zehnder interferometer can be determined:

$$\begin{bmatrix}\vec{E}_{7o}\\ \vec{E}_{8o}\end{bmatrix}=\frac{1}{\sqrt{2}}\begin{bmatrix}1 & j\\ j & 1\end{bmatrix}\begin{bmatrix}\vec{E}_{5i}\\ \vec{E}_{6i}\end{bmatrix}=\frac{1}{\sqrt{2}}\begin{bmatrix}\vec{E}_{5i}+j\vec{E}_{6i}\\ j\vec{E}_{5i}+\vec{E}_{6i}\end{bmatrix}=$$

$$\boxed{\frac{Te^{j\Phi}}{2}\begin{bmatrix}\left(E_{1i,x}\cos\theta_F-E_{1i,y}\sin\theta_F\right)\hat{x}+\left(E_{1i,x}\sin\theta_F+E_{1i,y}\cos\theta_F\right)\hat{y}-\vec{E}_{1i}\\ j\left(E_{1i,x}\cos\theta_F-E_{1i,y}\sin\theta_F\right)\hat{x}+j\left(E_{1i,x}\sin\theta_F+E_{1i,y}\cos\theta_F\right)\hat{y}+j\vec{E}_{1i}\end{bmatrix}} \quad (2.7)$$

Assuming $T=1$ and $\Phi=0$ for simplicity, the output for a Faraday rotation of $\theta_F=0°$, $90°$, and $180°$ can be solved (Table 1).

Table 1: Mach-Zehnder Output

$\boldsymbol{\theta_F}$	$\boldsymbol{E_{7o}}$	$\boldsymbol{E_{8o}}$
$0°$	0	jE_{1i}
$90°$	$E_{1i,y}$	$jE_{1i,x}$
$180°$	$-E_{1i}$	0

This table shows that given an input at port 1, no input at port 2, and without magnetizing the MO material, maximum output results at port 8 with a 90° phase shift relative to the input ($j=e^{j\frac{\pi}{2}}$). Given the same input but magnetizing the MO material to rotate the SoP of E_{3o} by 90°, the outputs at port 7 and 8 are equivalent in magnitude, however port 8 has a phase shift of 90°. Finally, by rotating the SoP even further to 180°, maximum output results at port 7 with a 180° phase shift ($-1=e^{j\pi}$).

2.4.2 Sagnac Interferometer

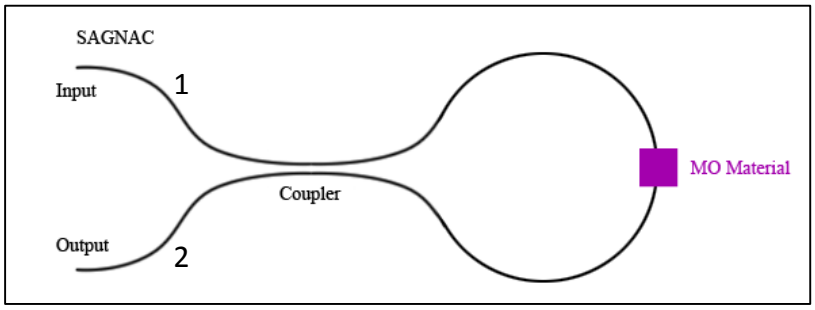

Figure 2.13: Sagnac Interferometer

The Sagnac is an all-optical router that uses one coupler which splits an incoming signal, each split signal's SoP is then specially rotated due to the MO material, and the signals re-enter the same coupler and interfere at the output. The Sagnac configuration is unique because the two split signals travel the exact same path length prior to re-entering the coupler. If any environmental factors (which are usually reciprocal phenomena) have an effect on part of the loop, both of the split signals experience the same effect and no relative phase difference between the signals is created resulting in a very stable output.

Assuming only input at port 1 ($\vec{E}_{2i} = 0$), the electric field vectors exiting ports 3 and 4 can be represented by the following, which is similar to that found in the first step of solving the Mach-Zehnder in Section 2.4.1:

$$\begin{bmatrix} \vec{E}_{3o} \\ \vec{E}_{4o} \end{bmatrix} = \frac{1}{\sqrt{2}} \begin{bmatrix} 1 & j \\ j & 1 \end{bmatrix} \begin{bmatrix} \vec{E}_{1i} \\ 0 \end{bmatrix} = \frac{1}{\sqrt{2}} \begin{bmatrix} \vec{E}_{1i} \\ j\vec{E}_{1i} \end{bmatrix} \quad (2.8)$$

The waves are then guided around the loop through the MO material, experiencing a rotation of their SoP. The material can be represented as a rotational matrix, similarly as in Section 2.4.1. The wave exiting port 3 and travelling through the MO material can then be written in terms of its x- and y-components:

$$\begin{bmatrix} E_{3o,xMO} \\ E_{3o,yMO} \end{bmatrix} = \begin{bmatrix} \cos\theta_F & -\sin\theta_F \\ \sin\theta_F & \cos\theta_F \end{bmatrix} \begin{bmatrix} E_{3o,x} \\ E_{3o,y} \end{bmatrix} = \begin{bmatrix} \left(E_{3o,x}\cos\theta_F - E_{3o,y}\sin\theta_F\right) \\ \left(E_{3o,x}\sin\theta_F + E_{3o,y}\cos\theta_F\right) \end{bmatrix} \quad (2.9)$$

Combining the x- and y-components and noting that $E_{3o} = \frac{E_{1i}}{\sqrt{2}}$, the wave at the input of port 4 results in the following:

$$\vec{E}_{4i} = \frac{T_1 e^{j\Phi_1}}{\sqrt{2}}\left[\left(E_{1i,x}\cos\theta_F - E_{1i,y}\sin\theta_F\right)\hat{x} + \left(E_{1i,x}\sin\theta_F + E_{1i,y}\cos\theta_F\right)\hat{y}\right] \quad (2.10)$$

Here, T_1 and Φ_1 are the transmission coefficient and phase change due to traversing the Sagnac loop through the fiber and the MO material. The wave exiting port 4 and

traversing through the MO material also experiences a Faraday rotation that rotates the SoP in the same direction relative to an outside observer:

$$\begin{bmatrix} E_{4o,xMO} \\ E_{4o,yMO} \end{bmatrix} = \begin{bmatrix} \cos\theta_F & \sin\theta_F \\ -\sin\theta_F & \cos\theta_F \end{bmatrix} \begin{bmatrix} E_{4o,x} \\ E_{4o,y} \end{bmatrix} \quad (2.11)$$

Similarly, the wave at the input of port 3 is found to be the following (note $E_{2i} = 0$):

$$\vec{E}_{3i} = \frac{T_2 e^{j\Phi_2}}{\sqrt{2}} \left[j\left(E_{1i,x}\cos\theta_F + E_{1i,y}\sin\theta_F\right)\hat{x} + j\left(E_{1i,y}\cos\theta_F - E_{1i,x}\sin\theta_F\right)\hat{y} \right] \quad (2.12)$$

T_2 and Φ_2 in this case are due to traversing the Sagnac loop in the opposite direction. Lastly, the electric field vectors pass through the coupler again, and resulting Sagnac interferometer equation can be determined:

$$\begin{bmatrix} \vec{E}_{1o} \\ \vec{E}_{2o} \end{bmatrix} = \frac{1}{\sqrt{2}} \begin{bmatrix} 1 & j \\ j & 1 \end{bmatrix} \begin{bmatrix} \vec{E}_{3i} \\ \vec{E}_{4i} \end{bmatrix} = \frac{T_1 T_2 e^{j(\Phi_1+\Phi_2)}}{2} \begin{bmatrix} \vec{E}_{3i} + j\vec{E}_{4i} \\ j\vec{E}_{3i} + \vec{E}_{4i} \end{bmatrix} =$$

$$\boxed{Te^{j\Phi} \begin{bmatrix} \left(j\,E_{1i,x}\cos\theta_F\right)\hat{x} + \left(jE_{1i,y}\cos\theta_F\right)\hat{y} \\ -\left(E_{1i,y}\sin\theta_F\right)\hat{x} + \left(E_{1i,x}\sin\theta_F\right)\hat{y} \end{bmatrix}} \quad (2.13)$$

Here, $T = T_1 T_2$ and $\Phi = \Phi_1 + \Phi_2$. Assuming $T = 1$ and $\Phi = 0$ for simplicity, we can solve for the output at ports 1 and 2 (Table 2).

Table 2: Sagnac Output

$\boldsymbol{\theta_F}$	$\vec{\boldsymbol{E}}_{\boldsymbol{1o}}$	$\vec{\boldsymbol{E}}_{\boldsymbol{2o}}$
0°	$jE_{1i,x}$	0
90°	0	$-E_{1i,y}\hat{x} + E_{1i,x}\hat{y}$

2.4.3 Resonator Interferometer

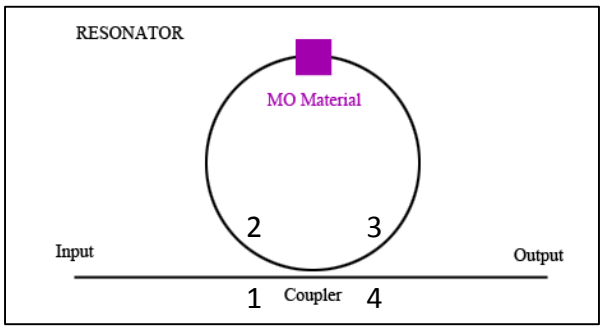

Figure 2.14: Resonator Interferometer

The resonator can be used as an all-optical switch that requires a coupler to couple light onto a ring-resonating path that builds in amplitude, is delayed with respect to the incoming signal due to the loop path travelled, and thus creates interference at the output. Placing an MO material at the center of the loop changes the SoP of the resonating signal, changing the interference pattern at the output. The resonator configuration is special since the resonant signal traverses the loop many times, and thus experiences many changes in its SoP.

In solving for the resonator with MO material, the resonator without MO material must be first solved to show the general approach. Solutions are determined using the Jones calculus technique [29].

2.4.3.1 Solution without MO Material

Solving for the coupler output ports (3 and 4) without MO material present gives a similar result to that seen in subsections 2.4.1 and 2.4.2.

$$\begin{bmatrix}\vec{E}_{3o}\\ \vec{E}_{4o}\end{bmatrix} = \frac{1}{\sqrt{2}}\begin{bmatrix}1 & j\\ j & 1\end{bmatrix}\begin{bmatrix}\vec{E}_{1i}\\ \vec{E}_{2i}\end{bmatrix} = \frac{1}{\sqrt{2}}\begin{bmatrix}\vec{E}_{1i} + j\vec{E}_{2i}\\ j\vec{E}_{1i} + \vec{E}_{2i}\end{bmatrix} \quad (2.14)$$

Due to the direct connection of port 4 to port 2, the input to port 2 becomes nonzero after a very short time:

$$\vec{E}_{2i} = T_1\vec{E}_{4o}e^{j\Phi} = \frac{T_1}{\sqrt{2}}\left(j\vec{E}_{1i} + \vec{E}_{2i}\right)e^{j\Phi} = \frac{jT_1}{\sqrt{2}}\vec{E}_{1i}e^{j\Phi} + \frac{T_1}{\sqrt{2}}\vec{E}_{2i}e^{j\Phi} \quad (2.15)$$

$$\rightarrow \vec{E}_{2i} = \frac{\frac{jT_1e^{j\Phi}}{\sqrt{2}}}{1-\frac{T_1}{\sqrt{2}}e^{j\Phi}}\vec{E}_{1i} \quad (2.16)$$

The output at port 3 can then be solved since the input at port 2 is now defined:

$$\vec{E}_{3o} = \frac{1}{\sqrt{2}}\left(\vec{E}_{1i} + j\vec{E}_{2i}\right) = \frac{1}{\sqrt{2}}\left[\vec{E}_{1i} - \frac{\frac{T_1e^{j\Phi}}{\sqrt{2}}}{1-\frac{T_1}{\sqrt{2}}e^{j\Phi}}\vec{E}_{1i}\right] = \boxed{\frac{\vec{E}_{1i}}{\sqrt{2}}\left(1 - \frac{\frac{T_1e^{j\Phi}}{\sqrt{2}}}{1-\frac{T_1}{\sqrt{2}}e^{j\Phi}}\right)} \quad (2.17)$$

2.4.3.2 Solution with MO Material

Now, by placing the material at the center of the resonator loop the formulation becomes more complicated, but a similar approach can be used. The output at ports 3 and 4 can be represented by:

$$\begin{bmatrix}\vec{E}_{3o}\\ \vec{E}_{4o}\end{bmatrix} = \frac{1}{\sqrt{2}}\begin{bmatrix}1 & j\\ j & 1\end{bmatrix}\begin{bmatrix}\vec{E}_{1i}\\ \vec{E}_{2i}\end{bmatrix} \quad (2.18)$$

Also, the wave entering port 2 can be determined using the rotational Jones matrix similar to Sections 2.4.1 and 2.4.2:

$$\begin{bmatrix}\boldsymbol{E_{2i,x}}\\ \boldsymbol{E_{2i,y}}\end{bmatrix} = \boldsymbol{T_2e^{j\Phi_2}}\begin{bmatrix}\boldsymbol{E_{4o,xMO}}\\ \boldsymbol{E_{4o,yMO}}\end{bmatrix} = \boldsymbol{T_1T_2e^{j\Phi_1}e^{j\Phi_2}}\begin{bmatrix}\boldsymbol{\cos\theta_F} & \boldsymbol{-\sin\theta_F}\\ \boldsymbol{\sin\theta_F} & \boldsymbol{\cos\theta_F}\end{bmatrix}\begin{bmatrix}\boldsymbol{E_{4o,x}}\\ \boldsymbol{E_{4o,y}}\end{bmatrix}$$

$$= Te^{j\Phi}\begin{bmatrix}\cos\theta_F & -\sin\theta_F\\ \sin\theta_F & \cos\theta_F\end{bmatrix}\begin{bmatrix}E_{4o,x}\\ E_{4o,y}\end{bmatrix} \quad (2.19)$$

Here, $T = T_1T_2$ describes the transmission coefficient between port 4 and the MO material and between the MO material and port 2. θ_F is the angle of rotation of the SoP. $\Phi = \Phi_1 + \Phi_2$ is the phase change between port 4 and the MO material and between the MO material and port 2.

Solving for $\vec{E}_{4o}$ in terms of $\vec{E}_{2i}$ gives,

$$\begin{bmatrix}E_{4o,x}\\ E_{4o,y}\end{bmatrix} = \frac{1}{Te^{j\Phi}}\begin{bmatrix}\cos\theta_F & \sin\theta_F\\ -\sin\theta_F & \cos\theta_F\end{bmatrix}\begin{bmatrix}E_{2i,x}\\ E_{2i,y}\end{bmatrix} \quad (2.20)$$

Considering each component separately, it is found that:

$$E_{4o,x} = \frac{1}{\sqrt{2}}\left(jE_{1i,x} + E_{2i,x}\right) = \frac{1}{Te^{j\Phi}}\left(E_{2i,x}\cos\theta_F + E_{2i,y}\sin\theta_F\right) \quad (2.21)$$

$$E_{4o,y} = \frac{1}{\sqrt{2}}\left(jE_{1i,y} + E_{2i,y}\right) = \frac{1}{Te^{j\Phi}}\left(-E_{2i,x}\sin\theta_F + E_{2i,y}\cos\theta_F\right) \quad (2.22)$$

Using these equations, $\vec{E}_1$ can be defined in terms of $\vec{E}_2$:

$$jTe^{j\Phi}E_{1i,x} = \sqrt{2}E_{2i,x}\cos\theta_F + \sqrt{2}E_{2i,y}\sin\theta_F - Te^{j\Phi}E_{2i,x} \quad (2.23)$$

$$jTe^{j\Phi}E_{1i,y} = -\sqrt{2}E_{2i,x}\sin\theta_F + \sqrt{2}E_{2i,y}\cos\theta_F - Te^{j\Phi}E_{2i,y} \quad (2.24)$$

This can be represented in Jones calculus form for convenience as:

$$jTe^{j\Phi}\begin{bmatrix}E_{1i,x}\\E_{1i,y}\end{bmatrix} = \begin{bmatrix}\sqrt{2}\cos\theta_F - Te^{j\Phi} & \sqrt{2}\sin\theta_F\\ -\sqrt{2}\sin\theta_F & \sqrt{2}\cos\theta_F - Te^{j\Phi}\end{bmatrix}\begin{bmatrix}E_{2i,x}\\E_{2i,y}\end{bmatrix} \quad (2.25)$$

Extracting $\sqrt{2}$ and solving for $\vec{E}_{2i}$ gives:

$$\begin{bmatrix}E_{2i,x}\\E_{2i,y}\end{bmatrix} = \frac{\frac{jTe^{j\Phi}}{\sqrt{2}}}{\left(\cos\theta_F - \frac{Te^{j\Phi}}{\sqrt{2}}\right)^2 + \sin^2\theta_F}\begin{bmatrix}\cos\theta_F - \frac{Te^{j\Phi}}{\sqrt{2}} & -\sin\theta_F\\ \sin\theta_F & \cos\theta_F - \frac{Te^{j\Phi}}{\sqrt{2}}\end{bmatrix}\begin{bmatrix}E_{1i,x}\\E_{1i,y}\end{bmatrix} \quad (2.26)$$

$\vec{E}_{3o}$ can also be represented in terms of its x- and y-components:

$$\vec{E}_{3o} = \frac{1}{\sqrt{2}}\left(\vec{E}_{1i} + j\vec{E}_{2i}\right) \rightarrow \begin{bmatrix}E_{3o,x}\\E_{3o,y}\end{bmatrix} = \frac{1}{\sqrt{2}}\begin{bmatrix}E_{1i,x}\\E_{1i,y}\end{bmatrix} + \frac{j}{\sqrt{2}}\begin{bmatrix}E_{2i,x}\\E_{2i,y}\end{bmatrix} \quad (2.27)$$

Using Equation 2.26 with Equation 2.27, the output at port 3 can be determined:

$$\boxed{\begin{bmatrix}E_{3o,x}\\E_{3o,y}\end{bmatrix} = \frac{1}{\sqrt{2}}\begin{bmatrix}E_{1i,x}\\E_{1i,y}\end{bmatrix} - \frac{1}{\sqrt{2}}\frac{\frac{Te^{j\Phi}}{\sqrt{2}}}{\left(\cos\theta_F - \frac{Te^{j\Phi}}{\sqrt{2}}\right)^2 + \sin^2\theta_F}\begin{bmatrix}\cos\theta_F - \frac{Te^{j\Phi}}{\sqrt{2}} & -\sin\theta_F\\ \sin\theta_F & \cos\theta_F - \frac{Te^{j\Phi}}{\sqrt{2}}\end{bmatrix}\begin{bmatrix}E_{1i,x}\\E_{1i,y}\end{bmatrix}} \quad (2.28)$$

2.4.3.3 Summary of Output

One method to verify that Equation 2.29 is sufficient would be to set $\theta_F = 0^0$ and compare the result to Equation 2.18. The results should be equivalent. Setting $\theta_F = 0^0$ gives:

$$\begin{bmatrix} E_{3o,x} \\ E_{3o,y} \end{bmatrix} = \frac{1}{\sqrt{2}} \begin{bmatrix} E_{1i,x} \\ E_{1i,y} \end{bmatrix} - \frac{\frac{Te^{j\Phi}}{\sqrt{2}}}{\left(1-\frac{Te^{j\Phi}}{\sqrt{2}}\right)^2} \begin{bmatrix} 1-\frac{Te^{j\Phi}}{\sqrt{2}} & 0 \\ 0 & 1-\frac{Te^{j\Phi}}{\sqrt{2}} \end{bmatrix} \begin{bmatrix} E_{1i,x} \\ E_{1i,y} \end{bmatrix} \quad (2.29)$$

Simplifying this result gives:

$$\begin{bmatrix} E_{3o,x} \\ E_{3o,y} \end{bmatrix} = \frac{1}{\sqrt{2}} \begin{bmatrix} E_{1i,x} \\ E_{1i,y} \end{bmatrix} - \frac{1}{\sqrt{2}} \frac{\frac{Te^{j\Phi}}{\sqrt{2}}}{1-\frac{Te^{j\Phi}}{\sqrt{2}}} \begin{bmatrix} 1 & 0 \\ 0 & 1 \end{bmatrix} \begin{bmatrix} E_{1i,x} \\ E_{1i,y} \end{bmatrix} \quad (2.30)$$

Combining the x- and y-components, the result becomes that described in Section 2.4.3.1, as expected:

$$\boxed{\vec{E}_{3o} = \frac{\vec{E}_{1i}}{\sqrt{2}} \left(1 - \frac{\frac{Te^{j\Phi}}{\sqrt{2}}}{1-\frac{Te^{j\Phi}}{\sqrt{2}}}\right)} \quad (2.31)$$

2.5 Conclusion

In the solutions for the Mach-Zehnder, Sagnac, and Resonator interferometer configurations, the MO material is the cause of the Faraday rotation, and thus the differing outputs. In the case of the fiber-based configurations that will be presented in Chapter 3 – Chapter 7, the material is activated by applying an external magnetic field in the direction of propagation of light. The manner in which this field is generated is tailored to the MO material used, since different materials have different activation requirements. Therefore, it is of special interest to know the challenges of generating a magnetic field and how to do so with low power, high speed, and maintain a compact size.

CHAPTER 3

MAGNETIC FIELD GENERATOR DESIGN

Modified from the paper published in the *IEEE Transactions on Magnetics*

John W. Pritchard, Mani Mina, and Robert J. Weber

It has been a challenge to design magnetic field generation devices for small-scale, low-power, and deployable solutions in MO systems [31] [32]. Much effort has been put into the design of the MO material and how to implement it in optical systems [23] [14] [33] [34] [35], but it is equally important to design the proper field generator for component magnetization. For dynamic field generators used for modulation, this is usually done with a coil and a current driver, such that a sufficient current can create a magnetic field that is suitable for Faraday rotation in the optical circuit. Similar devices exist and are commercially available for fiber-based systems. However, these devices currently have response times on the order of 10 µs. As the technology continues to grow and advance, faster and more compact MO switches will be desired. This translates to the need for enhanced magnetic field generators and more responsive MO materials. Currently, the MO materials are very responsive [36], but the small-scale magnetic field generators are not able to match the MO material's potential. Thus, it is of great interest to pursue and report design methods and procedures that result in such well-designed field generators.

3.1 MFG Design for Magneto-Optic Interferometers

To design a suitable MFG, several different factors must be considered. The overall goal is to obtain great optical response due to the application of magnetic fields, but accurate modeling is not necessarily straight forward. However, in understanding how the field interacts with the MO material, parameters can be optimized to achieve

fast and stable optical switching. The following sections describe an MFG design process that leads to specific design decisions for magneto-optic interferometric switching (Figure 3.1).

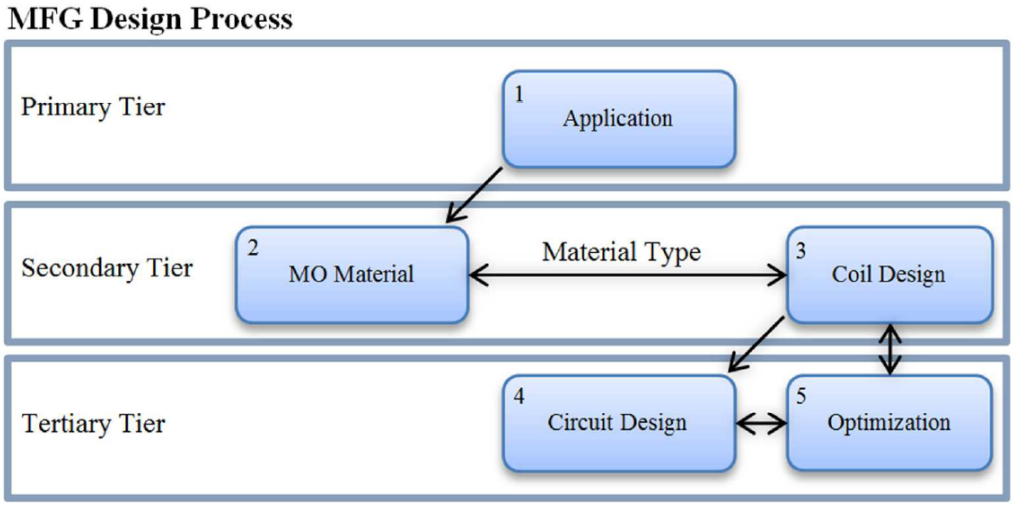

Figure 3.1: MFG design process

3.1.1 Application

Primary MFG parameters of interest include coil inductance and current requirement. Constraints that affect these parameters include, but are not limited to, required field strength, electronic rise time, and electronic fall time. All optimizations will depend on the coil geometry and configuration, which further depend on the application.

Two specific applications include a high speed MO switch and a low power switch. For a high speed switch, it is advantageous to have fast control of the magnetization of the MO material. Thus, it may be best to choose a single-coil configuration with a low number of turns to minimize inductance and optimize rise or fall time. For a low power switch where such high speeds are not needed, it may be advantageous to choose a dual coil configuration. These are discussed in more detail in Section 3.1.3).

3.1.2 MO Material

For optical modulation applications, a soft MO material (meaning, one with low coercivity) may be best suited for use as the modulation element. It is often desired to utilize materials with low loss, low temperature dependence, and low saturation field which well-designed soft MO materials provide. Alternatively, hard MO materials whose domains latch to a direction of magnetization could be chosen for low power signal routing applications. This is advantageous as it eliminates the need for a prolonged external field to maintain a certain magnetized state. However, these materials often have higher temperature coefficients, worsened wavelength dispersion, and require greater field strength for sufficient rotation compared to soft MO materials.

Once the application and MO material have been chosen, the coil configuration can be considered and circuit optimization techniques can be employed to achieve fine electronic response, which, in effect, leads to desirable optical output.

3.1.3 Coil Design

Many coil configurations can be used, however two categories can be defined as the most basic types: single-coil and multi-coil configurations (Figure 3.2). In this study, two-coil systems will be the focus of the multi-coil configurations.

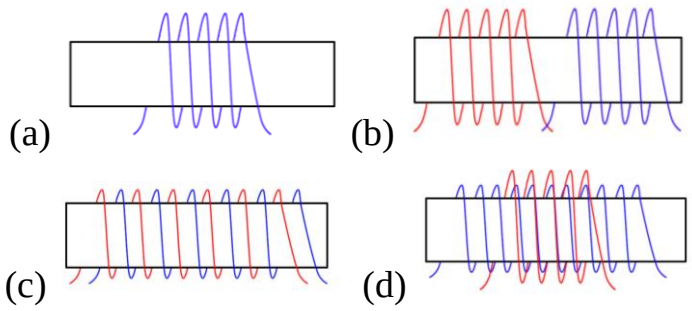

Figure 3.2: Illustration of different coil configurations

Single-coil configurations utilize an N-turn coil to control the magnetization of the MO material. This is traditionally the configuration that is used, as it is effective for most applications. Multi-coil configurations utilize independently controlled coils each with N_1, N_2, …, N_n turns. This type of field generator can be used where low power operation of optical pulses with long periods may be required. Recent works have shown that the use of one coil of low number of turns can be used to quickly magnetize the material while a second coil of much higher number of turns can be used to sustain the magnetization dissipating much less power (Figure 3.2(d), see also Chapter 4) [37]. In addition, research has shown that dual coil configurations can also be used where a fast, single-shot optical pulse is desired. In this case, the second coil can be used to neutralize any residual energy in the first coil (Figure 3.2(c), see also Chapter 5), reducing sluggish fall time [15]. Other dual coil configurations that are not independently controlled, such as the well-known Helmholtz coil, can be used for creating uniform fields where space constraints is not an issue.

In designing the proper coil, parameters of interest include the inductance, radius, number of turns, and length. Assuming a tightly wound coil with no spacing between turns, the length of the coil is determined by the wire diameter and number of turns.

For a single coil, it is found that B can be approximated by the following, leading to the inductance, $\boldsymbol{L}$ [13]:

$$B = \frac{\mu NI}{\sqrt{l^2+4R^2}} \rightarrow L = \frac{\mu N^2 \pi R^2}{\sqrt{l^2+4R^2}} \qquad (3.1)$$

since $A = \pi R^2$, where R is the radius of the coil, I is the current, and l is the length of the coil. This equation can be used for multi-coil configurations as well, since each coil is independently controlled. However, mutual inductance will then need to be considered for analysis and optimization.

For the Helmholtz coil configuration (Figure 3.4), the magnetic flux at the on-axis midpoint between the two coils can be approximated using Equation 3.2 [22]. Inductance

can then be found similarly as in Equation 3.1, but must be doubled since two coils are present in the circuit:

$$B = \frac{\mu(0.7155)NI}{R} \rightarrow L_{total} = 2\mu(0.7155)N^2\pi R \qquad (3.2)$$

Additionally, it would be advantageous to have a figure of merit in the design of the coil, and it is proposed that this figure be L/B. Having such a geometry dependent metric will more clearly present the link between L and B for the designer. These calculations, which include the field generated and coil inductance, length, and radius, can be used optimize the MFG electronic circuitry.

3.1.4 Circuit Design and Optimization

The driver circuit will depend on the field generator choice, particularly if single- or multi-coil configurations are used. Once a switching architecture has been decided upon, the parameters from the field generator design as well as the application specifications are inputted into simulation software. The designer then sets optimization conditions and fine-tunes the driver circuit.

3.2 Resonator Interferometer with Helmholtz Field Generator

As an example of this design process, a magneto-optic switch of resonator configuration was implemented with a bismuth substituted iron garnet (BIG) as the MO material. A Helmholtz coil was designed for the field generator and its driver circuitry was optimized.

The optical switch in which this MFG was implemented is of ring resonator configuration. Optical resonator configurations have shown promise in serving as fast optical switches (see Chapter 6). The device consists of an optical waveguide that couples to a second waveguide in the shape of a ring. The coupled light begins to resonate and build in amplitude in the ring, interfering with the input wave at the coupled region. This configuration has become especially popular due to its simplicity

and potential for monolithic integration. Recent works have fabricated such a device for use in EO switches [38]. It is only natural that an MO switch of similar design be implemented in the future, due to its ability to serve as a low power alternative. The optical switch used here consists of a 1550nm laser, isolator, 3dB coupler, two linear polarizers, MO material (BIG), MFG, and detector circuitry (Figure 3.3). An oscilloscope was used to observe the optical output.

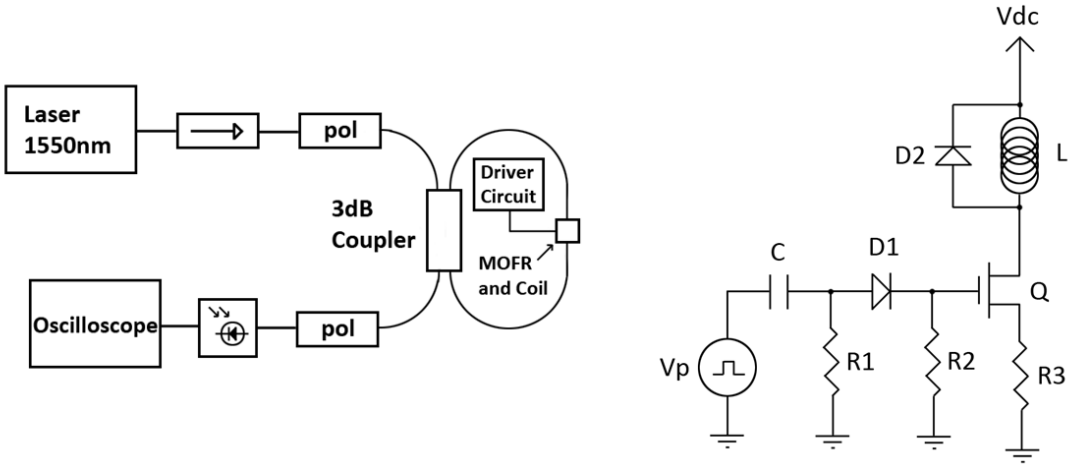

Figure 3.3: Optical experiment setup and electronic driver circuit

The chemical composition of the specific BIG used is $(Bi_{1.1}Tb_{1.9})(Fe_{4.25}Ga_{0.75})O_{12}$ [23] [34] [35]. This is a soft ferrimagnetic material to be used in the optical resonator as the modulating element. It was chosen for its low temperature coefficient, low saturation field requirement, and specific Faraday rotation. These parameters are -0.060 deg/˚C, less than 225 Oe, and -96 deg/mm, respectively. Two samples, each with a thickness of 470µm, were placed back-to-back in the optical circuit.

The Helmholtz coil (Figure 3.4) was designed based on the geometrical constraints of the optical connectors. The connectors used have a 3.2mm diameter protective structure, with a zirconia mating sleeve to easily align the fiber ends. The Helmholtz coil was then designed with each coil length being 1.6mm, each having 5 turns, with each radius near 1.6mm, and thus an inter-coil spacing of 1.6mm. Using the equations described, the coil has a theoretical inductance of approximately 127nH.

The MFG electronics design consists of a single-MOSFET switching circuit (Figure 3.3), which serves to drive current through the Helmholtz coil. This circuit includes a fast, low-power MOSFET switch (Fairchild FDC655BN), Helmholtz coil for field generation, and appropriate passive components for signal shaping and protection. Circuit optimization was performed using Cadence Circuit Design Suite (ver. 16.2), with goals that minimize rise and fall time constrained by coil currents (in order to reduce power).

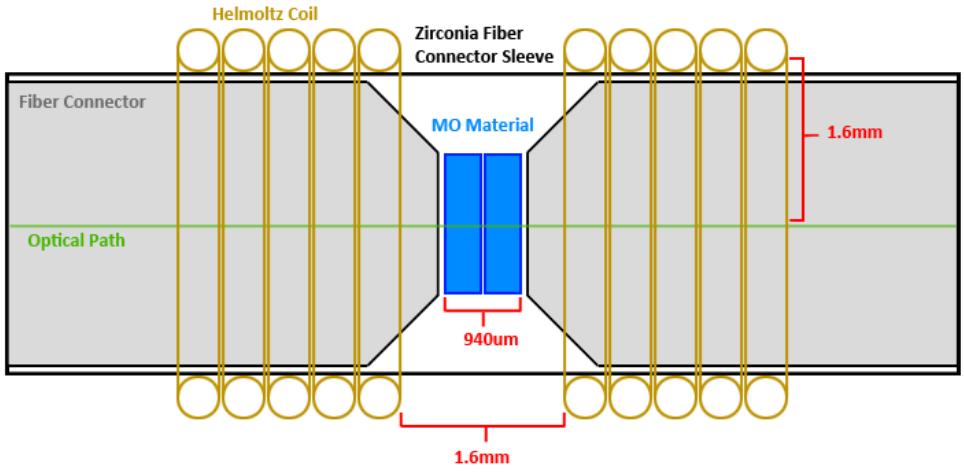

Figure 3.4: Helmholtz coil and interface of fiber connectors and MO material

Using the described electronic switching circuit architecture and optimizing using Cadence Design Suite, component values resulted in 65nF for C, 50Ω for R1, 100Ω for R2, and 1.1Ω for R3. The N-channel MOSFET has a typical rated rise and fall of 2ns. Additionally, the FET's typical input and output capacitances are 470pF and 100pF, respectively, with an on-resistance of 26mΩ.

Optical and electrical results are provided (Figure 3.5). The current through the current-sense resistor (R_3) shows a peak of 5A achieved with 184ns pulse width, resulting in a magnetic field strength of 166.7Oe in magnitude. The generated field led to an optical response (normalized) of approximately 150ns, where response is defined as the amount of time taken for the optical signal to rise from 10% to 90% of the

maximum amplitude of the optical signal. However, the optical fall time is lengthy due to effects from the material's hysteresis and the residual current circulating in the coil after the electronic switch has turned off, which continues to magnetize the MO material. This issue and suggested remedies are discussed in detail in Chapter 5 [15].

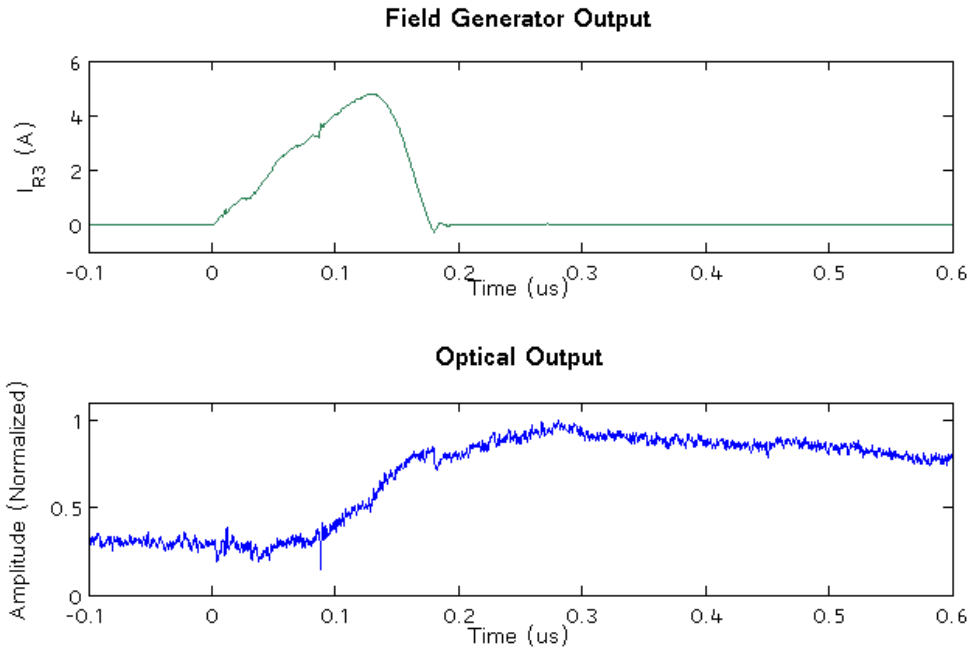

Figure 3.5: Measured electrical and optical outputs

3.3 Conclusion

In this chapter, a novel method for designing and optimizing magnetic field generators for magneto-optical systems is proposed. Optical and electrical experimental results using the described method are provided and discussed. The presented design methodologies expand the toolset for magneto-optic switch designers, and also provide a platform for enhancing the magnetic field generation for similar applications in the future.

This magnetic field generator design methodology serves as one of the key platforms upon which this research is based. In order to develop novel MO switches

and routers, having suitable field generators is a bare minimum. Solidifying this design methodology will allow for a stronger foundation in MO interferometer research as a whole, especially when optimizing for high speed and low power operation.

CHAPTER 4

ENHANCEMENTS FOR LOW POWER OPERATION

Modified from the paper published in the *Journal of Applied Physics*

John W. Pritchard, Mani Mina, Robert J. Weber, and Sasha (Kemmet) Oster

In this chapter, novel approach for low power operation of a fiber-based, magneto-optic router is proposed. The router, with reasonable speed compared to competitive designs, operates at considerably reduced power levels which makes it a practical deployable solution. The optical setup consists of a Faraday rotator in a fiber-based Sagnac interferometer in which optical switching is controlled by an electronic driving circuit, similarly to that presented in Section 3.2. The electronic system generates a magnetic field through the Faraday rotator by driving current through a specially designed two-coil system. The new coil system allows for sufficient field generation at low quiescent power levels while maintaining very short optical rise and fall times. The electronic design considerations as well as the effect of mutual inductance between the two coils and its influence on switching times are investigated. The Faraday rotator is placed at the center of the loop in the Sagnac interferometer. Appropriate phase shift for interference is achieved by the proposed field generating system designed for the magneto-optical element. The theory of operation, design, experimental results, and optical and electronic setup are presented and analyzed in this chapter.

4.1 Experimental Setup

The experimental setup includes the optical system and the field generation system (Figure 4.1). The MO material used is a bismuth-doped iron garnet (BIG)

$[(Bi_{1.1}Tb_{1.9})(Fe_{4.25}Ga_{0.75})O_{12}]$ [23] and is placed in the Sagnac loop, ideally such that the optical paths on either side of the material are equidistant.

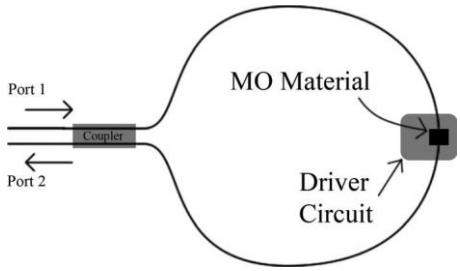

Figure 4.1: Fiber-based Sagnac interferometer

The high speed field generation system controls and enables the magnetized state of the MO material and is placed appropriately. This is the driving force that constitutes the switching capability of the system. The proposed circuit is composed of two separate circuits that drive current through $coil_1$ and $coil_2$ of the two-coil system (Figure 4.2). The circuit that drives the current through $coil_1$ provides a very rapid, high current pulse to quickly magnetize the MO material. The mutual inductance does not affect the total field in the MO material, but it does affect how the input signals are shaped to achieve the total field. For example, V_{p1} and V_{p2} have identical voltage profiles, but the voltage seen at the gate of MOSFET M_1 decreases rapidly as a result of the charging series capacitor. The purpose of this is to control the initial magnetization of the material while minimizing total current drawn. $Coil_1$ should energize for only a brief moment to quickly magnetize the MO material. The circuit driving the current through $coil_2$ provides a longer pulse of less amperage to sustain the material's magnetization. The distinction between both control circuits is advantageous because effects of mutual inductance can be compensated by adjusting the input voltage profiles. Bypass capacitors, current sense resistors, protection diodes, and other passives were placed appropriately.

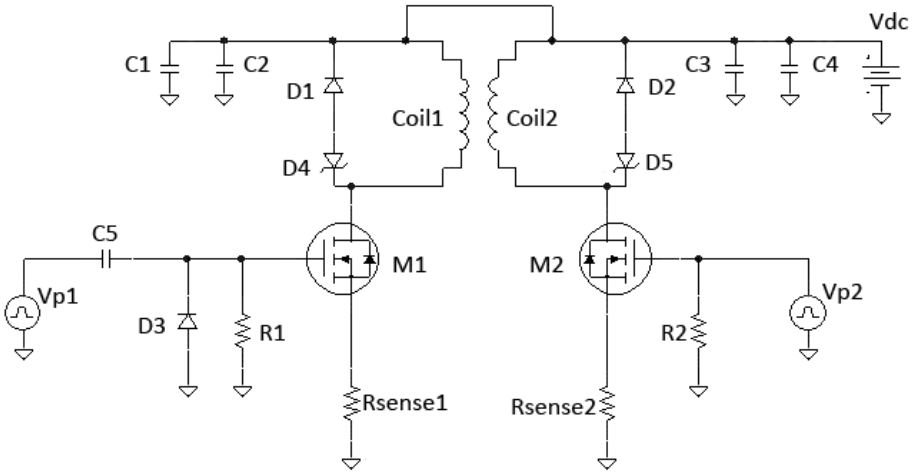

Figure 4.2: High speed field generation circuit

4.2 Proposed System

To achieve all-optical switching, fiber-based interferometers have been shown to be reasonable and practical solutions [39]. While different interferometer topologies could be used, the fiber-based Sagnac has been proposed and successfully demonstrated for this application [40]. This design is also advantageous because the number of components required to achieve optical switching is minimal, allowing for greater scalability and deployment. Switching occurs by magnetizing the MO material using the suitably designed coils and field generation system, achieving appropriate rotation of polarization for interference.

Traditionally, the MO material is placed at the center of a coil and is magnetized by passing current through this coil. To have fast switching capabilities, a coil of few turns is needed to minimize inductance. Although, this means that high current is required to generate a strong enough magnetic field. In this section a novel two-coil system is proposed that reduces the amount of current required for the magnetization field while still maintaining short optical rise times.

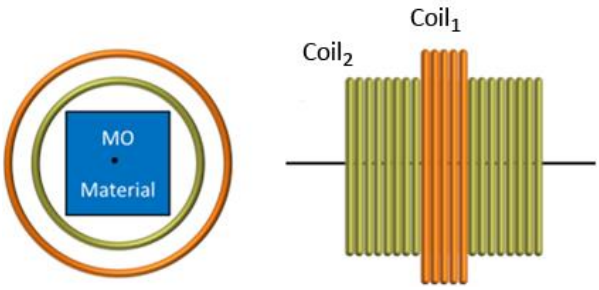

Figure 4.3: Dual coil magnetic field generator

The two coil system consists of $coil_1$ with N_1 turns and $coil_2$ with N_2 turns where $N_2 >> N_1$ (Figure 4.3). $Coil_1$ is wrapped around $coil_2$ coaxially and centered about its length. In this design, $coil_1$ has a low inductance which allows for fast initial magnetization of the MO material. $Coil_2$ uses much less current to maintain the same field strength for longer periods of time. Using both coils, optical signal routing is achieved with lower power dissipation than competitive designs.

4.3 Results

Given a turns ratio of 7:1, 28 gauge wire, and coil radii of 1.6 mm for the two-coil system, a current of 1 A through $coil_2$ of 21 turns and length 6.5 mm, and a maximum current of 4 A through $coil_1$ of 3 turns and length 1 mm, a total field of approximately 81 G through the MO material can be generated [13]:

$$B \approx \frac{\mu N_1 I_1}{\sqrt{l_1^2+4R_1^2}} + \frac{\mu N_2 I_2}{\sqrt{l_1^2+4R_2^2}} \qquad (4.1)$$

where N is the number of turns, I is the current, l is the length, and R is the radius of each coil. An optical rise time of 267 ns was achieved with both coils energized, which is competitive with contemporary switches. The total current required for this was significantly reduced in comparison to single coil configurations.

In the results shown (Figure 4.4), the optical signal sustains after the electrical pulses have turned off. This elongated fall time is a function of the MO material's

position between fiber ends in addition to the ringing seen in coil$_2$. Also, given the current through coil$_1$, if the current through coil$_2$, I_2, is increased too high, a secondary peak in the optical output begins to emerge near 2.5 µs. This peak becomes more prominent the higher I_2 is increased. The peak occurs due to coupling on coil$_1$ when coil$_2$ turns off, if I_2 is high enough. Therefore, a practical I_2 was chosen such that the optical response did not overly deteriorate and yet sufficient magnetization of the MO material could be achieved.

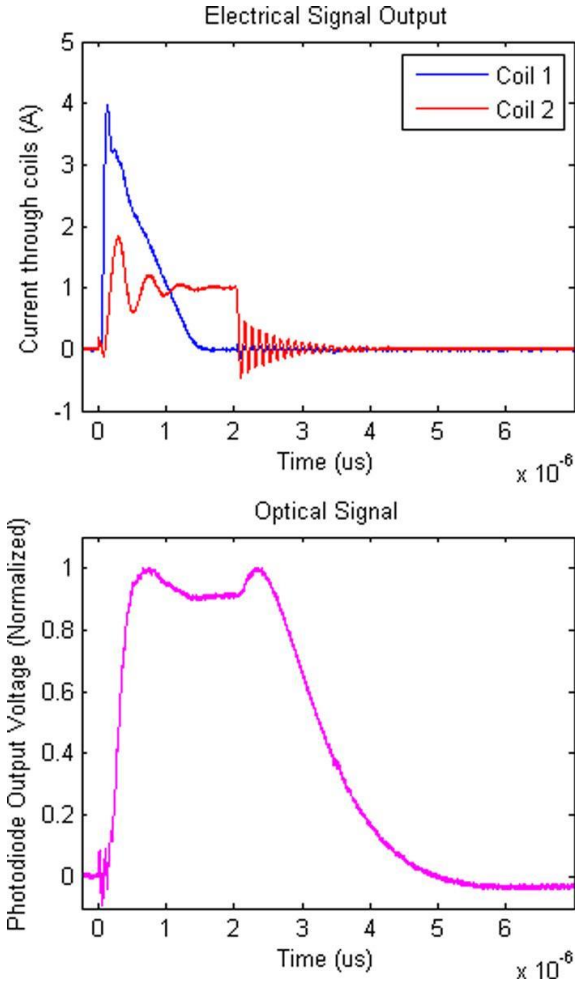

Figure 4.4: Measurements of the electrical and optical response

The measured coupling coefficient of the system was found to be approximately 0.8 for a turns ratio of 7:1. The turns ratio was chosen based on optimization of optical

rise time (due to large inductance) and size requirements given a specific wire gauge. In Figure 4.5, the effect of mutual inductance is shown. Here, the voltage across $coil_2$ is measured while $coil_1$ is energized, and also the voltage across $coil_1$ is measured while $coil_2$ is energized. From these figures it can be seen that coupling is most prominent in the former case. The coupling coefficient is found by dividing the peak coupled voltage by the source voltage, resulting in a coefficient of approximately 0.8 in this case. In addition, the ringing in $coil_2$ is a result of an RLC circuit consisting of the transistor capacitance, the inductance of the coil, and parasitic resistance. This ringing may be dampened by replacing D5 in the schematic with a resistor of value $\frac{V}{I_2}$ where V is approximately 40 V and I_2 is the current through $coil_2$.

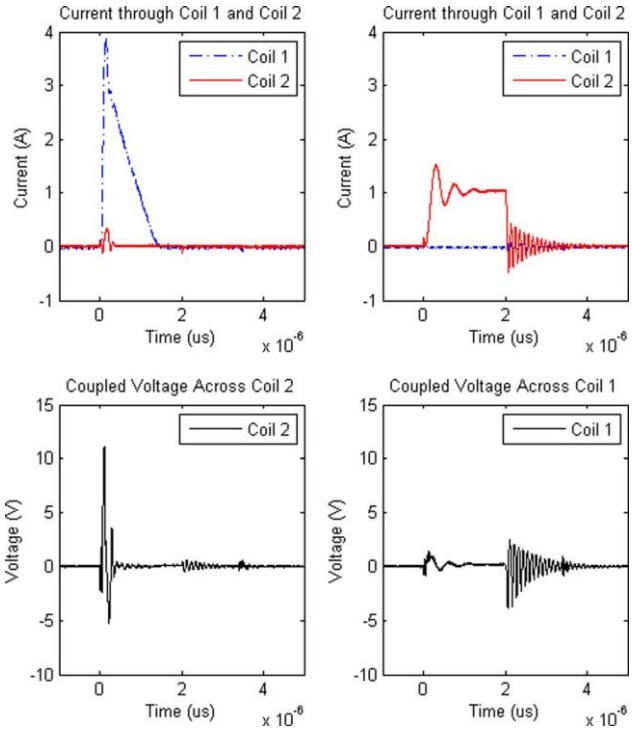

Figure 4.5: Coupled voltage across $coil_2$ (bottom left) while energizing $coil_1$ (top left) and coupled voltage across $coil_1$ (bottom right) while energizing $coil_2$ (top right)

4.4 Conclusion

A device that implements a new method of fiber-based magneto-optic switching has been realized that operates at powers lower than previous work. The two-coil system presented in this chapter can provide sufficient magnetization for Faraday rotators made of bismuth-doped iron garnet for optimal switching speeds. This proposed switching concept introduces new ideas and challenges that can be utilized for novel classes of deployable fiber-based magneto-optic switches.

CHAPTER 5

ENHANCEMENTS FOR HIGH SPEED OPERATION

Modified from the paper published in the *IEEE Transactions on Magnetics*

John W. Pritchard, Mani Mina, and Robert J. Weber

This chapter presents novel enhancements to the speed of fiber-based interferometric switches. Conventional drivers in MO switching devices utilize one coil with a low number of turns to quickly magnetize the MO material. This, in effect, leads to a fast optical rise time. However, the optical fall time is determined by the response of the MO material and the decay rate of any trapped magnetic energy in the coil, which can be sluggish. This can also be seen in the optical results shown in Figure 4.4 from Section 4.3. The proposed design achieves fast optical fall time by better controlling the demagnetization of the MO material. In this chapter, the design of the magnetic field generation system is presented and compared to other recently proposed systems, the electrical system is characterized, and the reliability of the optical output is investigated.

5.1 Optical Setup

The optical switch configuration utilizes the Sagnac effect, which is a phenomenon seen in ring interferometry (see Section 2.4.2) [41] [42] [43]. A diagram of this is shown in Figure 5.1. This was chosen over competitive switch configurations, such as the Mach-Zehnder interferometer (see Section 2.4.1), due its stability over temperature and low number of required components [9] [10]. The MO material is placed between two fibers in the Sagnac loop, such that the fiber length on either side of the material is the same. The coils for magnetic field generation are placed appropriately around it.

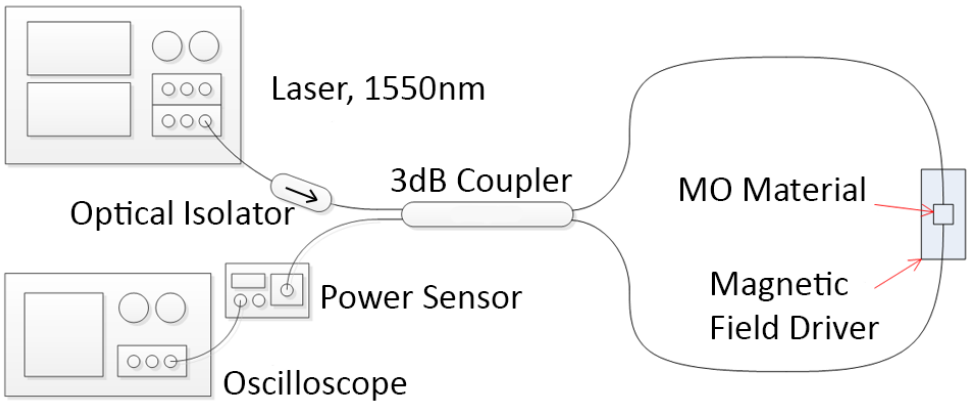

Figure 5.1: Fiber-based magneto-optic Sagnac interferometer setup

The optical components used include a tunable laser, optical coupler, optical isolator, InGaAs photodetector (power sensor), and oscilloscope. The operating wavelength chosen was 1550nm, thus a suitable power sensor was selected to analyze the optical output signal. Also, an appropriate MO material was selected, given by the chemical equation $[(Bi_{1.1}Tb_{1.9})(Fe_{4.25}Ga_{0.75})O_{12}]$ [23], such that it is transparent (without application of magnetic fields) at the operating wavelength.

5.2 High Speed Driver Circuit

In a typical MO interferometer, phase shift for interference is achieved by appropriate placement of MO material. Magnetized MO material results in the optical output at one of two output ports, while demagnetized MO material results in the optical output at the other port. The field generation system controls the magnetization of the MO material, and thus the selection of the optical output port. The driver utilizes two MOSFET devices with two respective coils, represented schematically by a transformer (Figure 5.2).

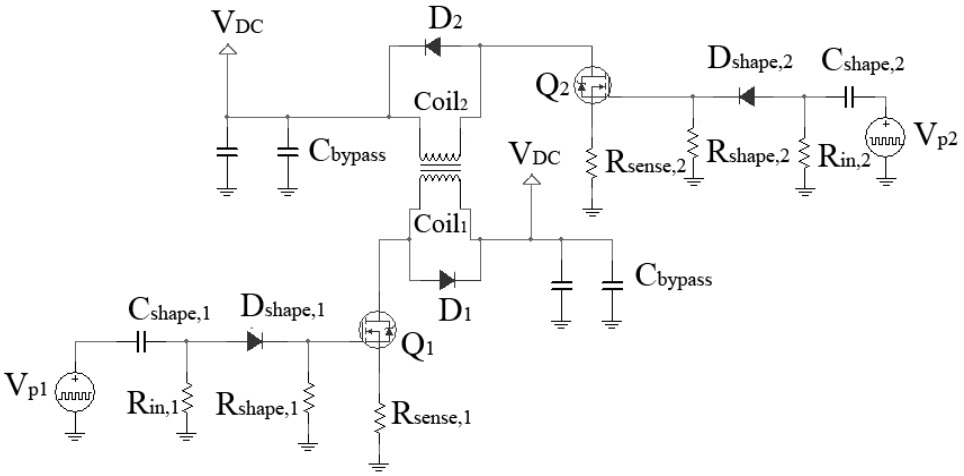

Figure 5.2: Field Generation Driver

Pulse source V_{p1} is used to activate MOSFET Q_1, providing a fast, high amplitude current pulse to $coil_1$, quickly magnetizing the MO material. The voltage profile at the gate is achieved by placing $C_{shape,1}$ in series with the gate of the Q_1. To eliminate the negative pulse at the falling edge of V_{p1}, a fast switching diode, $D_{shape,1}$, is placed in series. Resistor $R_{in,1}$ is placed in parallel for input impedance matching, and $R_{shape,1}$ provides a return path to ground for the gate signal.

Pulse source V_{p2} is triggered immediately after the falling edge of V_{p1}. It is used to activate Q_2, providing current to $coil_2$, quickly demagnetizing the MO material and neutralizing any trapped magnetic energy from the initial pulse. The electronic components are placed similarly as before. A series capacitor $C_{shape,2}$, series diode $D_{shape,2}$, and parallel resistor $R_{shape,2}$ are placed such that the gate signal to Q_2 is shaped appropriately. Resistor $R_{in,2}$ is placed in parallel for input impedance matching.

The challenges in creating the field generation system were primarily focused on optimizing the coil design, efficiently transferring magnetic energy, and minimizing parasitics. The coils were uniquely designed to allow the MO material to experience the most uniform field for each magnetic pulse. Several different coil configurations were considered and experimented with [31], but an intertwined design has shown to be the most effective, as illustrated in Figure 5.3.

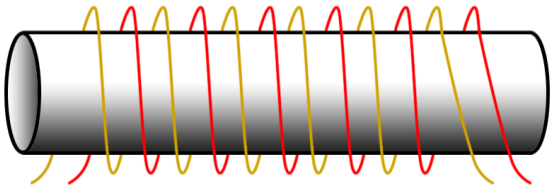

Figure 5.3: Two-Coil Field Generator

In this design, two wires are wound in parallel around a zirconia universal mating sleeve. This sleeve is a guide for the ends of optical patch cables, designed to precisely align the fiber. In this case, the two ends of the optical coupler in the Sagnac setup are fitted in this sleeve, with the MO material placed in-between (Figure 5.4).

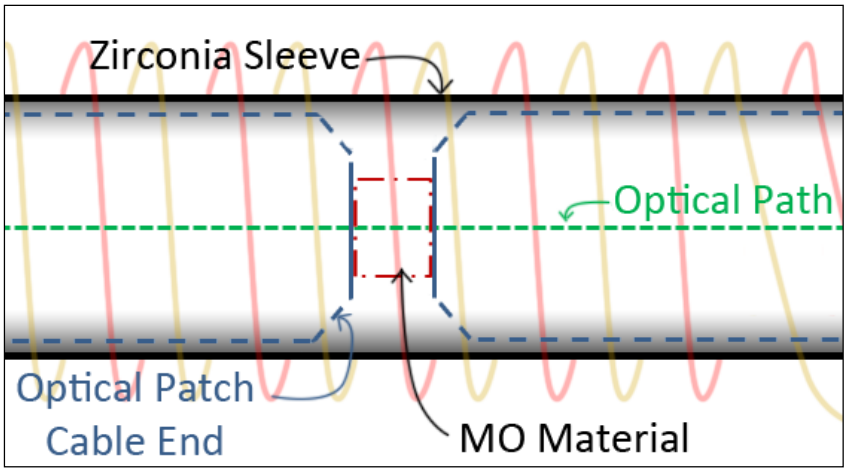

Figure 5.4: MO material between two optical patch cable ends, fitted within the mating sleeve

In creating a fast magnetic pulse, it is not uncommon to see trapped magnetic energy in the coil after its respective MOSFET switch has turned off. This issue can be addressed by placing a low-value resistor in series with the protection diode across the coil. In addition, the reverse field applied after the initial pulse can be used to neutralize this trapped energy, superimposing the fields such that the net field through the MO material is zero.

5.3 Magnetic Field Generation

V_{p1} has a pulse width of about 110 ns with a rise and fall time near 50 ns in both experiments, and V_{p2} also has a pulse width of about 110 ns with a rise and fall time near 50 ns when energized.

The passive components were chosen to appropriately generate the required magnetic field. For the gate signal shaping, $C_{shape,1} = C_{shape,2} = 10nF$, $R_{in,1} = R_{in,2} = 50\Omega$, $R_{shape,1} = R_{shape,2} = 100\Omega$, and $R_{sense,1} = R_{sense,2} = 1\Omega$. The current through each coil can be determined by measuring the voltage across the current sense resistors ($R_{sense,1}$ and $R_{sense,2}$).

The field through the MO material is calculated for each coil using the following equation [13]:

$$B \approx \frac{\mu_0 NI}{\sqrt{l^2+4R^2}} \qquad (5.1)$$

where N is the number of turns, I is the current through the coil, R is the radius of the coil, and l is the length of the coil. The relative permeability of the material is assumed to be unity for practical purposes.

For the initial pulse using $coil_1$, a 6-turn, 4.4 mm long coil with a radius of 1.6 mm achieved a maximum field near 83.2 G with a peak current of approximately 6 A. This field strength was great enough to attain sufficient Faraday rotation for an observable optical output. For the reverse field, a coil of the same number of turns and dimensions with a peak current of 3.2 A produced a maximum field near 44.3 G.

5.4 Electrical and Optical Results

Optical output due to the application of magnetic fields is shown in Figure 5.5 and Figure 5.6. Figure 5.5 shows the result of two experiments in the presence of the MO material: optical output when $coil_1$ is energized and $coil_2$ is turned off and optical output when both $coil_1$ and $coil_2$ are energized. Figure 5.6 shows optical output as a

result of energizing $coil_1$ and $coil_2$ in the absence of the MO material, for reference. In addition, optical output is also shown energizing only $coil_1$ in the presence of the MO material with and without $coil_2$. Consequently, it is determined that the presence of $coil_2$ results in a 10% decrease in the peak amplitude of the optical output with little effect on the rise and fall times. The data was normalized in these figures based on the greatest peak of the respective traces to show relative scale. The optical signals measured are averaged over a 16-sample window.

Using this method of field generation, the potential speed of the MO switch can be increased. As shown in Figure 5.5, the proposed switch significantly reduces the optical fall time. The fall time is calculated by taking the difference in time where the amplitude has reached 90% of the maximum and 10% of the maximum for the falling edge of the pulse. This value was found to be 739 ns without the reverse field applied and 129 ns with the reverse field applied. The rise time is calculated similarly and this value was found to be 77 ns without the reverse field applied and 82 ns with the reverse field. Thus, the overall pulse width has been reduced. Assuming the duty cycle can approach 100%, the switching speed can be improved. However, trapped magnetic energy in the coil can then be problematic.

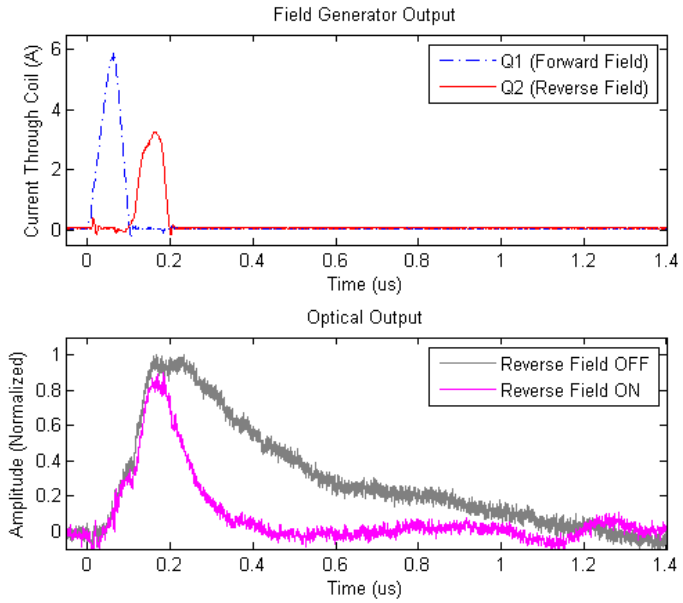

Figure 5.5: Electrical output (top) and optical results including MO material without reverse field applied (gray) and with reverse field applied (magenta)

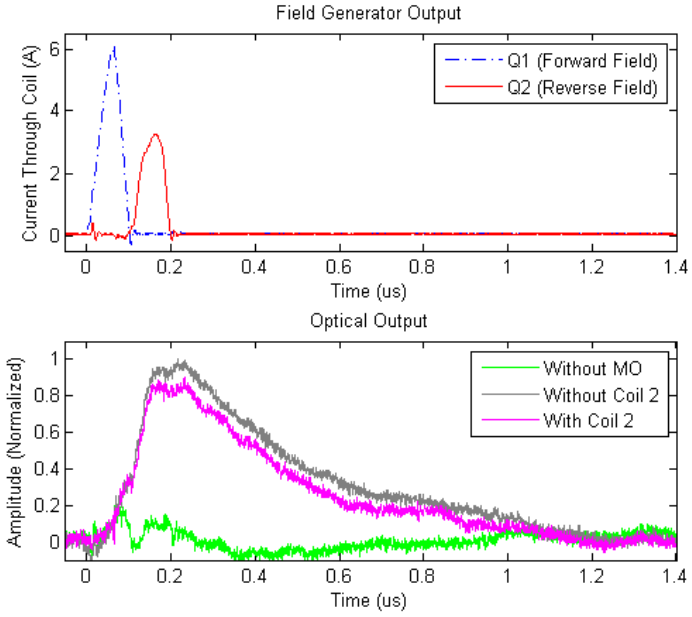

Figure 5.6: Electrical output (top) and optical output (bottom) showing the contribution of coil$_2$ and effects of the absence of the MO material

5.5 Dominant Effects

The effect dominating the lengthy optical fall time may primarily be due to the trapped magnetic energy in $coil_1$ after Q_1 has turned off. In some cases, when the reverse field is applied, a small perturbation in the optical output can be seen well after the optical switching pulse (Figure 5.7).

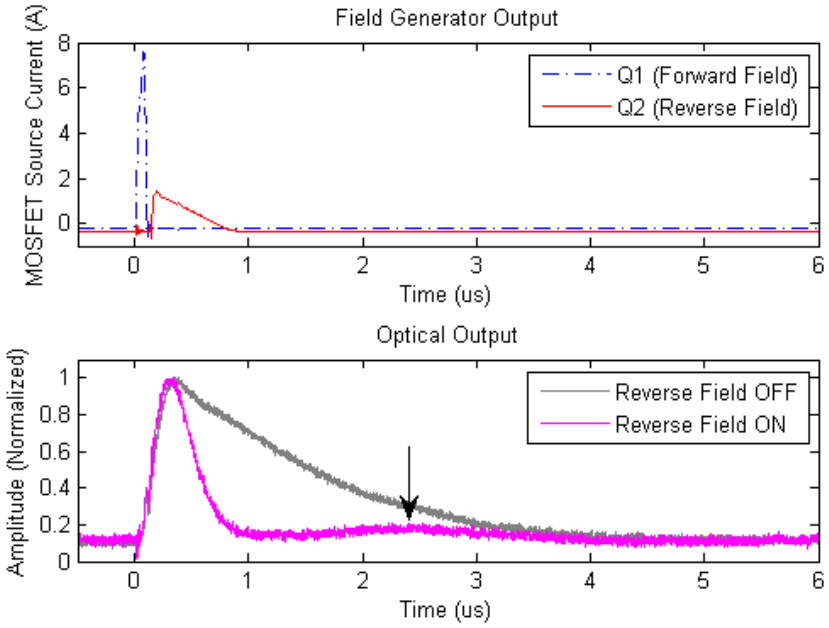

Figure 5.7: Optical output indicating perturbation

In Figure 5.7, it is shown that after a low amplitude reverse field has been applied, the optical fall time is reduced as before. However, at approximately 2.5 µs a slight perturbation can be seen and is indicated by a black arrow. This is a result of the reverse field not fully neutralizing the trapped magnetic energy in $coil_1$. The trapped energy is an effect of the coil inductance, bypass capacitance, and their inherent resistance. These effects can ultimately limit the switching speed of this device. This effect can be reduced by choosing suitable components with low equivalent series resistance. In addition, effects of coupling can be seen by looking at the voltage across each coil while the other is energized. In the following experiment the voltage across each coil is monitored

continuously. $Coil_1$ was energized as well as $coil_2$ immediately after. The results show that the coupling coefficient is approximately 0.8. This was determined by dividing the maximum voltage across the coupled coil (while the other was energized) by V_{DC}. The effects of coupling on each coil are illustrated in Figure 5.8. Additionally, the optical output was observed with and without the presence of $coil_2$ to determine if mutual inductance was a cause of the trapped magnetic energy. However, results showed insignificant change in the optical rise and fall times.

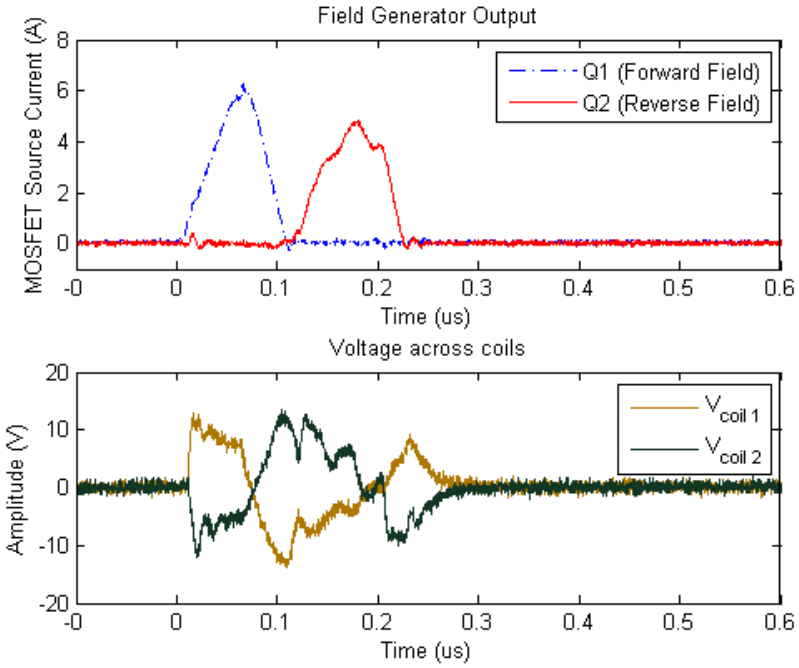

Figure 5.8: Coupling effects on each coil

5.6 Conclusion

In this chapter, a novel method for magnetic field generation that enhances the switching time of MO switching technologies was presented. It was found that optical fall time can be optimized by applying a reverse magnetic field through the magneto-optical element. Also, it was found that the effects that dominate the extended optical fall time are due to trapped magnetic energy in the coil due to the initial magnetic

pulse, not necessarily the response of the MO material. The field generation system was introduced and discussed and compared to other newly proposed electric drivers. The electrical system was analyzed, improved optical results were demonstrated, and additional experimentation was suggested.

CHAPTER 6

ENHANCING SENSITIVITY

Modified from the paper published in the *IEEE Magnetics Letters*

John W. Pritchard and Mani Mina

All-optical resonators have shown to be candidates for next-generation integrated optical switching devices for communication purposes. Their simplicity in design can allow for easy integration using standard CMOS fabrication processes. Other switch configurations, such as the Mach-Zhender and the Sagnac, have been implemented but are more complicated. Traditionally, optical resonators have been used as optical all-pass filters. However, by including a Faraday rotator in the resonating loop with an actuating field, an all-optical switch can be realized. Optical resonator switches have often been proposed and implemented utilizing the electro-optic effect. This chapter reveals that magneto-optic equivalents show promise as alternatives. Therefore, a magneto-optical switch of resonator configuration is proposed and implemented with theoretical analysis using the Jones calculus technique. Preliminary experimental results are presented.

6.1 Formulation and Theory of Operation

The optical resonator configuration with the MOFR element is shown in Figure 6.1. This fiber-based device utilizes a 3dB coupler, connecting ports 2 and 4 with the MOFR placed at the midpoint of the resonator loop. The resonator interferometric configuration differs from configurations such as the Sagnac in that the interfering signals at the output have a relative phase that is dependent on the path traveled in the resonant loop. This section provides a brief theory of operation with a numerical solution. For a more extensive description of the formulation, see Section 2.4.3.

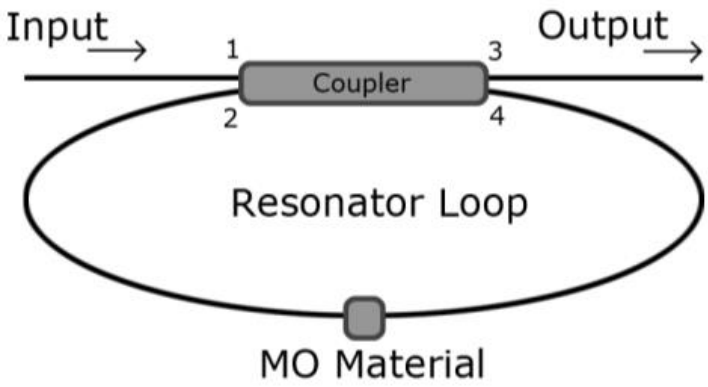

Figure 6.1: Fiber-based resonator with MO material placed at the midpoint of the resonator loop.

6.1.1 Jones Calculus Approach

Jones calculus can be used to solve optical circuits [29]. Each element in the circuit is represented by a Jones vector or Jones matrix. As shown in Equation 6.1, the optical 3dB coupler can be represented by a Jones matrix to solve for the optical output at ports 3 and 4, given an input signal at ports 1 and 2.

$$\begin{bmatrix} \vec{E}_{3o} \\ \vec{E}_{4o} \end{bmatrix} = \frac{1}{\sqrt{2}} \begin{bmatrix} 1 & j \\ j & 1 \end{bmatrix} \begin{bmatrix} \vec{E}_{1i} \\ \vec{E}_{2i} \end{bmatrix} \quad (6.1)$$

The MOFR can also be represented by a Jones matrix, which acts on the x- and y-component of the incident electric field. The optical signal that has exited port 4, traversed through the MO material and entered port 2 is represented by Equation 6.2.

$$\begin{bmatrix} E_{2i,x} \\ E_{2i,y} \end{bmatrix} = Te^{j\Phi} \begin{bmatrix} \cos\theta_F & -\sin\theta_F \\ \sin\theta_F & \cos\theta_F \end{bmatrix} \begin{bmatrix} E_{4o,x} \\ E_{4o,y} \end{bmatrix} \quad (6.2)$$

Here, $E_{2i,x}$ and $E_{2i,y}$ represent the x- and y-components of the electric field entering port 2 respectively, T represents the transmission coefficient, Φ represents the phase shift due to traversing the resonator loop, $E_{4o,x}$ and $E_{4o,y}$ represent the x- and y-components of the electric field exiting port 4 respectively, and θ_F represents the degree of Faraday rotation, which can be related to the applied field strength.

In this formulation, two solutions are provided for comparison: the output of the resonator configuration without the MOFR element placed in the resonator loop [44], and the output with the MOFR element included. It can be verified that the output with zero field applied to the included MOFR is equivalent to the output without the MOFR included.

6.1.2 Optical Output without MOFR

Considering the absence of MO material, it is shown that the optical output can be solved using the Jones calculus technique. Assuming that port 1 has an input amplitude E_{1i} and port 2 has an input amplitude E_{2i}, the Jones vector for the output port 4 can be solved for, and as a result the E_{2i} can be redefined as

$$\vec{E}_{2i} = T\vec{E}_{4o}e^{j\Phi} = \frac{\frac{jTe^{j\Phi}}{\sqrt{2}}}{1-\frac{T}{\sqrt{2}}e^{j\Phi}}\vec{E}_{1i}\,, \tag{6.3}$$

where T is the transmission coefficient, E_{4o} is the signal exiting port 4, and $e^{j\Phi}$ is the change in phase due to traversing the resonator loop. The result in Equation 6.3 can then be used to solve for the signal exiting port 3 (output), which is given by Equation 6.4.

$$\vec{E}_{3o} = \frac{\vec{E}_{1i}}{\sqrt{2}}\left(1 - \frac{\frac{T_1e^{j\Phi}}{\sqrt{2}}}{1-\frac{T_1}{\sqrt{2}}e^{j\Phi}}\right) \tag{6.4}$$

6.1.3 Output Including MOFR

By including the magneto-optic material, the formulation becomes more involved. However, a similar approach can be used.

Using Equations 6.1 and 6.2, the resulting output at port 3 is

$$\begin{bmatrix}E_{3o,x}\\E_{3o,y}\end{bmatrix} = \frac{1}{\sqrt{2}}\left(1 - A_0\begin{bmatrix}\cos\theta_F - \frac{Te^{j\Phi}}{\sqrt{2}} & -\sin\theta_F\\ \sin\theta_F & \cos\theta_F - \frac{Te^{j\Phi}}{\sqrt{2}}\end{bmatrix}\right)\begin{bmatrix}E_{1i,x}\\E_{1i,y}\end{bmatrix}, \tag{6.5}$$

where

$$A_0 = \frac{\frac{Te^{j\Phi}}{\sqrt{2}}}{\left(\cos\theta_F - \frac{Te^{j\Phi}}{\sqrt{2}}\right)^2 + \sin^2\theta_F}\ .$$

Equation 6.5 is the general solution to the output at port 3, for any θ_F. If $\theta_F = 0$, $\vec{E}_{3o}$ becomes

$$\begin{bmatrix} E_{3o,x} \\ E_{3o,y} \end{bmatrix} = \frac{1}{\sqrt{2}}\left(1 - \frac{\frac{Te^{j\Phi}}{\sqrt{2}}}{1-\frac{Te^{j\Phi}}{\sqrt{2}}}\begin{bmatrix} 1 & 0 \\ 0 & 1 \end{bmatrix}\right)\begin{bmatrix} E_{1i,x} \\ E_{1i,y} \end{bmatrix}, \qquad (6.6)$$

which is the same as that found in Equation 6.4.

Assuming $\Phi = 0$ for convenience, the result of this formulation shows that as θ_F is increased linearly, there is a nonlinear rotation in the state of polarization (SoP) of E_{3o} (Figure 6.2). This implies that a small initial degree of Faraday rotation can lead to a greater overall rotation of the SoP of the input wave.

As Φ changes, the output magnitude changes according to Equation 6.5. This results in a variation of the output power, as a function of Φ and θ_F (Figure 6.3). Thus, in designing the resonator to have suitable interference at the output, the path length of the resonant ring should be designed such that Φ results in the greatest difference in output magnitude due to small changes in θ_F (and thus, field applied). For a 40° variation of Faraday rotation, this formulation suggests that a Φ resulting in the greatest change in output power is π/10 (given by the third black arrow).

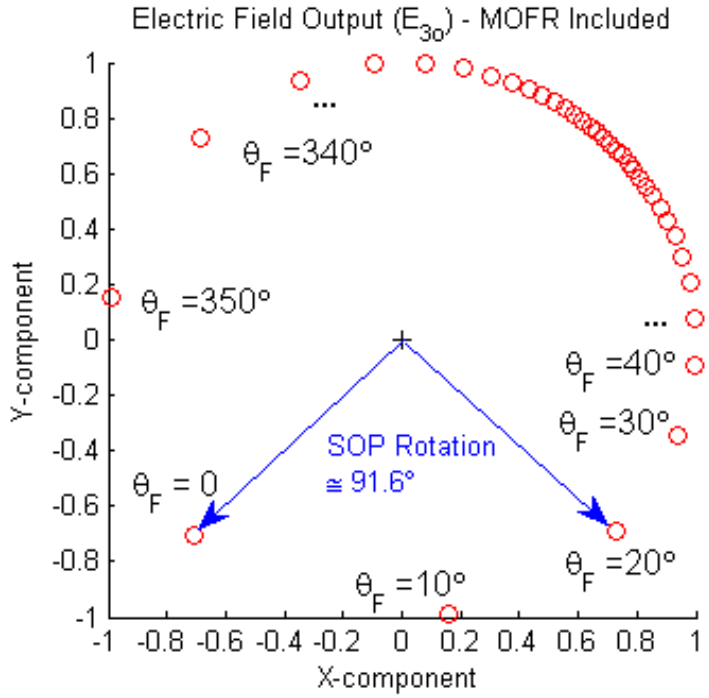

Figure 6.2: Electric field components of the optical output showing nonlinear rotation in the SoP due to applied magnetic field. A Faraday rotation of 20° corresponds to a 91.6° rotation of the SoP at the output.

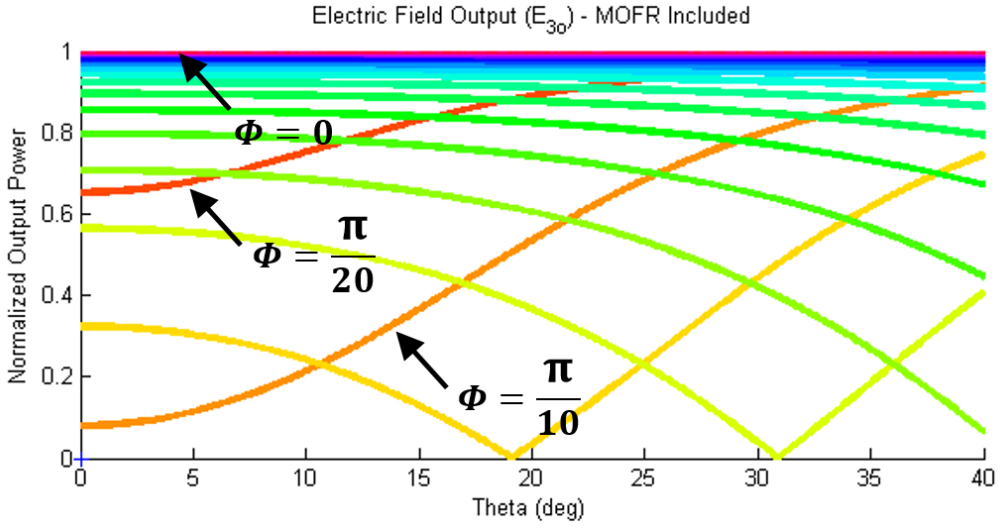

Figure 6.3: Relative output power as a function of θ_F for different values of Φ (increments of π/20).

6.2 Experimental Setup

In this fiber-based optical resonator design, a laser at 1550nm serves as the input signal and an optical isolator is placed in-between it and the interferometer to prevent unwanted reflections. Polarizers are placed on both sides of the resonator as described. An InGaAs photodetector is used to detect the 1550nm optical output, and an oscilloscope displays the result (Figure 6.4).

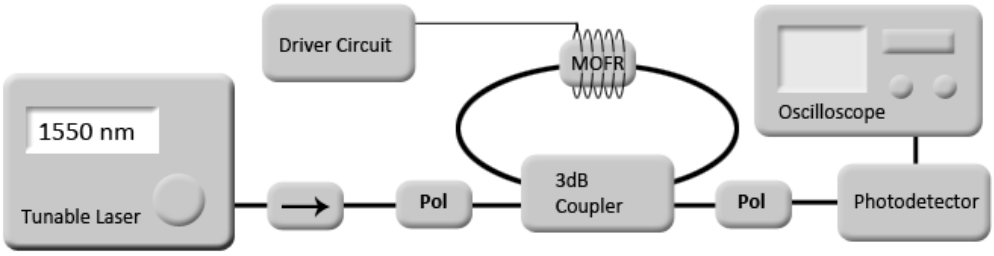

Figure 6.4: Experimental setup showing the 1550nm laser source, isolator, polarizers, resonator switch, photodetector, and oscilloscope.

Specialized coils are wrapped around a zirconia tube that, for alignment, houses both the MOFR and the optical connectors. Two 330µm thick sections of the MO material are placed back-to-back to achieve sufficient Faraday rotation. Index matching gel is used at the MO interfaces to minimize insertion loss and re-reflections. The coil is electronically driven and serves to magnetize the MOFR.

The MOFR chosen is a bismuth-doped iron garnet (BIG) with the chemical equation $[(Bi_{1.1}Tb_{1.9})(Fe_{4.25}Ga_{0.75})O_{12}]$ [23]. This was chosen based on the low required field strength to achieve rotation. Other materials were considered, but the BIG was best suited for this application.

6.3 Field Generation

To magnetize the MO material, a field generation system is required. This was completed using two coils wrapped in an intertwine configuration around the thin

zirconia tube housing the MO material. The optical path penetrates the MO material while still being well aligned with the fiber core. This system has shown to be suitable for fast magneto-optic switching technologies, and thus was implemented as described in [15].

The circuit that drives the two coils includes two MOSFETs whose gate signal is shaped appropriately for optimal switching (Figure 5.2). The second coil in the two-coil configuration was used in order to neutralize any residual field after the first coil has turned off. It has been shown that the residual field is a result of an LRC configuration between the coil inductance and the diode capacitance. This can be further reduced by choosing suitable components with low equivalent series resistance [15]. The equation for magnetic flux generated is shown in Equation 5.1.

6.4 Results and Discussion

Using the field generator and experimental setup described, optical output was obtained (Figure 6.5). A representation of the forward and reverse magnetic field through the MO material is shown. The reverse field is applied immediately after the forward field to quickly demagnetize the MO material and neutralize any residual field due to the LRC effects.

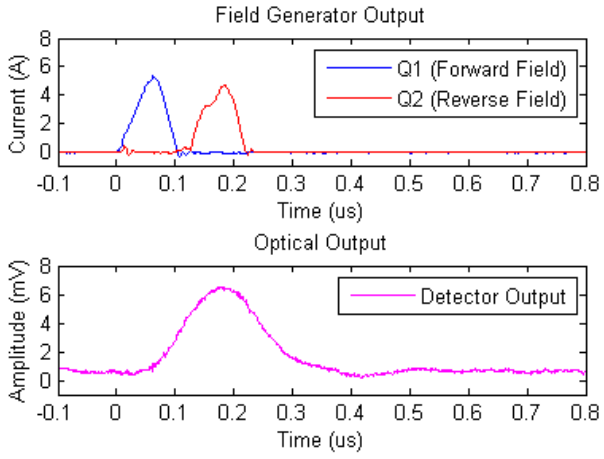

Figure 6.5: Electrical (top) and optical (bottom) results.

The particular MOFR used has a saturating magnetic field of 225 Oe for the full 45 degree rotation of SoP. Assuming a linear relationship between the applied field and degree of Faraday rotation, 5 Oe will result in 1 degree of rotation. For the coil configuration used as described by [15], the field generated for a 6 A peak current is approximately 83.2 Oe, which corresponds to approximately 16.6 degree of Faraday rotation. Using the proposed formulation, the output wave at port 3 is rotated nearly 80 degrees with respect to its SoP without an applied field.

The resulting optical pulse has a rise time of 80.6ns and fall time of 119.7 ns (which was calculated as the time the signal took to rise or fall 10%-90% of the maximum). The pulse width using full width at half maximum (FWHM) is found to be 152 ns. In addition, the insertion loss and isolation ratio at the operating wavelength were measured to be 8.9 dB and 15.6 dB, respectively. These results provide a proof of concept, showing that a MO switch of resonator configuration is a candidate for alternative all-optical switching solutions.

6.5 Conclusion

In this chapter, a magneto-optic interferometric switch of resonator configuration was proposed, and experimental results were provided. As magneto-optic switching technologies advance, it is desired to reduce size, power consumption, and switching time. This work showed that a ring resonator with a MOFR placed in the resonant loop can allow for large rotation of the state of polarization of the output wave with small degree of Faraday rotation. Such findings can lead to magneto-optic switches having faster transition time with lower field applied to the MO material. The formulation developed for theoretical analysis in this work uses the Jones calculus technique. Experimental results found that the resonator switch obtained an optical pulse width near 152 ns. A specialized field generator which utilizes a two-coil configuration was used, and electrical and optical results were presented.

CHAPTER 7

DIFFERENTIATION OF MO ROUTING TOPOLOGY

Modified from the paper published in the *IEEE Transactions on Magnetics*

John W. Pritchard, Mani Mina, and Prabesh Dulal

In Chapter 3 – Chapter 6, the magneto-optic (MO) material used had very low coercivity, and thus required relatively low applied magnetic field strength. In this chapter, a novel fiber-based MO latching circuit is presented which utilizes a bismuth-substituted yttrium iron garnet (Bi:YIG) having high coercivity (thus increased applied field is required). Experimentation shows that nearly 90 degrees of rotation of the state of polarization (SoP) of incident light occurs between material latching states upon application of an external magnetic field greater than 500 G. This amount of rotation is enough to cause sufficient routing at the output of an optical interferometer of Sagnac configuration. Due to the high coercivity of the Bi:YIG, the material remains in its magnetized state for very long periods of time and is thus "latched." Reversing the applied magnetic field changes the state of the material, "unlatching" it. This capability has great importance for nonreciprocal all-optical devices requiring low power operation. In addition, having such control of the state of the non-reciprocal elements can allow for a wider diversification of small-scale and large-scale optical network design. A discussion of the experimental setup, the resulting measurement data, and its implication for future low power applications is presented.

7.1 Experimental Setup

A fiber-based interferometer of Sagnac configuration was created and base measurements were recorded without the insertion of the MO material. The Bi:YIG was then placed in a the Sagnac loop and the material's magnetized state was toggled. The

power at the output ports of the interferometer were observed and recorded to show that two latched states could be achieved and utilized for optical routing.

7.1.1 Latching Material Principle of Operation

The Bi:YIG used in this study does not require the use of a bias magnet to cause Faraday rotation, and has domain dimensions on the order of 100 µm [24] [45]. Applying a pulsed magnetic field higher than 500 G oriented normal to the surface of the material will latch the domain in the applied field direction (Figure 7.1). Infrared light travelling through the material in this latched state will experience Faraday rotation, without the presence of a bias field. When the applied magnetic field pulse is reversed, the domain latches in the opposite direction as previous, and a different, oppositely oriented Faraday rotation is experienced (Figure 7.2). Here, the switching field latches the domain to a new direction and no bias field is required for incident light to experience Faraday rotation.

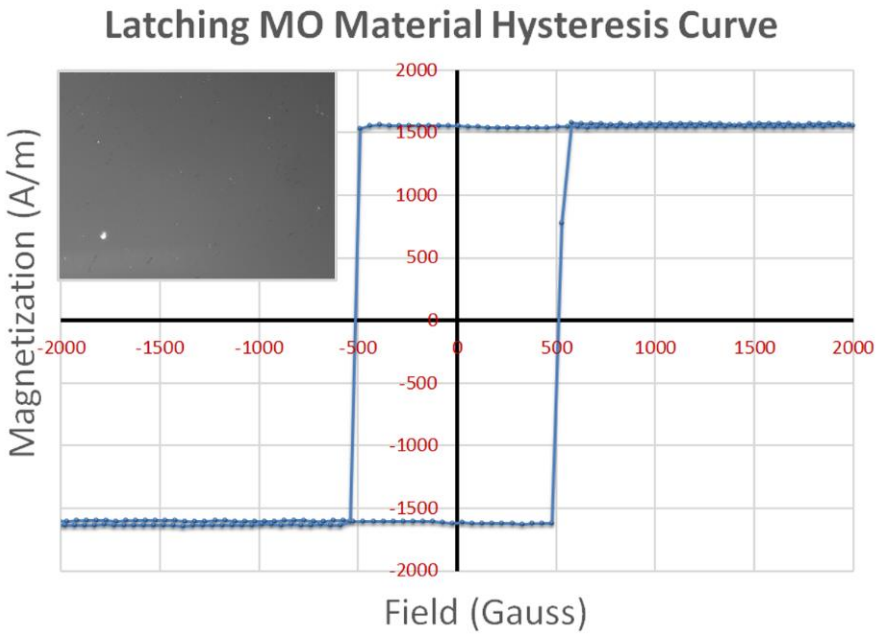

Figure 7.1: Measured hysteresis in latching Bi:YIG with MOKE image showing enlarged single domain (240 µm x 180 µm view at 20x magnification)

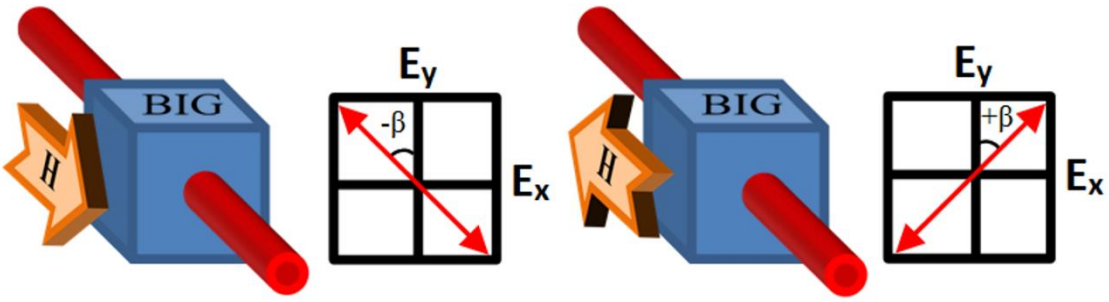

Figure 7.2: Latching material principle of operation

Given a magnetized state of the material, the resulting polarization once the light has exited the material can be measured using a polarization controller and power meter. When the magnetization state has latched to its opposite direction and the new polarization state is determined, the difference in the resultant SoP's can be calculated.

7.1.2 Faraday Rotation

A polarimeter can be used to get an initial estimate of the specific Faraday rotation of the Bi:YIG. A simplified version consists of an optical isolator, polarizer, MO material (Bi:YIG), polarization controller, and power meter (Figure 7.3). The polarization controller can be programmed to sweep from 0 to 360 degrees with 1 degree increments and the output power per degree can be reported. The difference in the SoP rotation for differently magnetized states can lead to the overall specific Faraday rotation.

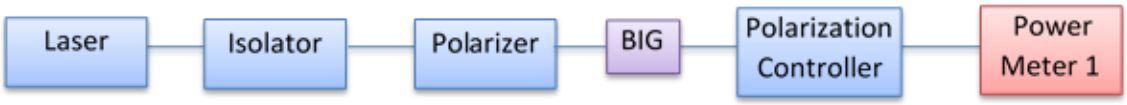

Figure 7.3: Simplified polarimeter setup

In addition, polarimeters that achieve similar goals use a polarization beam splitter (PBS) after light has exited the material to extract transvers-electric (TE) and transverse-magnetic (TM) information from the wave. Observing the phase shifting

behavior of the TE and TM waves can also lead to very accurate specific Faraday rotations.

The resulting specific Faraday rotation parameter was measured by Integrated Photonics, Inc. The reported value for the latching material used is –93 °/mm at 1550 nm. Since the purchased material is 485 µm thick, the Faraday rotation is approximately +/–45°, depending on the state of magnetization (due to a forward or reverse applied field). This material (at λ = 1550 nm) also has an index of refraction of 2.317, temperature coefficient of –0.093 deg/°C, and wavelength dispersion of –0.068 deg/nm [45].

7.1.3 Sagnac Interferometer

The Sagnac interferometric routing configuration was chosen due to its stability over temperature and over device size [8]. It utilizes a single 3 dB coupler with an optical circulator to route the returning signal (Figure 7.4). The MO material is placed at the center of the Sagnac loop, and an applied magnetic field activates the material creating interference at the output. The outputs at port 1 and port 2 are related using the following equation, assuming only port 1 of the coupler has an input signal [9]:

$$\begin{bmatrix}\vec{E}_{1o}\\ \vec{E}_{2o}\end{bmatrix} = Te^{j\phi}\begin{bmatrix}(jE_{1i,x}cos\theta_F)\hat{x} + (jE_{1i,y}cos\theta_F)\hat{y}\\ (-E_{1i,y}sin\,\theta_F)\hat{x} + (E_{1i,x}sin\theta_F)\hat{y}\end{bmatrix} \quad (7.1)$$

where T is the transmission coefficient, ϕ is the phase change due to path traveled, θ_F Faraday rotation, $\vec{E}_{1o}$ and $\vec{E}_{2o}$ are the electric field outputs at ports 1 and 2, respectively, and $E_{1i,x}$ and $E_{1i,y}$ are the x- and y-components for the input of port 1, respectively. An in-depth discussion of this interferometer type is provided in Section 2.4.2.

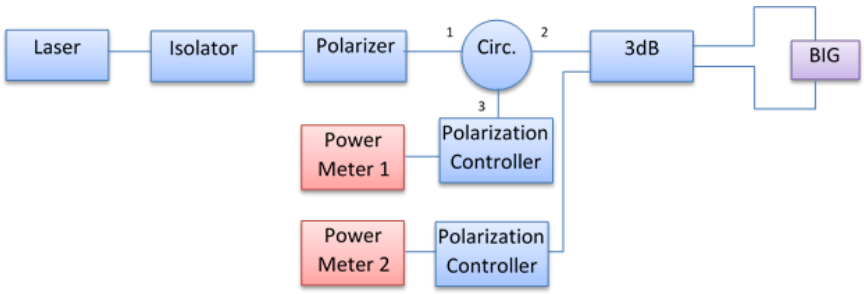

Figure 7.4: Sagnac interferometer setup

The output power at each port can be estimated by the following equation:

$$P = \frac{E^2}{2\eta} \qquad (7.2)$$

where E is the magnitude of the electric field, η is the wave impedance defined as $\eta = \frac{120\pi}{\sqrt{\varepsilon_r}}$, and ε_r is the relative permittivity of the waveguide.

The output power can be related to the Faraday rotation according to the formulation provided (Equations 1–2). Assuming $T = 1$ and $\phi = 0$ for convenience, the normalized output of the Sagnac interferometer can be determined (Figure 7.5). In this plot, output power is maximized at port 1 and minimized at port 2 when 0° of Faraday rotation occur. Similarly, the output is nonzero at port 2 and zero at port 1 for a Faraday rotation of 90°. Thus, ideal optical routing occurs when one state of the material observes 0 degrees Faraday rotation, and another observes 90 degrees (each port exhibits its maximum and minimum output). However, the particular Bi:YIG used reports a –45° to +45° rotation upon magnetization as opposed to a 0° to +90° rotation. Thus, alternative methods of obtaining sufficient output need to be determined.

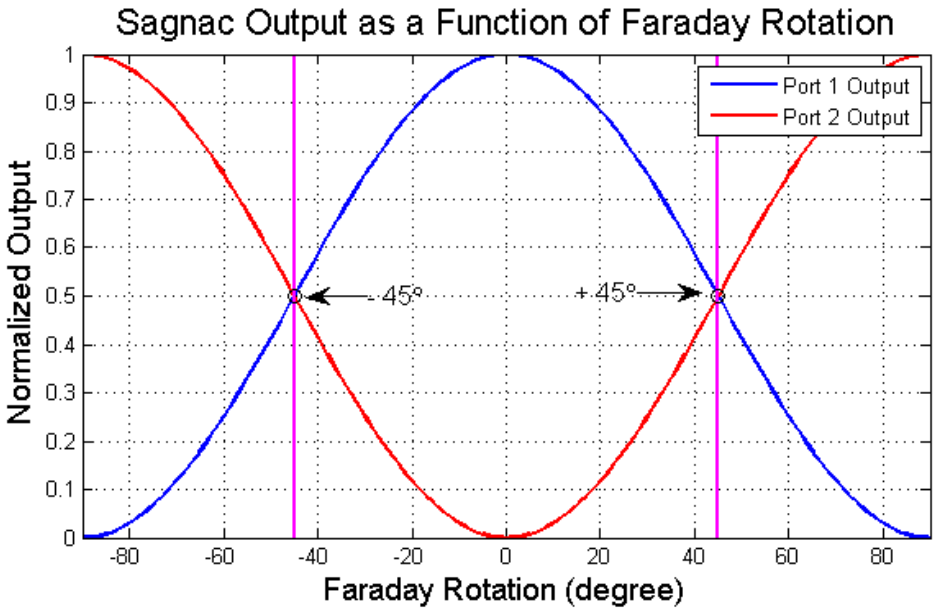

Figure 7.5: Normalized output (calculated) of Sagnac indicating Faraday rotations of –45° and +45°

7.1.4 Material and Interferometer Considerations

The theoretical formulation for the Sagnac interferometer shows that the output power given +45° and –45° of Faraday rotation should be equal at each port. If the power is expected to be the same at each port for each latching state of the material, this would indicate that no optical routing would be observed at the Sagnac outputs. However, since the output polarization shifts to such a degree, polarization beam splitters (PBS) can be used to create new outputs.

7.2 Results and Discussion

The Bi:YIG, approximately 485 µm thick, was inserted in the Sagnac loop. An axially magnetized ring magnet was used to magnetize the MO material in a particular direction. Measurements were recorded, and the magnet was then used to reverse the magnetization direction of the material. Measurements were again recorded, reported, and compared to the output without material included in the system (Table 3). This output is consistent with the formulation provided (Figure 7.5).

Table 3: Latched and unlatched optical output measurements

Input power (λ=1550 nm)	**Output power, no MO material**
3.5 dBm	(port 1) **–4.95 dBm** (port 2) **–14.6 dBm**
Input power (λ=1550 nm)	**Output power, state 1 (latched)**
3.5 dBm	(port 1) **–12.1 dBm** (port 2) **–12.2 dBm**
Input power (λ=1550 nm)	**Output power, state 2 (unlatched)**
3.5 dBm	(port 1) **–12.2 dBm** (port 2) **–12.0 dBm**

Although these measurements agree to the formulated output, no latched routing is observed from this perspective. It is then of interest to investigate the resultant output polarizations. A polarization controller was placed at port 2 and after the polarizer to analyze the degree of rotation observed at the Sagnac output upon latching and unlatching the material.

Results of studying the output polarization are provided (Figure 7.6, Figure 7.7). Upon latching and unlatching the material, the output at port 2 results in a rotation of +45° and – 45° degree Faraday rotation. Thus, a polarization beam splitter can be used at the output of port 2 to utilize the routing capability that the latched material provides.

Due to the fiber-optic path lengths, number of fiber-fiber and fiber-Bi:YIG interfaces, insertion loss is approximately 15.6 dB and would be nearly 18.6 dB given a 3 dB polarization beam splitter. Additionally, due to persistent microvibrations and temperature fluctuations, noise was introduced into the system and affected the quality of the signal measured.

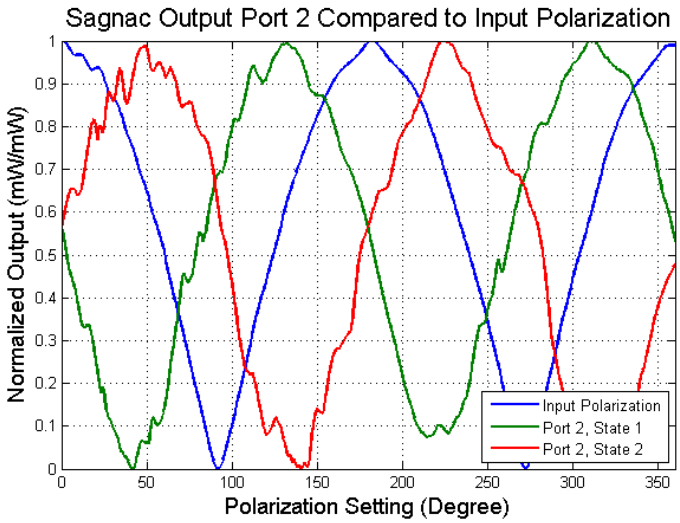

Figure 7.6: Normalized Sagnac output power showing shifting due to forward (green) and reverse (red) applied field compared to the input signal (blue)

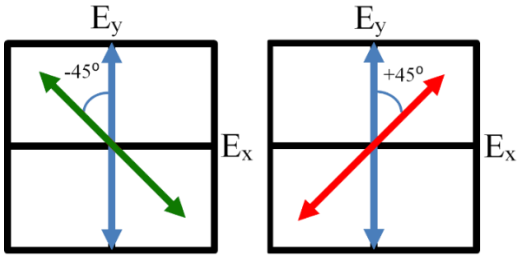

Figure 7.7: SoP rotation of the input signal (blue) as a result of Bi:YIG magnetization state 1 (left, green) and state 2 (right, red)

7.3 Conclusion

In this chapter, a novel fiber-based MO latching circuit has been presented. A brief discussion of the utilized bismuth-substituted rare earth iron garnet and its magnetic properties are included. Measurements show that between latched and unlatched states, the SoP of incident light can be rotated 90° (+45° to –45°) using this material. The latched optical router was successfully realized, with an insertion loss of 15.6 dB. The realization of this optical circuit enables the capability for low-power alternatives to conventional all-optical routers in current networking systems.

CHAPTER 8

TOWARD AN ON-CHIP MO MODULATOR

Monolithically integrating an MO modulator may be one of the most pressing endeavors as a result of demonstrating the fiber-based, proof-of-concept equivalents shown in Chapter 3 – Chapter 7. This chapter focuses on addressing the questions, challenges, and concerns that arise from this endeavor focusing on the optics, electronics, and magnetic field generation requirements.

The demonstrated routers and switches use fiber-optic path lengths that are on the order of meters long. This is clearly too great for a large-scale deployable solution, so integrated solutions are desirable. One of the most popular platforms for integrated optical devices is the silicon-on-insulator (SOI) platform [46] [47] [48] [49] [50] [51] [52] [53] [54]. Waveguides are designed such that a sufficient beam profile is maintained throughout, with as little loss as possible. This has been well researched and is beginning to enter networking systems today. However, including MO materials exhibiting high Faraday rotations has been a topic of great interest recently.

Currently one of the most difficult tasks in constructing an MO device is the inclusion of the MO material. In passive, in-line MO devices for fiber-optic systems, manual insertion of the material and a field generator (usually a permanent magnet) has been the easiest and most common method. However, with the integration of optical systems on silicon-based technologies, monolithic integration of the entire device is anticipated. Many fabrication techniques have been employed, often including YIG ($Y_3Fe_5O_{12}$) as a seedlayer for Bi:YIG and Ce:YIG top layers. The tail of a Gaussian beam in the waveguide travels through the top MO material layer and experiences enough Faraday rotation to cause interference at the output [55] [56].

One important aspect to creating dynamic on-chip MO modulators is the magnetic field generation techniques. At such a small scale, suitable field generators (e.g. coils) have not been easy to monolithically integrate since 3D chip design

techniques need to be employed. Many 3D solenoids have been implemented for RF circuits and magnetic recording read-heads [57] [58], however none have been implemented for the purpose of causing the MO Faraday effect on light in a silicon waveguide.

In this chapter, the design and simulation of an on-chip optical waveguide and magnetic field generator are presented. The simulations were performed in COMSOL 4.2. Additionally, design tools are provided for the creation of a codirectional coupler, another important device in this system. The main items to be discussed are the importance of using silicon as the transmission medium, the silicon-on-insulator (SOI) platform, optical waveguide design and simulation, coupler design tools, and magnetic field generator design and simulation.

8.1 Silicon on Insulator Platform

Silicon, although absorptive at visible wavelengths, is transparent to infrared light. Moreover, it is clearly well-suited for integration with electronic devices. However, in order to build a silicon waveguide, a low-index cladding material must be positioned between the waveguide and the substrate in order to prevent the optical mode from leaking out. In the silicon-on-insulator (SOI) platform, a buried oxide insulator on a silicon substrate functions in this capacity (Figure 8.1) [59] – [60].

This buried oxide is grown by either a bond-and-etchback technique [61] or augmenting the silicon layer thickness by epitaxy after an oxygen implant [62]. Although the high index contrast between silicon and oxide/air seems to imply a small mode size, relatively large optical modes can be confined in silicon rib waveguides without sacrificing single-mode operation [63]. Single-mode waveguides with propagation loss as low as 0.1 dB/cm have been achieved using this method [64]. Due to the success of this technology and waveguide design, the rib waveguide on SOI substrate will be used in this work.

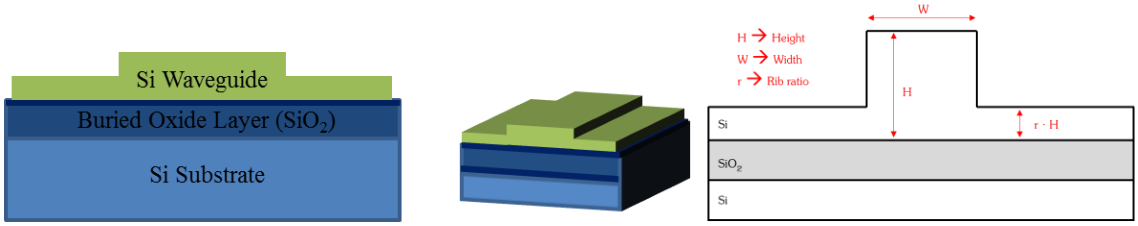

Figure 8.1: Rib waveguide using SOI technology

8.2 Optical Waveguide Design and Simulation

According to [64], single-mode rib waveguides can have geometry restrictions described by the following,

$$r \leq 0.5$$

$$\frac{W}{H} \leq 0.3 + \frac{r}{\sqrt{1-r^2}} \qquad (8.1)$$

where W is the width of the waveguide, H is the distance from the top of the waveguide to the buried oxide layer, and r is the desired ratio that leads to the height of the top silicon layer (Figure 8.1). In this work, the waveguide geometry will be similar to that presented in [64], and optical mode simulation results paired with waveguide propagation simulations will be presented.

The optical waveguide simulations are performed in COMSOL 4.2. The height of the waveguide is 1.0 µm, the width is 1.0 µm, and the rib ratio is 0.28. As shown in Figure 8.2, the optical mode is well confined in the Si waveguide, with air surrounding its sides and top and SiO_2 (the buried oxide layer) on the bottom. The simulation was performed with a wavelength of 1550 nm, and the solution shown is for an effective mode index of approximately 3.35.

Although this is a good indication that the waveguide geometry is sufficient for designing an interferometer, it would be advantageous to observe confinement of the propagating wave in the longitudinal direction. Thus, a frequency analysis of the waveguide from a top view was performed (Figure 8.3). In this simulation, an excitation

field of 1 V/m in the z-direction (out of page) was applied at a wavelength of 1550 nm propagating in the y-direction (left to right of page).

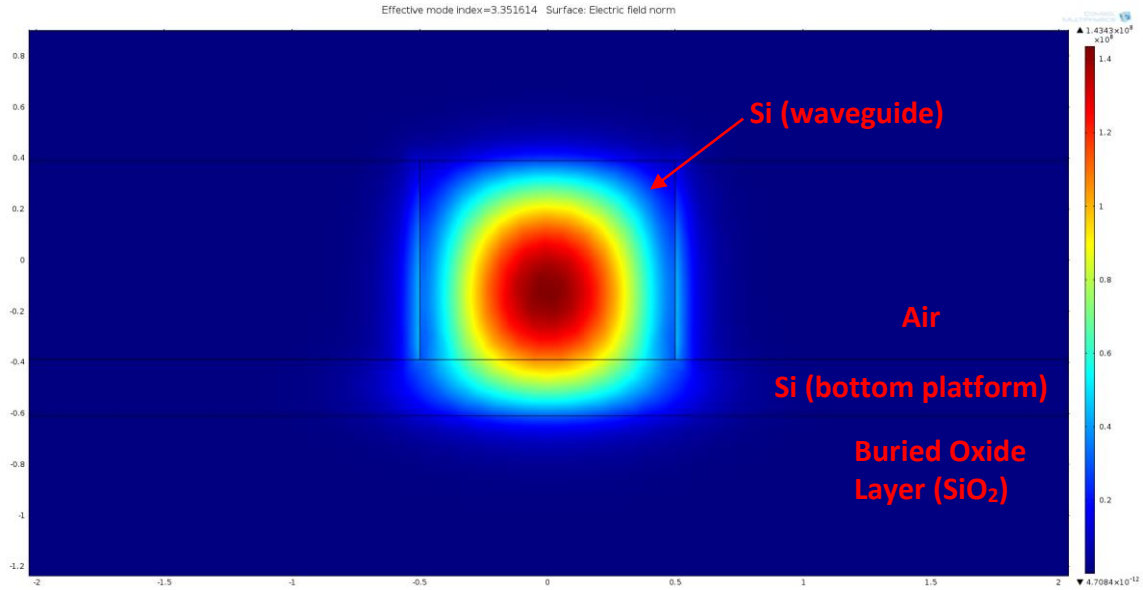

Figure 8.2: Optical mode simulation for SOI rib-waveguide

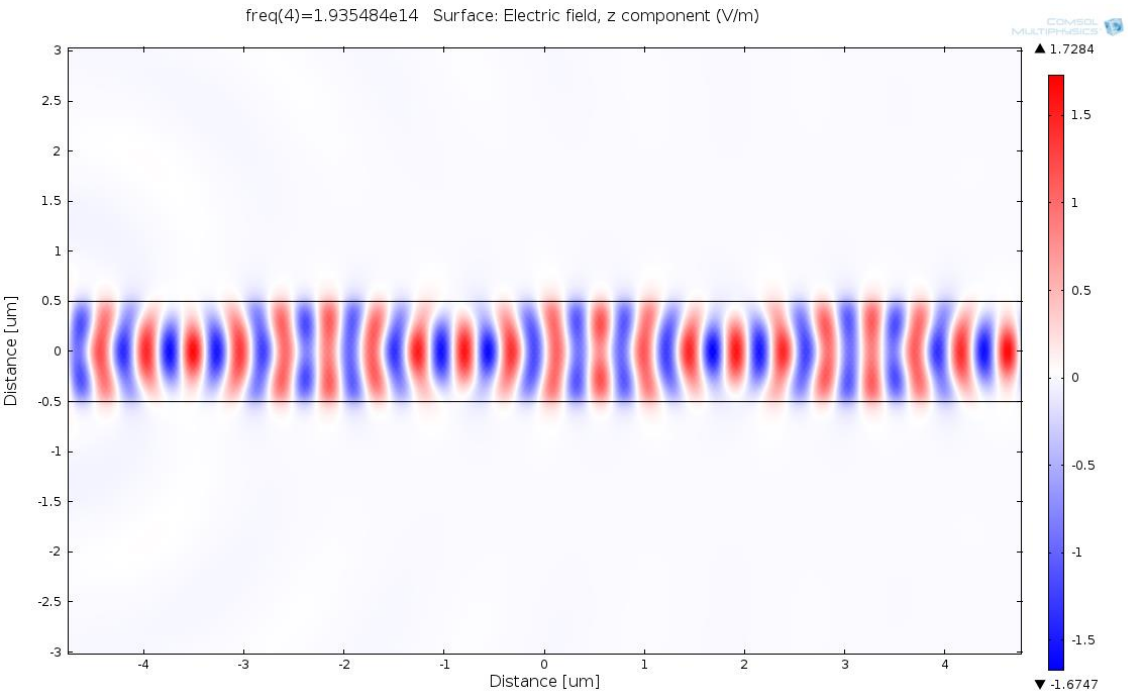

Figure 8.3: Top view of waveguide showing wave propagation at 1550nm

8.3 Codirectional Coupler Design

An optical device used often in the interferometer designs is the codirectional coupler. This can have varying power coupling coefficients, κ, depending on the distance between coupled waveguides and the length of the coupling section, x (Figure 8.4).

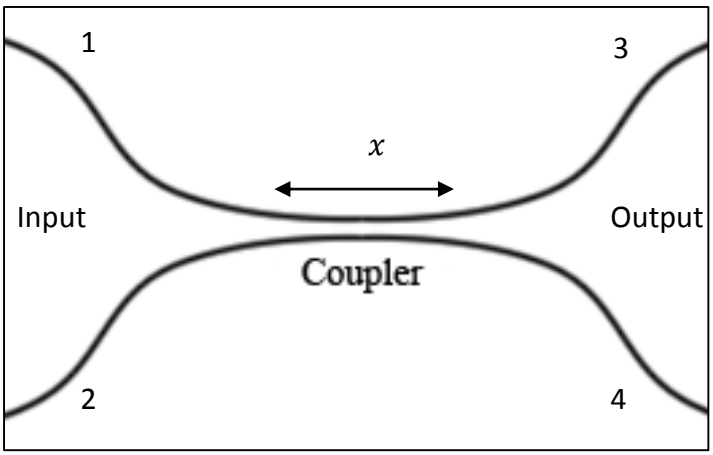

Figure 8.4: Schematic representation of a codirectional coupler

Neglecting losses, the input-output characteristics can be described by the following equation [65]:

$$\begin{bmatrix} \vec{E}_{3o} \\ \vec{E}_{4o} \end{bmatrix} = \begin{bmatrix} \sqrt{1-\kappa} & j\sqrt{\kappa} \\ j\sqrt{\kappa} & \sqrt{1-\kappa} \end{bmatrix} \begin{bmatrix} \vec{E}_{1i} \\ \vec{E}_{2i} \end{bmatrix} \quad (8.2)$$

Assuming no input at port 2 and $= \frac{1}{2}$, one will find that the equation can be reduced to that provided in the interferometer calculations of Section 2.4. However, the coupling coefficient is a function of L_c, the length of a coupler of which a signal from port 1 completely couples to port 4. Assuming a transmission coefficient of T (and $E_{2i} = 0$), the output as a function of coupler length (L_c) is [66]:

$$\vec{E}_{3o}(x) = T\vec{E}_{1i} \cos\left(\frac{\pi}{2L_c}x\right) \quad (8.3)$$

$$\vec{E}_{4o}(x) = jT\vec{E}_{1i} \sin\left(\frac{\pi}{2L_c}x\right) \quad (8.4)$$

After a length of L_c, the input at port 1 will have coupled completely to the output port 4, given that both waveguides have the same propagation constant. The value L_c can be modified by varying the coupling gap. A specific coupler length, x, can then be chosen to achieve the desired power coupler coefficient. For example, a codirectional coupler with $L_c = 450\ \mu m$ will have a power coupling coefficient of 0.7 given a specific coupler length of 284 µm (the output intensities are normalized, according to [65]).

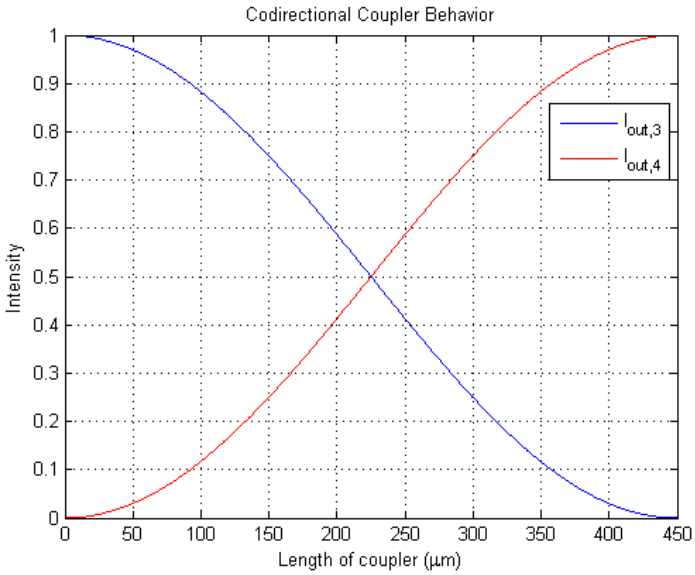

Figure 8.5: Example of a codirectional coupler with L_c = 450 µm

8.4 Simulation of Optical Waveguide with MO Material

The waveguide and coupler designs described in Section 8.2 and Section 8.3 are well suited for single mode confinement of light at 1550 nm. In this section, the effect of adding a top layer of magneto-optic (MO) material to an SOI rib waveguide will be analyzed. In particular, the mode profile will be simulated to determine the amount of light that is exposed to Faraday rotation. This will aide in understanding the level at which light with rotated state of polarization will interfere with non-rotated light.

An SOI rib waveguide with height of 1 µm is designed with a 0.2 µm top layer of MO material. Mode analyses show the portion of the input field that traverses through

the top layer and the solution has an effective mode index of approximately 3.36 (Figure 8.6). This particular magneto-optic material was chosen for its low-moment capability, and has an index of refraction of 2.344 [20]. Additionally, 3D height information provides an alternative perspective on the portion of light in the MO material relative to the total (Figure 8.7).

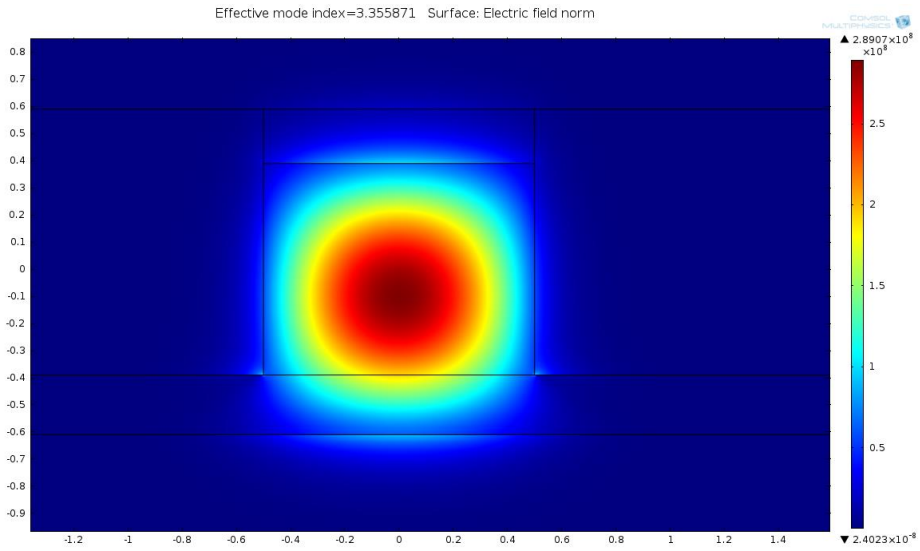

Figure 8.6: SOI waveguide mode analysis with 0.2 um top layer of MO material (n = 2.344)

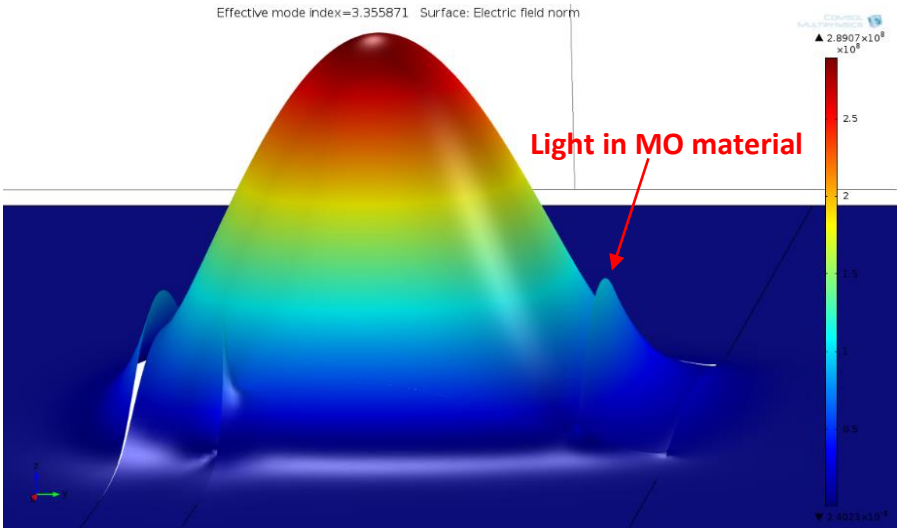

Figure 8.7: SOI waveguide mode analysis with 3D height information

Analyzing a line cut down the center of the 2D waveguide clearly shows the effect of the boundary materials (Figure 8.8). However, further analysis is required to determine approximately how much of the light is present in MO material.

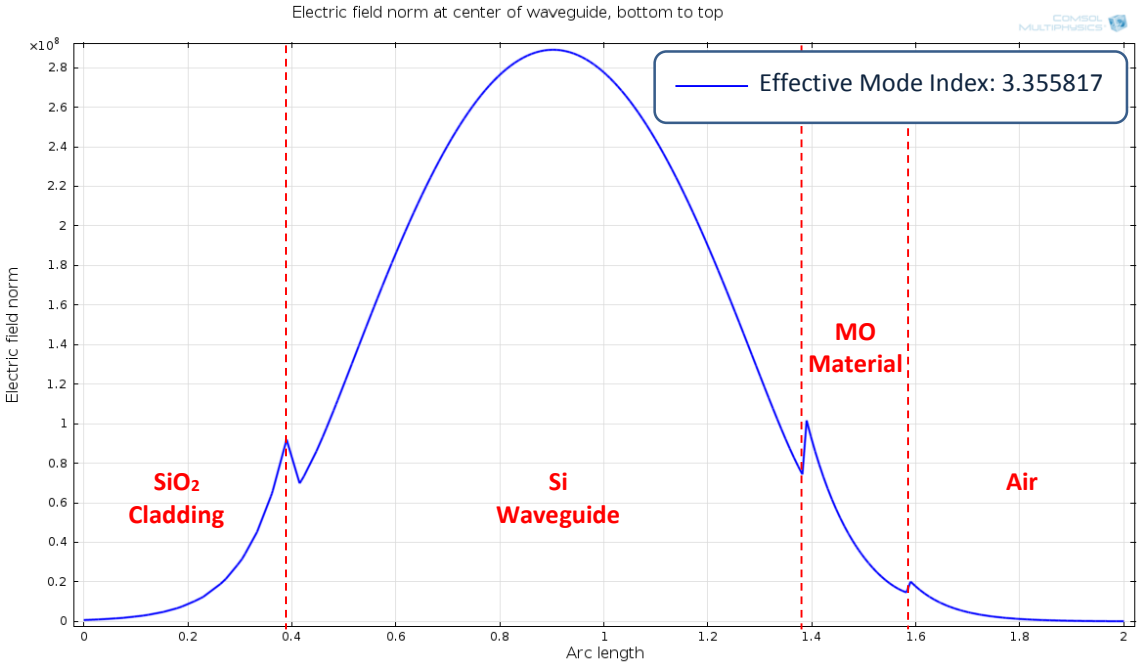

Figure 8.8: SOI waveguide mode analysis, center cut

Line cuts at different positions along the face of the waveguide were then analyzed in MATLAB. Data was first exported from COMSOL, consisting of varying y-position data with fixed x-positions (Figure 8.9). The resulting traces from each cut were then analyzed to find the approximate percentage of the field in the MO material (Figure 8.10). This was calculated by first numerically integrating each cut, then numerically integrating between the bounds defined by the MO material. The ratio of the portion in the MO material to the total field in each cut was then calculated. The average of the percentages from each cut was then calculated, resulting in the final reported percentage. It was found that approximately 3.9% of the light resides in the MO material using this method. According to [14], although this as a small percentage

there is sufficient Faraday rotation to see interference at the optical output. However, this would only occur if the material is magnetized using either a permanent magnet or, more desirably, a controlled magnetic field generator.

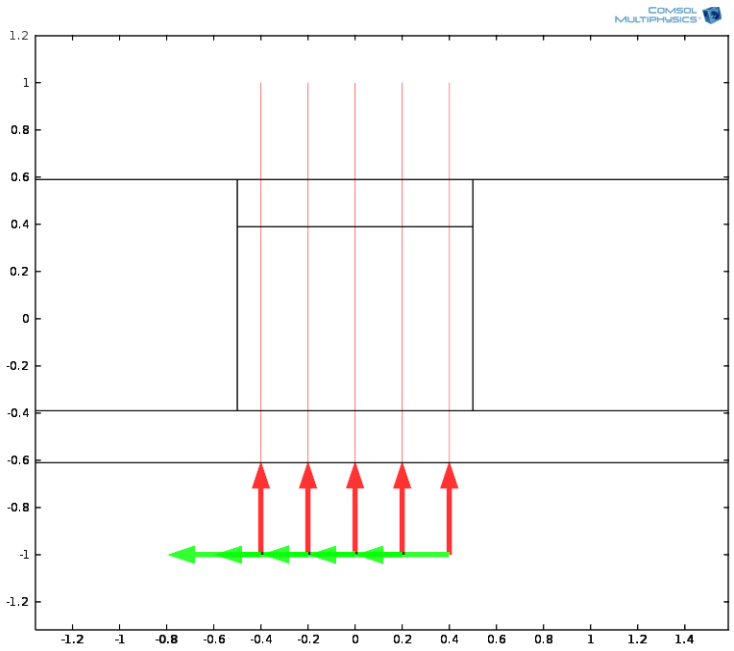

Figure 8.9: Line cuts from 2D waveguide simulation

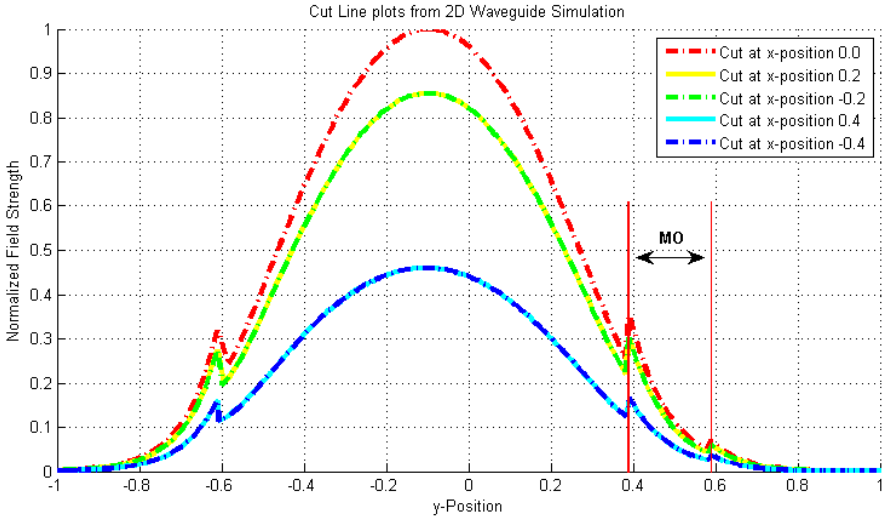

Figure 8.10: Normalized field strengths along 2D line cuts

8.5 Design and Simulation of Integrated Transverse-Plane Solenoid

Much effort has been put into discovering new methods and techniques that deposit the MO material without extensive damage to the silicon waveguide [67] [33]. However, little research has been performed on a monolithically-integrated dynamic magnetic field generator for such devices. This section discusses a novel field generator for on-chip optical waveguides.

In fiber-based field generation systems it is conventional to pass current through a solenoid, creating a magnetic field that sufficiently magnetizes magneto-optic material at the solenoid's center. Light passing through an energized solenoid with MO material experiences Faraday rotation, a phenomena that can be utilized in interferometry to create all-optical switches and routers (see Section 2.3.2) [68]. On silicon-based devices, solenoids are more often seen as compact inductors for RF applications (e.g. [69] [70] [71] [72] [73]), but rarely as magnetic field generators. Therefore, in this section a novel dynamic magnetic field generator for monolithically integrated MO devices on silicon is proposed and magnetic field simulation is performed in COMSOL to validate its utility.

8.5.1 Experimental Results with Air Core

The chosen geometry of the coil follows the geometry of the optical waveguide presented in Section 8.2 (Figure 8.11). Specifically, an optical waveguide of 1 μm in width and 1 μm in height was used, with a rib ratio of 0.28. The coil, in this case, is surrounded by air ($\mu_r = 1$). It was found in simulation that providing 35mA of current to energize the novel 4-turn field generator resulted in 256 G generated near the optical waveguide's center (Figure 8.12). Additionally, the field strength near the top edge of the coil, where the MO layer would likely be present, peaks at approximately 200 G (Figure 8.13) This field strength is high enough to sufficiently magnetize Ce:YIG film on silicon with the given waveguide dimensions [14].

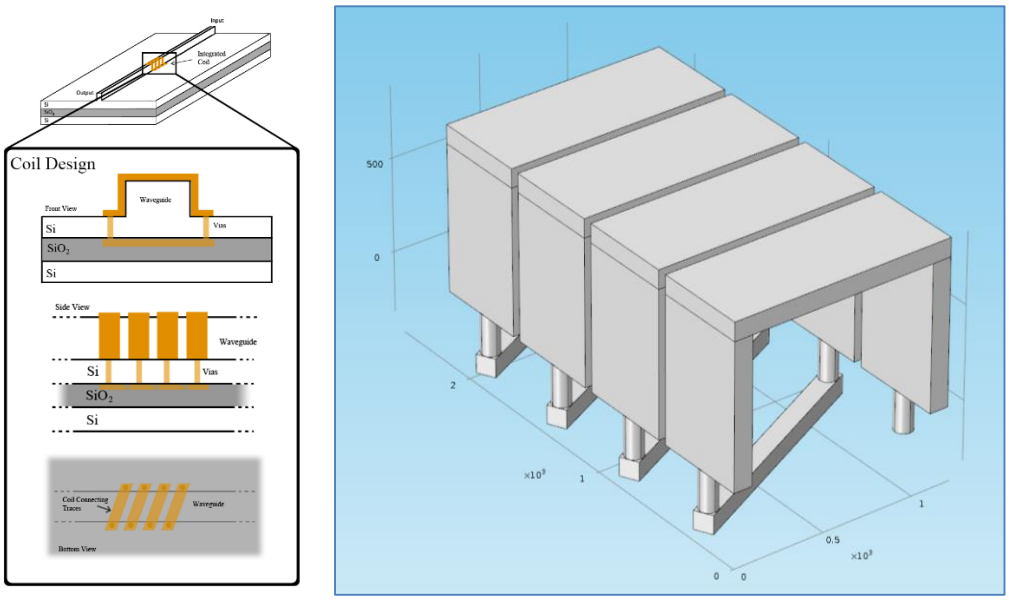

Figure 8.11: Integrated magnetic field generator concept and COMSOL geometry

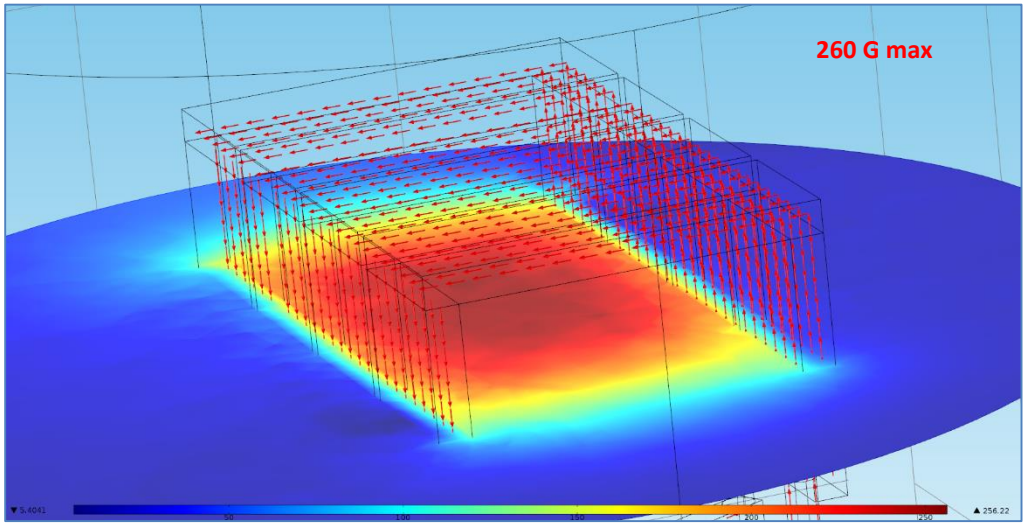

Figure 8.12: Integrated MFG with COMSOL simulation results at center of coil

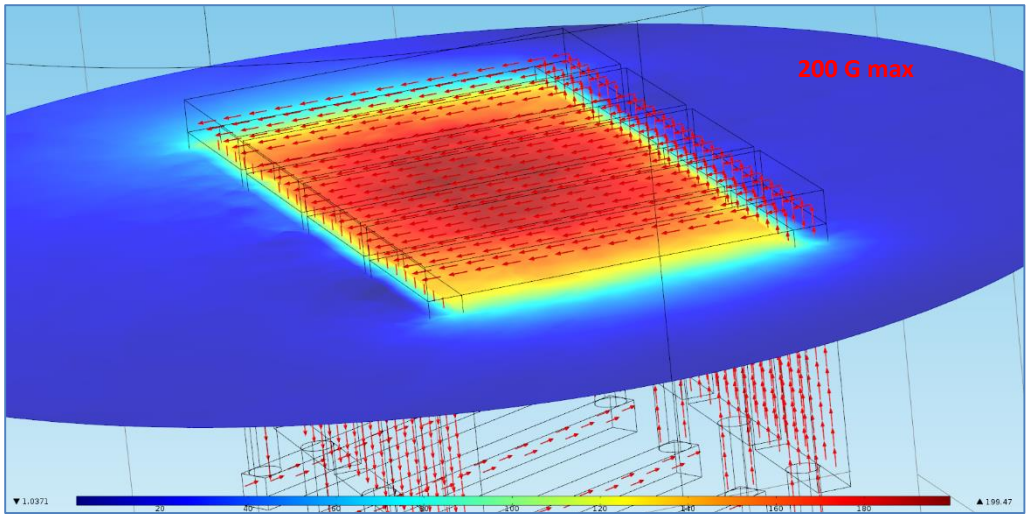

Figure 8.13: Integrated MFG with COMSOL simulation results near top edge of coil

8.5.2 Experimental Results with Si and MO core

It would be useful to know the field at the same points in space including the silicon and MO material at the core of the coil. Thus, the core was defined to have a layer of MO material 0.2 µm thick on top of the core, while a 0.8 µm thick silicon layer defined below that (Figure 8.14). The MO material in this simulation has $\mu_r = \varepsilon_r = 1$ and electrical conductivity equal to zero ($\sigma = 0$), for convenience. The silicon waveguide also has relative permeability set to 0 and permittivity set to 1, however the conductivity is defined to be $\sigma = 1.56e^{-3}$.

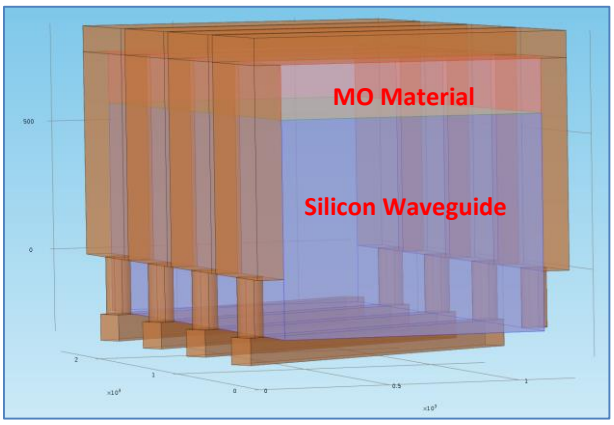

Figure 8.14: Integrated MFG with Si and MO core

Results show that the magnetic field generated at the center of the coil and within the MO material has a maximum field of approximately 210 G (Figure 8.15), given a current of 35 mA. Additionally, the field generated in the silicon waveguide with the same current has a peak near 270 G (Figure 8.16).

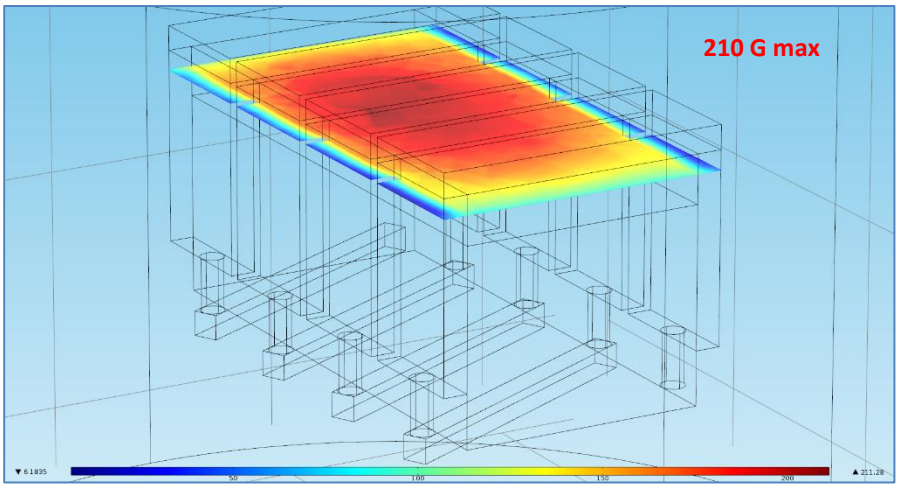

Figure 8.15: Field generated in the MO material

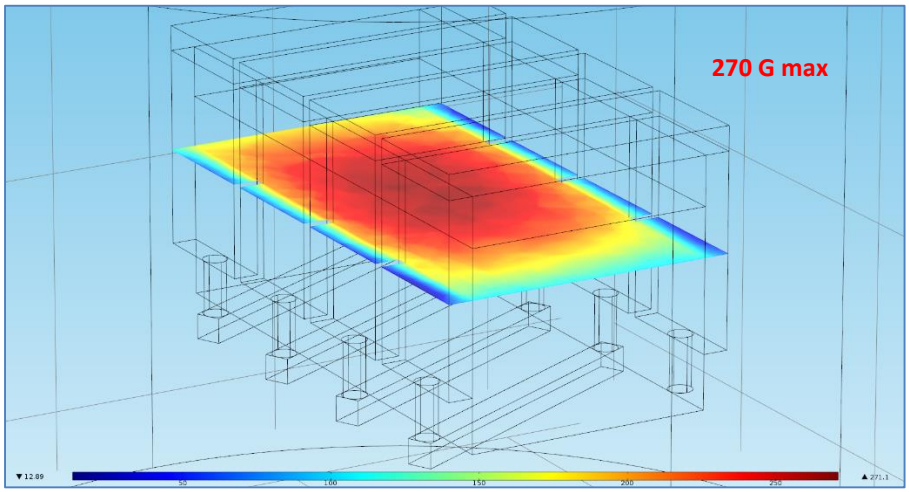

Figure 8.16: Field generated in the silicon waveguide

8.6 Conclusion

The results presented in this chapter are preliminary results since the properties of useful, consistently manufacturable MO material have yet to be well-developed. Much research is being conducted to determine what is the best deposition method of the MO material on silicon [55] [56], and once the resulting material properties are reported the model can be improved.

However, these simulations and design methodologies provide a proof of concept on-chip magnetic field generator for silicon rib waveguides. This is a highly anticipated effort if dynamic all-optical modulators utilizing MO materials are to be realized. The reported currents in the fiber-based experiments throughout this work peak on the order of 10 A, while the currents in these simulations are on the order of 30 mA. This is a clear reduction in quiescent power and offers an entirely new class of magneto-optic devices.

Future work will include simulation of the optical properties of the waveguides and overall devices which is comprised of insertion loss, reflection, birefringence, cross-talk, extinction ratio, polarization-dependent loss, wavelength dependency, and several others. Additionally, the simulation tools (e.g. COMSOL) have the capability of define permeability tensors, as opposed to scalars, for materials whose permeability is not isotropic. This allows for the simulation of Faraday rotation and will further enhance the study.

The results of this study show the potential for a great improvement over currently researched solutions for fiber-based systems [40] [37]. In addition, the implications of such a device with a dynamic magnetic field generator extend to applications in which optical isolation needs to be reversed using low power. This capability can widely diversify optical network design.

CHAPTER 9

MESSAGE TO FUTURE RESEARCHERS

As this work is expanded, I believe and hope that the multifaceted nature of the goals listed throughout this dissertation will create new directions requiring new capabilities, relationships, and exciting distributions of knowledge and information. Continuing this work, to me, does not necessarily mean to follow the next steps in line for this technology, although that can be an advantage. Instead, it is more important that we can firstly excite those around us who relate to our technology and who have capabilities beyond our own. Jim Collins, an author of the best seller "Good to Great," once said, "great vision without great people is irrelevant." In the advancement of this work, the greatest advantage one can have is the relationships and collaborations with others to help in this endeavor. However, there are some immediate steps that can be taken to prepare.

In Chapter 8 of this dissertation, the design and simulation of on-chip optical waveguides are presented. The on-chip interferometer simulations in full are not presented since the simulation tools are not currently capable of performing the full system tasks. In order to have a stronger foundation, to take this work beyond its current form, the simulations must be matched with tests of real devices or more advanced tools must be acquired to have confidence in the final works. This requires new relationships with those who have access to the necessary fabrication and measurement equipment. However, a few other efforts need to be sustained:

1. Microwave circuit design, test, and analysis
2. Fiber-based interferometer design and testing
3. Rapid prototyping of electronics
4. Continued improvement of magnetic materials

9.1 Microwave Design, Test, and Analysis

In this and the majority of previous works at the High Speed Systems Lab at Iowa State University, electronic circuitry has been required in the optical systems research. This circuitry is a fundamental component that enables the advancement of the related optical networking systems developed at this lab, and in the majority (if not all) of the deployed technologies. Therefore, it is sensible that the design, test, and analysis of such circuitry is a bare minimum requirement to continue this work.

9.2 Fiber-Based Interferometer Design and Testing

Although one of the main goals to advance this work is to bring the fiber-based systems onto integrated circuit platforms, the fiber-based platform is fastest way to test new ideas in the optical domain. The ease of connecting or removing fiber patch cables to active and passive optical devices makes the fiber-based systems ideal for providing convincing proof of concepts. Additionally, the size of the fiber system is convenient to interface rapidly prototyped electronics when necessary.

9.3 Rapid Prototyping of Electronics

Since microwave circuit design, test, and analysis is considered a fundamental component of this work, it would be advantageous to very quickly fabricate such circuits to reduce the time to implementation of the fiber systems. Relieving the challenges of generating the circuit materials can allow one to focus more acutely on the challenges in the optical domain.

In this context, rapid prototyping of electronics refers to using schematic and layout software to design circuits, then using an in-house mill or fabrication company to create the printed circuit board (PCB), and finally to manually populate the PCB using parts from a separate purchase. This is not new, nor uncommon, however it can sometimes be a task full of trade secrets and assumed knowledge.

9.4 Conclusion

Some of the most important items in this work are in the expansion of the toolset for all-optical switch and router designers and the path to research in monolithically integrated all-optical technologies. This is a great effort that requires relatively large amounts of resources and teamwork. However, this path can lead to many other research venues including on-chip sensors, detectors, and measurement systems. The potential is limitless, and I hope that this work provides points of inspiration to further pursue studies in high speed circuits, light, magnetic materials, and electromagnetism.

CHAPTER 10
CONTRIBUTIONS

This chapter discusses the specific contributing works that this dissertation revealed in order to advance research in magneto-optic, all-optical interferometric switching and routing. The five contributions include the following core topics related to the development of all-optical MO switches and routers:

1. Reduced power operation of magnetic field generation (Chapter 4)
2. Enhanced magneto-optic pulsing (Chapter 5)
3. Enhanced interferometer sensitivity (Chapter 6)
4. Differentiation of MO routing topology (Chapter 7)
5. Expansion of on-chip MO modulator studies and simulations (Chapter 8)

Each contribution resulted in publications in the IEEE Transactions on Magnetics, IEEE Magnetics Letters, Journal of Applied Physics, and Magnetics Technology International Magazine.

10.1 Reduced Power Operation

In Chapter 4, a magnetic field generation method is presented that offers the potential for lower power operation of magneto-optic switching or routing. The discussed method utilizes a novel two-coil configuration to quickly magnetize the MO material and then sustain this field at a reduced current. One coil is of low number of turns (which provides low inductance and fast pulsing) and the other coil is of many turns (which provides equivalent field strength with less current). Optical and electrical results are provided utilizing the Sagnac interferometer for stability reasons. This work was published in 2012 in the Journal of Applied Physics entitled, “Low power field generation for magneto-optic fiber-based interferometric switches” [37].

10.2 Enhanced Switching Speed

The challenges in enhancing the switching speed of MO switches and routers are centered at the proper manipulation of the MO material. Since the activation of the material requires the application of an external magnetic field, this driving mechanism, e.g. magnetic field generation circuitry, is of great interest. In Chapter 5, the magnetic field generation circuitry is modified to provide a very fast pulsed magnetic field at the center of two concentric coils of equal turns. One coil magnetizes the material and the other coil is used to neutralize any residual field due to parasitics of the field generation circuitry. The result is a much shorter optical pulse which can lead to faster all-optical switching speeds. The presence of the reverse field to neutralize the residual field reduced the optical pulse width from 739 ns to 129 ns. Optical and electrical results are provided utilizing the Sagnac interferometer, again for stability reasons. This work was published in 2013 in the IEEE Transactions on Magnetics entitled, “Improved Switching for Magneto-Optic Fiber-Based Technologies” [15].

10.3 Enhanced Interferometer Sensitivity

MO interferometer sensitivity can be defined, in this context, as the degree to which applied field strength causes a change in optical output. An interferometer of high sensitivity, then, is one in which the optical output changes drastically with very little change in applied magnetic field strength. In Chapter 6, the resonator interferometer configuration was demonstrated with MO material to create an all-optical switch. The combination of using this interferometer configuration with a low-moment MO material offers much greater switching sensitivity than competitive interferometers (e.g. Mach-Zehnder and Sagnac). This leads to lower power operation and a more simplistic design since less field (and thus less current) is required to achieve all-optical switching. Optical output pulses of 152 ns were achieved and

presented in this work. This work was published in 2013 in the IEEE Magnetics Letters entitled, “Magneto-Optic Interferometric Switch With Resonator Configuration” [30].

10.4 Differentiation of MO Routing Topology

The improvement of all-optical networking architectures relies on the different tools that can be taken advantage of. Continuing to develop, improve, and create new tools is essential in the expansion of optical communications technology. In Chapter 7, a new type of MO router is demonstrated that employs a latching magneto-optic material. This new device is shown to be useful in differentiating the capabilities of non-reciprocal MO devices, expanding the toolset of all-optical network designers. This work was published in 2014 in the IEEE Transactions on Magnetics entitled, “Demonstration of magneto-optic latching router for all-optical networking applications” [74].

10.5 On-Chip MO Modulator Studies and Simulations

The optical experiments performed in this work are done so using a fiber-based system. This system is useful in rapidly prototyping proof-of-concept devices that have implications at much smaller scales. However, to advance this technology further it is necessary to bring this platform to the chip scale. Integrated photonic platforms of great interest recently, especially in the field of magneto-optic technologies since their nonreciprocal effects allow for all-optical isolation, switching, and routing with the potential for low power operation. The preliminary studies and simulations in Chapter 8 are the essential activities required to create on-chip MO modulators. The goal of this chapter is to provide preliminary results that will hopefully lead to future level-of-effort investigations for on-chip solutions. Many of the ideas presented in this chapter have been published as invited papers in 2012, 2013, and 2014 in Magnetics Technology International Magazine with titles, “Magneto-Optic Switching in Fiber-Optic Systems” [75], “Feel the Pulse” [26], and “Communicating with Magnetism” [76].

BIBLIOGRAPHY

[1] P. Horowitz and W. Hill, "The Art of electronics," 1989.

[2] R. Schmitt, Electromagnetics Explained: A handbook for wireless/RF,EMC, and high speed electronics, New York: Newnes, 2002.

[3] R. J. Weber, Introduction to microwave circuits radio frequency and design applications, New York: IEEE press, 2001.

[4] E. T. Whitteker, A History of theories of aether and electricity, Dublin: Hodges, Figgss, and Co. Ltd, 1910.

[5] A. Einstein, "Zur Elektrodynamik bewegter Körper," *Annalen der Physik,* p. 17 (10): 891–921, 1905.

[6] Y.-S. Yeh, M. G. Hluchyj and A. Acampora, "The Knockout Switch: A Simple, Modular Architecture for High-Performance Packet Switching," *IEEE Journal on Selected Areas in Communications,* pp. Vol. 5, No. 8, pp. 1274-1283, 1987.

[7] X. Ma and G.-S. Kuo, "Optical switching technology comparison: optical MEMS vs. other technologies," *IEEE Communications Magazine,* vol. 41, no. 11, pp. S16-S23, 2003.

[8] S. O. Kasap, Optoelectronics and Photonics: Principles and Practices, Upper Saddle River, NJ: Prentice Hall, 2001.

[9] S. Kemmet, M. Mina and R. J. Weber, "Fiber-Based Magneto-Optic Sagnac Optical Modulator," *IEEE Transactions on Magnetics,* vol. 45, no. 10, pp. 4892-4894, 2009.

[10] R. Bahuguna, M. Mina and R. J. Weber, "Mach-Zehnder Interferometric Switch Utilizing Faraday Rotation," *IEEE Transactions on Magnetics,* vol. 43, no. 6, pp. 2680-2682, 2007.

[11] P. Hariharan, Optical Interferometry, Amsterdam: Academic, 2003.

[12] C. K. Madsen and J. H. Zhao, Optical Filter Design and Analysis: A Signal Processing Approach, New York: John Wiley, 1999.

[13] J. A. Stratton, Electromagnetic Theory, New York: McGraw-Hill, 1941.

[14] L. Bi, J. Hu, P. Jiang, D. H. Kim, G. F. Dionne, L. C. Kimerling and C. A. Ross, "On-chip optical isolation in monolithically integrated non-reciprocal optical resonators," *Nature,* vol. 5, pp. 758-762, 2012.

[15] J. W. Pritchard, M. Mina and R. J. Weber, "Improved Switching for Magneto-Optic Fiber-Based Technologies," *IEEE Transactions on Magnetics,* vol. 48, no. 11, pp. 3772-3775, 2012.

[16] L.-S. Yan, A. E. Willner, X. Wu, A. L. Yi, A. Bogoni, Z.-Y. Chen and H.-Y. Jiang, "All-Optical Signal Processing for Ultra-High Speed Optical Systems and Networks," *Journal of Lightwave Technology,* vol. 30, no. 24, pp. 3760-3770, 2011.

[17] "Multiple Radio Shows," [Online]. Available: http://musiciam.co.uk/multipleradioshows/images/light-interference.jpg.

[18] "Wave Optics Simulation Software - Simulating Optical Design Components," COMSOL Multiphysics, 2014. [Online]. Available: http://www.comsol.com/wave-optics-module.

[19] "Manual Variable Optical Delay Line VDL - General Photonics Corporation," General Photonics Corporation, 2011. [Online]. Available: http://www.generalphotonics.com/ProductDetail.aspx?dept=10&cp=67&d=1.

[20] Integrated Photonics, "Integrated Photonics, Inc.," April 2008. [Online]. Available: http://integratedphotonics.com/images/Product_Bulletin_FLM_F1-5.pdf.

[21] M. S. Sodha and N. C. Srivastava, Microwave Propagation in Ferrimagnetics, New York: Plenum Press, 1981.

[22] D. C. Jiles, Introduction to Magnetism and Magnetic Materials, London: Chapman and Hall, 1998.

[23] V. J. Fratello, S. J. Licht and C. D. Brandle, "Innovative improvements in bismuth-doped rare-earth iron garnet Faraday rotators," *IEEE Transactions on Magnetics,* vol. 32, no. 5, p. 6, 1996.

[24] V. J. Fratello, S. J. Licht and C. D. Brandle, "Compositional Design of Faraday Rotator Materials," *MRS Proceedings,* vol. 574, p. 225, 1999.

[25] S. Tkachuk, V. J. F., C. Kraft, G. Lang and I. D. Mayergoyz, "Imaging Capabilities of Bismuth Iron Garnet Films With Low Growth-Induced Uniaxial Anisotropy," *IEEE Transactions on Magnetics,* vol. 45, no. 10, pp. 4238-4241, 2009.

[26] J. W. Pritchard and M. Mina, "Feel the Pulse," *Magnetics Technology International,* 2013.

[27] D. K. Mynbaev and L. L. Scheiner, Fiber-optic Communications Technology, Upper Saddle River, NJ: Prentice Hall, 2001.

[28] C. A. Balanis, Advanced Engineering Electromagnetics, Hoboken, NJ: John Wiley & Sons, Inc., 2012.

[29] R. C. Jones, "A New Calculus for the Treatment of Optical Systems," *Journal of the Optical Society of America,* vol. 31, no. 7, pp. 488-493, 1941.

[30] J. W. Pritchard and M. Mina, "Magneto-Optic Interferometric Switch With Resonator Configuration," *IEEE Magnetics Letters,* vol. 4, p. 6000104, 2013.

[31] J.-W. Tioh, M. Mina and R. J. Weber, "Field Coil for Magneto-Optic Switching: Capacitance Considerations," *IEEE Transactions on Magnetics,* vol. 44, no. 11, pp. 3843-3846, 2008.

[32] S. Kemmet, M. Mina and R. J. Weber, "Magnetic pulse generation for high-speed magneto-optic switching," *Journal of Applied Physics,* vol. 109, pp. 07E333-07E333-3, 2011.

[33] L. Bi, J. Hu, G. F. Dionne, L. Kimerling and C. A. Ross, "Monolithic integration of chalcogenide glass/iron garnet waveguides and resonators for on-chip nonreciprocal photonic devices," *SPIE Proceedings,* pp. 7941-794105, 2011.

[34] G. B. Scott and D. E. Lacklison, "Magnetooptic properties and applications of bismuth substituted iron garnets," *IEEE Transactions on Magnetics,* Vols. Mag-12, pp. 292-311, 1976.

[35] V. J. Fratello, S. E. G. Slusky, C. D. Brandle and M. P. Norelli, "Growth-induced anisotropy in bismuth: Rare-earth iron garnets," *Journal of Applied Physics,* vol. 60, no. 7, pp. 2488-2497, 1986.

[36] C. H. Tsang, R. M. White and R. L. White, "Transit-time measurements of domain-wall mobilities in YFeO," *Journal of Applied Physics,* vol. 49, no. 12, pp. 6052-6062, 1978.

[37] J. W. Pritchard, M. Mina and S. Kemmet, "Low power field generation for magneto-optic fiber-based interferometric switches," *Journal of Applied Physics,* vol. 111, pp. 07A941-07A943, 2012.

[38] Q. Xu, B. Schmidt, S. Pradhan and M. Lipson, "Micrometre-scale silicon electro-optic modulator," *Nature,* vol. 435, pp. 325-327, 2005.

[39] J.-W. Tioh, R. J. Weber and M. Mina, "Magneto-optical switches," in *Optical switches: Materials and design*, Philadelphia, PA, Woodhead Publishing, 2010.

[40] S. Kemmet (Oster), M. Mina and R. J. Weber, "Current-Controlled, High-Speed magneto-Optic Switching," *IEEE Transactions on Magnetics,* vol. 46, p. 2, 2010.

[41] S. Sundada and T. Harayama, "Sagnac effect in resonant microcavities," in *2006 International Conference on Transparent Optical Networks*, IEEE, 2006, p. 92.

[42] F. Xiaojun, "A variable-loop Sagnac interferometer for distributed impact sensing," *Journal of Lightwave Technology,* vol. 14, no. 10, pp. 2250-2254, 1996.

[43] T. S. Jang, S. S. Lee, I. B. Kwon, W. J. Lee and J. J. Lee, "Noncontact detection of ultrasonic waves using fiber optic Sagnac interferometer," *IEEE Transactions on Ultrasonics, Ferroelectrics, and Frequency Control,* vol. 49, no. 6, pp. 767-775, 2002.

[44] A. Yariv, "Universal relations for coupling of optical power between microresonators and dielectric waveguides," *Electronics Letters,* vol. 36, no. 4, pp. 321-322, 2000.

[45] Integrated Photonics Inc., "MGL Garnet-Latching Faraday Rotator," 2010. [Online].

[46] T. Aalto, M. Cherchi, M. Harjanne, M. Kapulainen and S. Ylinen, "Dense photonics integration on a micron-scale SOI waveguide platform," *IEEE 10th International Conference on Group IV Photonics,* pp. 107-108, 2013.

[47] A. Beling, M. Piels, A. S. Cross, Y. Fu, Q. Zhou, J. Peters, J. E. Bowers and J. C. Campbell, "High-power InP-based waveguide photodiodes and photodiode arrays heterogeneously integrated on SOI," *International Conference on Indium Phosphide and Related Materials,* pp. 171-172, 2012.

[48] N. Hattasan, B. Kuyken, J. Leo, E. M. P. Ryckeboer, D. Vermeulen and G. Roelkens, "High-Efficiency SOI Fiber-to-Chip Grating Couplers and Low-Loss Waveguides for the Short-Wave Infrared," *IEEE Photonics Technology Letters,* vol. 24, no. 17, pp. 1536-1538, 2012.

[49] S. Keyvaninia, G. Roelkens, D. Van Thourhout, J.-M. Fedeli, S. Messaoudene, G.-H. Duan, M. Lamponi, F. Lelarge, E. J. Geluk and B. Smalbrugge, "A highly efficient electrically pumped optical amplifier integrated on a SOI waveguide circuit," *IEEE 9th International Conference on Group IV Photonics,* pp. 222-224, 2012.

[50] S. Keyvaninia, S. Verstuyft, L. Van Landschoot, D. Van Thourhout, G. Roelkens, G.-H. Duan, F. Lelarge, J.-M. Fedeli, S. Messaoudene, T. de Vries, E. Geluk, B. Smalbrugge and M. Smit, "III-V/silicon first order distributed feedback lasers

integrated on SOI waveguide circuits," *39th European Conference and Exhibition on Optical Communication,* pp. 1-4, 2013.

[51] G. Kurczveil, J. R. Heck, J. M. Garcia, H. N. Poulsen, H. Park, J. P. Mack, D. J. Blumenthal and J. E. Bowers, "Integrated Recirculating Optical Hybrid Silicon Buffers," in *SPIE Proceedings 7606, Silicon Photonics V*, 2010.

[52] H. Nishi, T. Tsuchizawa, H. Shinojima, T. Watanabe, S. Itabashi, R. Kou, H. Fukuda and K. Yamada, "Low-Polarization-Dependent Silica Waveguide Monolithically Integrated on SOI Photonic Platform," *Journal of Lightwave Technology,* vol. 31, no. 11, pp. 1821-1827, 2013.

[53] A. Omari, W. Xie, P. Geiregat, D. Van Thourhout and Z. Henz, "Modeling the Optical Properties of Low-Cost Colloidal Quantum Dot Functionalized Strip SOI Waveguides," *IEEE Journal of Selected Topics in Quantum Electronics,* vol. 20, no. 4, pp. 71-76, 2014.

[54] Y. Xie, S. Gao and H. Sailing, "Two-channel simultaneous polarization demultiplexing and wavelength conversion for polarization-multiplexing signals in a SOI waveguide," *Asia Communications and Photonics Conferencev,* pp. 1-2, 2012.

[55] A. D. Block, P. Dulal and B. J. H. Stadler, "Growth Parameters of Fully Crystallized YIG, Bi:YIG, and Ce:YIG Films With High Faraday Rotations," *IEEE Journal of Photonics,* vol. 6, no. 1, pp. 1-8, 2014.

[56] T. Goto, Y. Eto, K. Kobayashi, Y. Haga, M. Inoue and C. A. Ross, "Vacuum annealed cerium-substituted yttrium iron garnet films on non-garnet substrates for

integrated optical circuits," *Journal of Applied Physics,* vol. 113, no. 17, pp. 17A939 - 17A939-3, 2013.

[57] K. Itoi, M. Sato, H. Abe, H. Ito, H. Sugawara, K. Okada, K. Masu and T. Ito, "On-chip high-Q solenoid inductors embedded in WL-CSP," *Proceeding of the Sixth IEEE CPMT Conference on High Density Microsystem Design and Packaging and Component Failure Analysis,* pp. 105-108, 2004.

[58] J. B. Albertini, H. Sibuet, P. Renaux and P. Gaud, "A new solenoid magnetic integrated head for digital video recording," *IEEE Transactions on Magnetics,* vol. 33, no. 5, pp. 2836-2838, 1997.

[59] M. Verbist, D. Van Thourhout and W. Bogaerts, "Low-contrast top gratings in high-contrast SOI waveguides for integrated holographic filters," *IEEE Photonics Conference,* pp. 200-201, 2012.

[60] L. Zimmermann, M. Kroh, K. Voigt, G. Winzer, H. Tian, L. Stampoulidis, B. Tillack and K. Petermann, "Hybrid integration of coherent receivers for Terabit Ethernet on SOI waveguide PLC," *IEEE 9th International Conference on Group IV Photonics,* pp. 153-155, 2012.

[61] B. N. Kurdi and D. G. Hall, "Optical Waveguides in Oxygen-Implanted Buried-Oxide Silicon-on-Insulator Structures," *Optical Letters,* vol. 13, no. 2, pp. 175-177, 1988.

[62] A. G. Rickman, G. T. Reed and F. Namavar, "Silicon-on-Insulator Optical Rib Waveguide Loss and Mode Characteristics," *Journal of Lightwave Technology,* vol. 12, no. 10, pp. 1771-1776, 1994.

[63] R. A. Soref, J. Schmidtchen and K. Peterman, "Large Single-Mode Rib Waveguides in GeSi-Si and Si-on-SiO2," *IEEE Journal of Quyantum Electronics,* vol. 12, no. 10, pp. 1971-1974, 1991.

[64] U. Fischer, T. Zinke, J.-R. Kropp, F. Arndt and K. Peterman, "0.1 dB/cm Waveguide Losses in Single-Mode SOI Rib Waveguides," *IEEE Photonics Letters,* vol. 8, no. 5, pp. 647-648, 1996.

[65] D. G. Rabus, Realization of optical filters using ring resonators with integrated semiconductor optical amplifiers in GaInAsP/InP, Berlin: Elektrotechnik und Informatik der Technischen Universität Berlin, 2002.

[66] K. J. Ebeling, Integrierte Optoelektronik, Berlin, Heidelberg, New York: Springer Verlag, 1992.

[67] T. Goto, M. C. Onbaşlı and C. A. Ross, "Magneto-optical properties of cerium substituted yttrium iron garnet films with reduced thermal budget for monolithic photonic integrated circuits," *Optics Express,* vol. 20, no. 27, pp. 28507-28517, 2012.

[68] R. Bahuguna, M. Mina, J.-W. Tioh and R. J. Weber, "Magneto-Optic-Based Fiber Switch for Optical Communications," *IEEE Transactions on Magnetics,* vol. 42, no. 10, pp. 3099-3101, 2006.

[69] M. Duplessis, O. Tesson, F. Neuilly, J. R. Tenailleau and P. Descamps, "Physical implementation of 3D integrated solenoids within silicon substrate for hybrid IC applications," *European Microwave Conference,* pp. 1006-1009, 2009.

[70] M.-H. Chang, K.-H. Lin, J.-W. Huang and A.-K. Chu, "On-chip solenoid inductors with high quality factor for high frequency magnetic integrated circuits," *IEEE Microwave and Wireless Components Letters,* vol. 16, no. 4, pp. 203-205, 2006.

[71] H. Namba, T. Hashimoto and M. Furumiya, "On-chip vertically coiled solenoid inductors and transformers for RF SoC using 90nm CMOS interconnect technology," *IEEE Radio Frequency Integrated Circuits Symposium (RFIC),* pp. 1-4, 2011.

[72] N. C. Schirmer, J. Hesselbarth, S. Strohle, B. R. Burg, M. K. Tiwari and D. Poulikakos, "Millimeter-wave on-chip solenoid inductor by on-demand three-dimensional printing of colloidal nanoparticles," *Applied Physics Letters,* vol. 97, no. 24, pp. 243109 - 243109-3, 2010.

[73] H.-Y. Tsui and J. Lau, "Experimental results and die area efficient self-shielded on-chip vertical solenoid inductors for multi-GHz CMOS RFIC," *IEEE Radio Frequency Integrated Circuits (RFIC) Symposium,* pp. 243-246, 2003.

[74] J. W. Pritchard, M. Mina and P. Dulal, "Demonstration of magneto-optic latching router for all-optical networking applications," *IEEE Transactions on Magnetics,* vol. 50, no. 11, p. 8001104, 2014.

[75] J. W. Pritchard and M. Mina, "Magneto-Optic Switching in Fiber-Optic Systems," *Magnetics Technologies International Magazine,* 2012.

[76] J. W. Pritchard and M. Mina, "Communicating with magnetism," *Magnetics Technology International,* pp. 68 - 71, 2014.

ACKNOWLEDGEMENTS

I would like to firstly acknowledge my major professor, advisor, and mentor, Professor Mani Mina. Your excitement, energy, patience, intellect, and ability to uniquely connect knowledge and information is absolutely inspiring. Having you believe in me was the best thing that could've happened during my undergraduate and graduate career. The eight years of having worked with you has transformed my thinking, learning, studying, researching, inventing, questioning, living, and my perspective on all things. I know that this new journey that lies ahead will not end our engagement and that my path of lifelong learning will always have the essence of your teachings. Thank you.

It is also a pleasure to acknowledge all those at Iowa State University who have supported my ideas, ambitions, and dreams. Dr. Robert Weber, our many meetings about advancing this research and your remarkable wisdom are an immeasurable addition to my work and growth. Dr. Sasha (Kemmet) Oster, thank you for your time, energy, positivity, and friendship. The discussions and collaborations of all things electromagnetic have shaped who I am as an engineer and researcher. Dr. Joe Idziorek, your constant push to inspire me to be the best that I could be has helped me from the beginning to the end of these studies. There are countless others, Dr. Ryan Gerdes, Dr. Jin-Wei Tioh, Dr. Tony Barsic, Narimdinda (Robert) Bouda, and many more, that I am very thankful of being able to work with and learn from.

I would finally like to acknowledge my family and friends for your collective support and encouragement. To my parents, John and Kathy Pritchard, thank you for everything and supporting all of my decisions. Danny, Anna, and Elizabeth, thank you for always listening and inspiring me to be great. To all of my extended family and my friends, this work would not be possible without your help. I am infinitely grateful.

APPENDIX A

IMPLEMENTATION OF MAGNETIC FIELD GENERATOR CIRCUITRY

The purpose of this chapter is to briefly present an application in which a magnetic field circuit is designed, simulated, fabricated, and finally implemented. This differs from the work presented in Chapter 3 – Chapter 7 as it provides implementation methods and in-house fabrication techniques. These efforts resulted in a collaboration with the Toyohashi University of Technology in Aichi, Toyohashi, Japan.

Abstract

In this brief report, magnetic field generation circuitry was designed, fabricated, and tested in an optical circuit. The results of this study show that approximately 23 A of current through a 20 turn, 5.3 mm long, 3.8 mm diameter coil generated well over 500 G. This was verified in an optical circuit which employed a bismuth-substituted yttrium iron garnet (Bi:YIG) with a coercivity of 500 G. This document presents the electronic design and fabrication process and also discusses the optical and electronic testing and results.

Electronic Circuit Design

The electronics design and simulation is performed in OrCAD 16.2. A suitable MOSFET was selected based on the current requirement generated by COMSOL simulation. The FET selected is the IRL3714ZSPBF by International Rectifier. This FET can provide 36 A of continuous current, or 100 A pulsed if the pulse width is less than 100 µs and sufficient thermal considerations are applied. The minimum electronic rise and fall time of 13ns and 5ns, respectively, are suitable for this desgn.

The Caddock MP725 current-sense resistor was chosen having a resistance of 0.05 Ω +/- 1%, and a power limit of 25 W.

This design was simulated in OrCAD 16.2, based on an accurate model found at the manufacturer's website. The resulting simulation proved the MOSFET would be a useful

candidate for magnetic field generation over 20 A predicted with a 5 V pulsed input (Figure A-1).

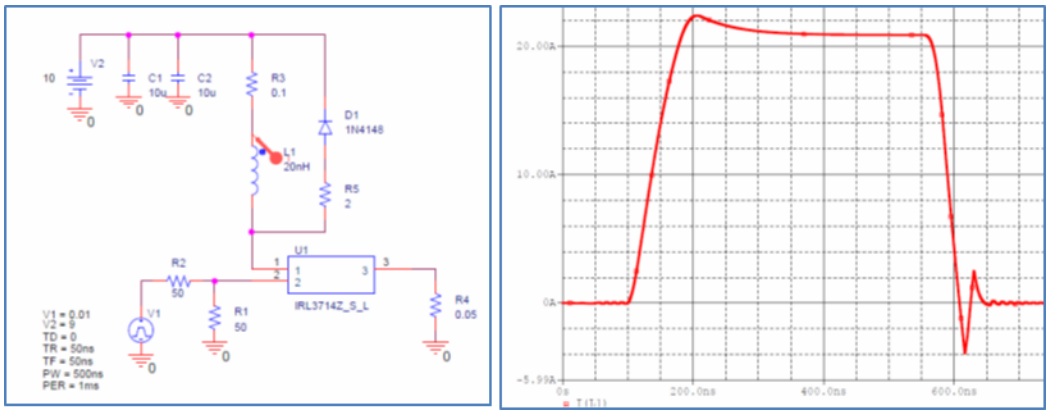

Figure A-1: Electronic circuit simulation in OrCAD 16.2

Electronics PCB Design and Fabrication

The circuit was then re-designed in Eagle PCB® (free version) to more easily perform PCB design (Figure A-2).

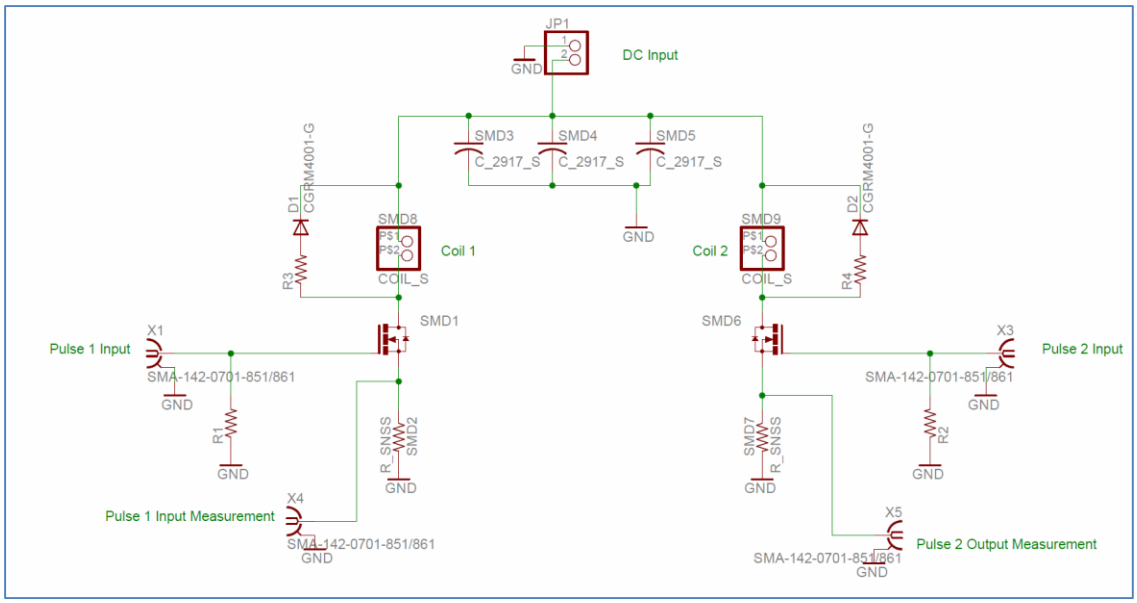

Figure A-2: Eagle PCB schematic of simulated design

The PCB design was then also performed in Eagle PCB® (Figure A-3).

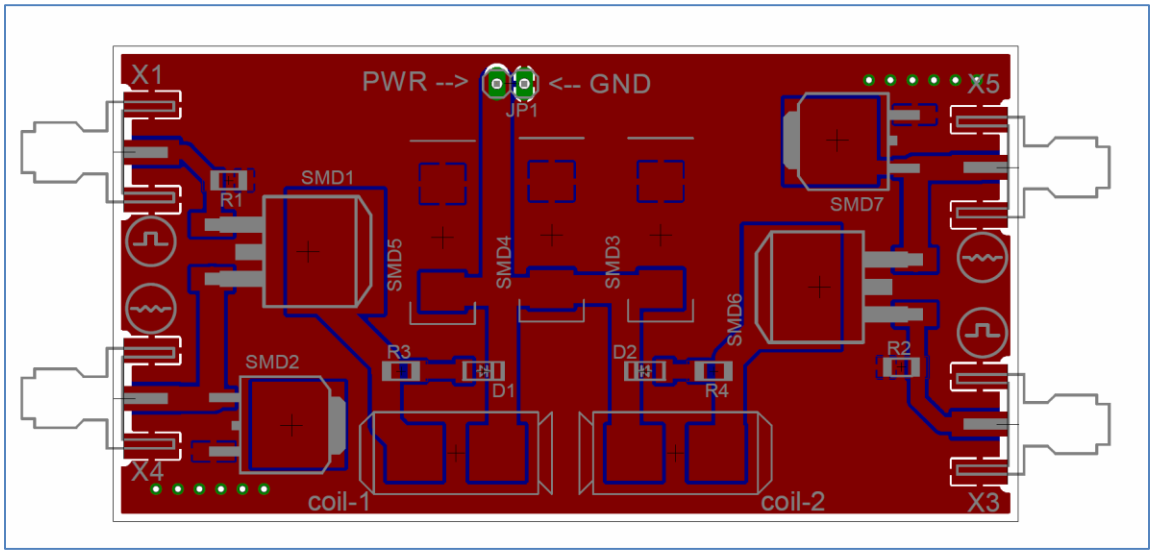

Figure A-3: Eagle PCB layout of the simulated design

Each coil will be attached to the large pads on the bottom of the board. The pulse generator inputs and current measurement inputs are labeled with appropriate symbols for ease-of-use. The DC voltage inputs are located at the top of the board and are indicated.

The board was fabricated with a Protomat S62 prototyping mill (Figure A-4).

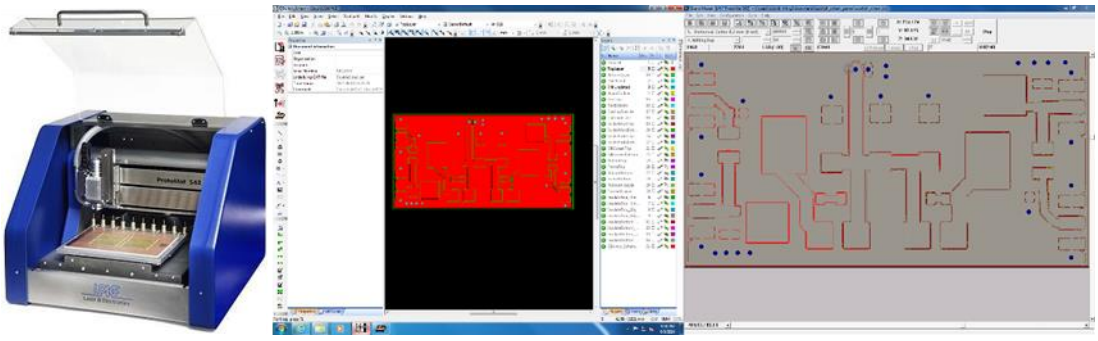

Figure A-4: Protomat S62 prototyping mill and associated software

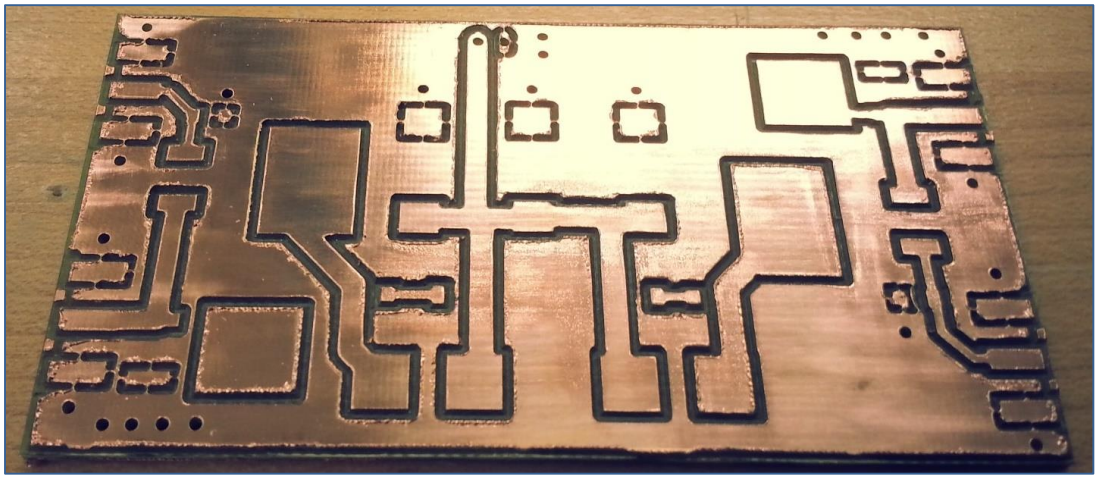

Figure A-5: The milled, unpopulated prototype MFG circuit

The PCB was populated with one MOSFET, one current sense resistor, and all other components required for a single-coil design (Figure A-5 and Figure A-6).

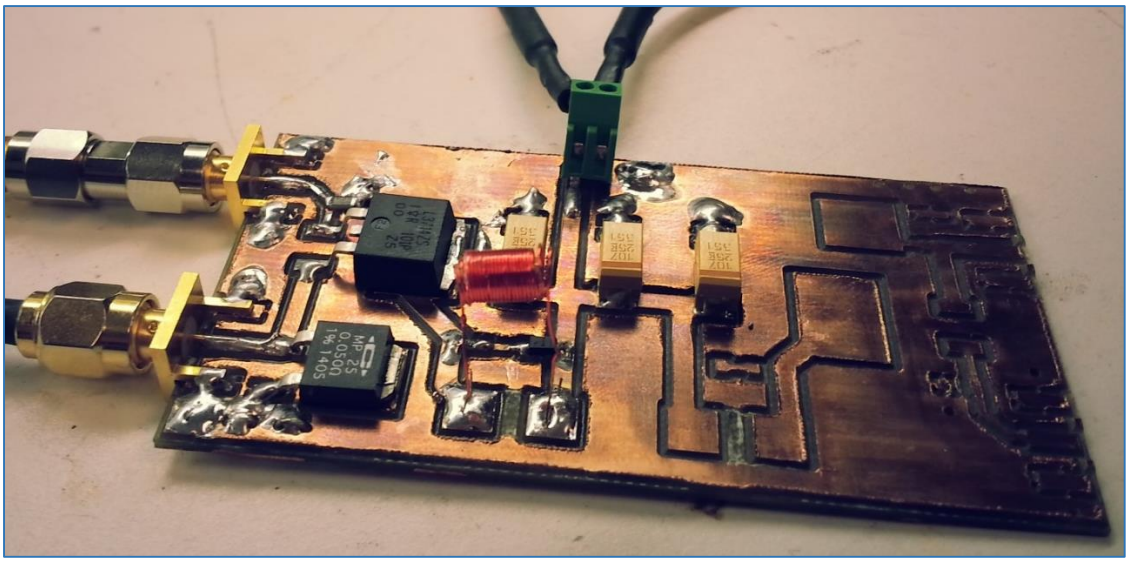

Figure A-6: The single-FET populated MFG prototype

Coil Design and Fabrication

The goal in this particular study was to create a magnetic field of 500 G. The following equation was used in the coil design estimations (magnetic flux at the center of a short coil):

$$B = \frac{\mu NI}{\sqrt{l^2+4R^2}} \quad \text{(A-1)}$$

where μ is the magnetic permeability of the medium, N is the number of coil turns, I is the current through the coil, B is the magnetic flux density, l is the length of the coil and R is the coil radius. To achieve 500 G (0.05 T) assuming a relative permeability of 1, 20-turn coil, 5.3 mm coil length, and 1.9 mm coil radius, the minimum current required is approximately 13 A.

The coil was fabricated using 28 awg wire (Figure A-7).

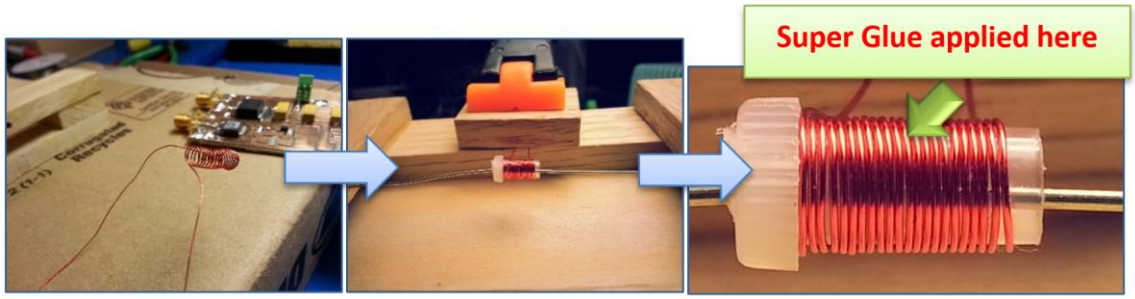

Figure A-7: Fabrication of the single coil

Electronics Testing

The electronics were tested with two different scenarios:

1. Measure output with shorted load
2. Measure output with inductive load (coil)

The current through the coil can be determined by relating the voltage measured across the current-sense resistor:

$$I_{meas} = \frac{V_{meas}}{50\ m\Omega} \quad \text{(A-2)}$$

The output for the short (left) and the coil (right) load show the effect of the coil inductance on the electronic rise and fall time (Figure A-8). Thus it can be seen here that a 1 μs pulse width can be achieved, for 3 A generated current.

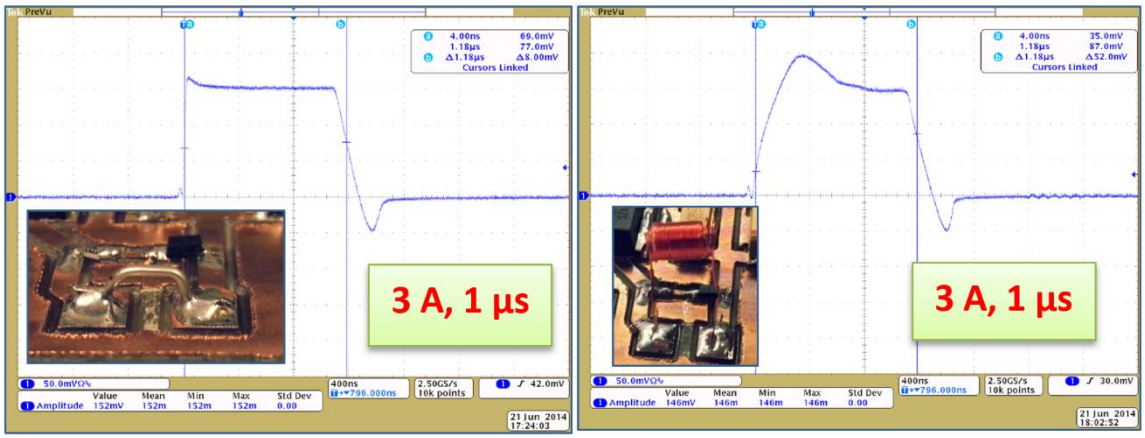

Figure A-8: Curent through shorted and inductive (coil) load

The next measurement increases the current to 23 A, and increases the pulse width to 80 µs (Figure A-9). This shows the capability of the MOSFET to provide magnetic field strengths beyond 500 G for relatively long periods of time. However, due to the inductance of the coil load the electronic rise and fall time hinder the speed of the circuit.

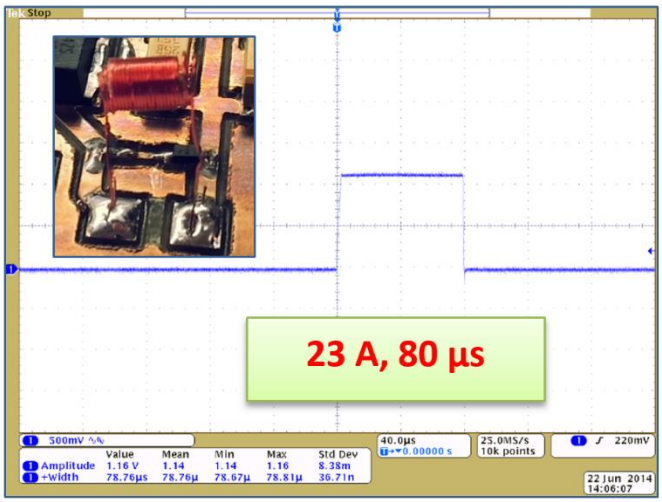

Figure A-9: Current through 20-turn coil showing 23 A for 80 µs

Test Magnetic Field in Optical Circuit

The Sagnac optical system (see subsection 2.4.2) was implemented with the latching Bi:YIG (see subsection 7.1.1) placed at the loop center, with the coil wrapped

around it. The magnetic field generator was pulsed with 23 A and 150 µs to achieve proper latched switching. The leads of the coil were manually swapped on the circuit board to reverse the applied field direction, and the field generator was pulsed again (Figure A-10). The outputs were measured and compared, and latched switching could clearly be seen.

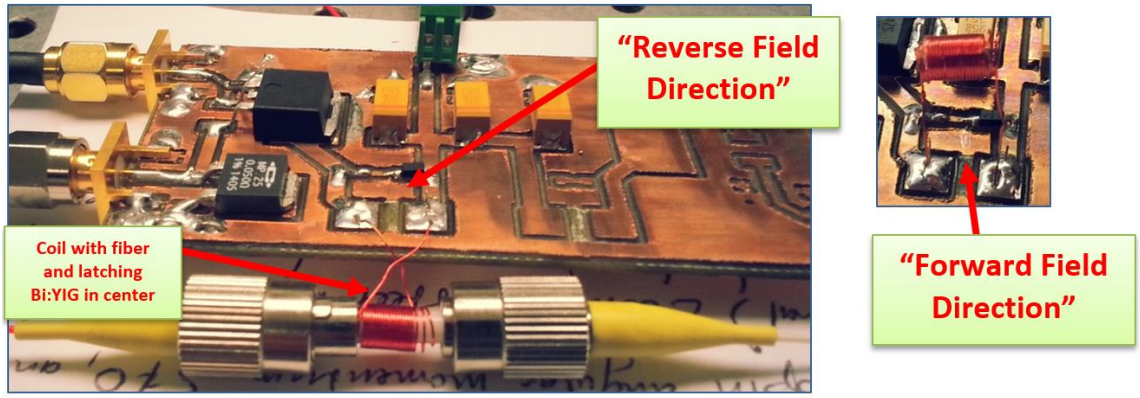

Figure A-10: Inclusion of optical setup and MO material showing application of forward and reverse direction

Output of optical circuit showed routing between ports based on magnetized direction of Bi:YIG. The results conclude that at minimum a 500 G pulse was achieved, as shown by the routed optical output (Figure A-11 and Figure A-12).

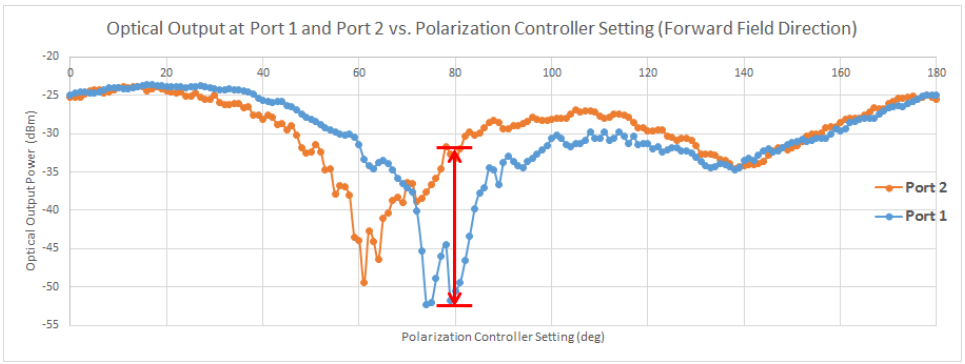

Figure A-11: Optical output showing routing to port 1

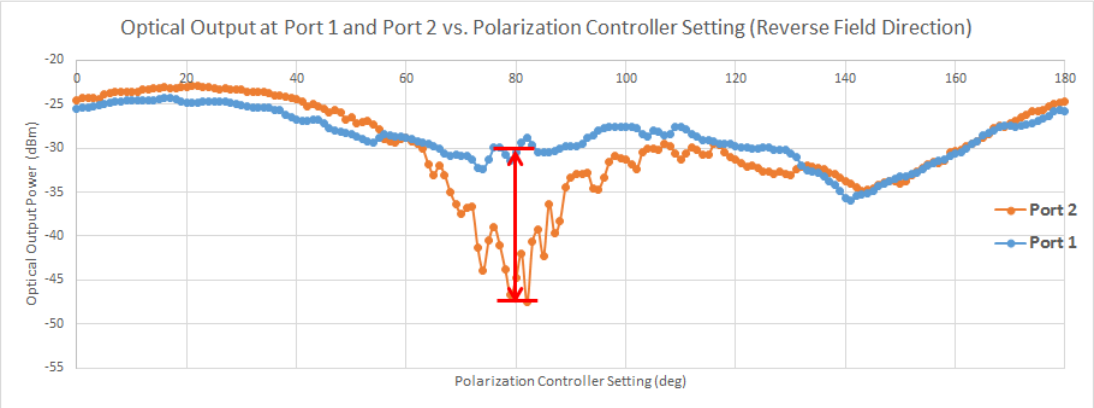

Figure A-12: Optical output showing routing to port 2

APPENDIX B

EXTENDED FORMULATION OF RESONATOR INTERFEROMETER

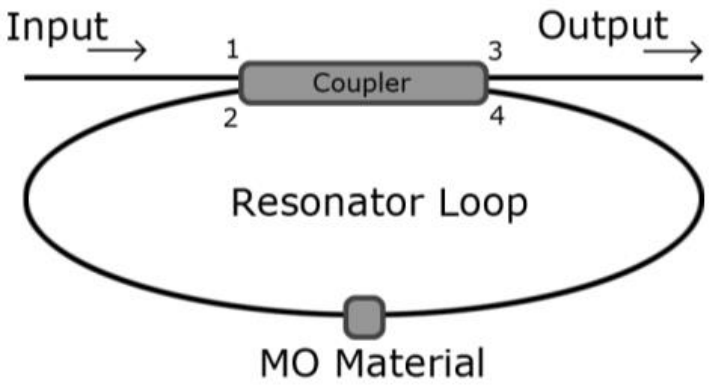

Figure B-1: Resonator Interferometer

MO Material Not Placed in Loop

Solve for the output ports (3 and 4) assuming the MO material is not included:

$$\begin{bmatrix} \vec{E}_{3o} \\ \vec{E}_{4o} \end{bmatrix} = \frac{1}{\sqrt{2}} \begin{bmatrix} 1 & j \\ j & 1 \end{bmatrix} \begin{bmatrix} \vec{E}_{1i} \\ \vec{E}_{2i} \end{bmatrix} = \frac{1}{\sqrt{2}} \begin{bmatrix} \vec{E}_{1i} + j\vec{E}_{2i} \\ j\vec{E}_{1i} + \vec{E}_{2i} \end{bmatrix} \tag{B-1}$$

So,

$$\vec{E}_{4o} = \frac{1}{\sqrt{2}} \left(j\vec{E}_{1i} + \vec{E}_{2i} \right) \tag{B-2}$$

But we need $\vec{E}_{2i}$. We know that:

$$\vec{E}_{2i} = T_1 \vec{E}_{4o} e^{j\Phi} \tag{B-3}$$

Plugging (B-2) into (B-3) gives:

$$\vec{E}_{2i} = \frac{T_1}{\sqrt{2}} \left(j\vec{E}_{1i} + \vec{E}_{2i} \right) e^{j\Phi} = \frac{jT_1}{\sqrt{2}} \vec{E}_{1i} e^{j\Phi} + \frac{T_1}{\sqrt{2}} \vec{E}_{2i} e^{j\Phi} \tag{B-4}$$

Rearranging:

$$\vec{E}_{2i} \left(1 - \frac{T_1}{\sqrt{2}} e^{j\Phi} \right) = \frac{jT_1}{\sqrt{2}} \vec{E}_{1i} e^{j\Phi} \tag{B-5}$$

Solving for $\vec{E}_{2i}$ gives:

$$\vec{E}_{2i} = \frac{\frac{jT_1 e^{j\Phi}}{\sqrt{2}}}{\left(1 - \frac{T_1}{\sqrt{2}} e^{j\Phi} \right)} \vec{E}_{1i} \tag{B-6}$$

Then,

$$\vec{E}_{3o} = \frac{1}{\sqrt{2}}\left(\vec{E}_{1i} + j\vec{E}_{2i}\right) = \frac{1}{\sqrt{2}}\left[\vec{E}_{1i} + j\frac{\frac{jT_1e^{j\Phi}}{\sqrt{2}}}{\left(1-\frac{T_1}{\sqrt{2}}e^{j\Phi}\right)}\vec{E}_{1i}\right] = \frac{1}{\sqrt{2}}\left[\vec{E}_{1i} - \frac{\frac{T_1e^{j\Phi}}{\sqrt{2}}}{\left(1-\frac{T_1}{\sqrt{2}}e^{j\Phi}\right)}\vec{E}_{1i}\right] \quad \text{(B-7)}$$

Finally,

$$\boxed{\vec{E}_{3o} = \frac{\vec{E}_{1i}}{\sqrt{2}}\left(1 - \frac{\frac{T_1e^{j\Phi}}{\sqrt{2}}}{1-\frac{T_1}{\sqrt{2}}e^{j\Phi}}\right)} \quad \text{(B-8)}$$

MO Material Placed in Loop

Solve for the output ports (3 and 4):

$$\begin{bmatrix}\vec{E}_{3o}\\ \vec{E}_{4o}\end{bmatrix} = \frac{1}{\sqrt{2}}\begin{bmatrix}1 & j\\ j & 1\end{bmatrix}\begin{bmatrix}\vec{E}_{1i}\\ \vec{E}_{2i}\end{bmatrix} \quad \text{(B-9)}$$

The wave exiting port 4 before reaching the MO is denoted by E_{4o}.

The wave entering port 2 is the following:

$$\begin{bmatrix}E_{2i,x}\\ E_{2i,y}\end{bmatrix} = T_2e^{j\Phi_2}\begin{bmatrix}E_{4o,xMO}\\ E_{4o,yMO}\end{bmatrix} = T_1T_2e^{j\Phi_1}e^{j\Phi_2}\begin{bmatrix}\cos\theta_F & -\sin\theta_F\\ \sin\theta_F & \cos\theta_F\end{bmatrix}\begin{bmatrix}E_{4o,x}\\ E_{4o,y}\end{bmatrix} =$$

$$Te^{j\Phi}\begin{bmatrix}\cos\theta_F & -\sin\theta_F\\ \sin\theta_F & \cos\theta_F\end{bmatrix}\begin{bmatrix}E_{4o,x}\\ E_{4o,y}\end{bmatrix} \quad \text{(B-10)}$$

where $E_{2i,x}$and $E_{2i,y}$ represent the x and y components of an incident wave, respectively. Here, T_1 and T_2 are the transmission coefficients between port 4 and the MO material and between the MO material and port 2, respectively. θ_F is the angle of rotation of the SOP. Φ_1 and Φ_2 are the phase changes between port 4 and the MO material and between the MO material and port 2, respectively.

Solving for E_{4o} in terms of E_{2i} gives,

$$\begin{bmatrix}E_{4o,x}\\ E_{4o,y}\end{bmatrix} = \frac{1}{Te^{j\Phi}}\begin{bmatrix}\cos\theta_F & \sin\theta_F\\ -\sin\theta_F & \cos\theta_F\end{bmatrix}\begin{bmatrix}E_{2i,x}\\ E_{2i,y}\end{bmatrix} \quad \text{(B-11)}$$

From (B-9),

$$\vec{E}_{4o} = \frac{1}{\sqrt{2}}\left(j\vec{E}_{1i} + \vec{E}_{2i}\right) \quad \text{(B-12)}$$

Thus,

$$E_{4o,x} = \frac{1}{\sqrt{2}}\left(jE_{1i,x} + E_{2i,x}\right) = \frac{1}{Te^{j\Phi}}\left(E_{2i,x}\cos\theta_F + E_{2i,y}\sin\theta_F\right) \quad \text{(B-13)}$$

$$E_{4o,y} = \frac{1}{\sqrt{2}}\left(jE_{1i,y} + E_{2i,y}\right) = \frac{1}{Te^{j\Phi}}\left(-E_{2i,x}\sin\theta_F + E_{2i,y}\cos\theta_F\right) \quad \text{(B-14)}$$

Now, we can define $\vec{E}_1$ in terms of $\vec{E}_2$:

$$jTe^{j\Phi}E_{1i,x} = \sqrt{2}E_{2i,x}\cos\theta_F + \sqrt{2}E_{2i,y}\sin\theta_F - Te^{j\Phi}E_{2i,x} \quad \text{(B-15)}$$

$$jTe^{j\Phi}E_{1i,y} = -\sqrt{2}E_{2i,x}\sin\theta_F + \sqrt{2}E_{2i,y}\cos\theta_F - Te^{j\Phi}E_{2i,y} \quad \text{(B-16)}$$

Putting in matrix form gives the following:

$$jTe^{j\Phi}\begin{bmatrix}E_{1i,x}\\E_{1i,y}\end{bmatrix} = \begin{bmatrix}\sqrt{2}\cos\theta_F - Te^{j\Phi} & \sqrt{2}\sin\theta_F\\ -\sqrt{2}\sin\theta_F & \sqrt{2}\cos\theta_F - Te^{j\Phi}\end{bmatrix}\begin{bmatrix}E_{2i,x}\\E_{2i,y}\end{bmatrix} \quad \text{(B-17)}$$

Extracting $\sqrt{2}$ gives:

$$\frac{jTe^{j\Phi}}{\sqrt{2}}\begin{bmatrix}E_{1i,x}\\E_{1i,y}\end{bmatrix} = \begin{bmatrix}\cos\theta_F - \frac{Te^{j\Phi}}{\sqrt{2}} & \sin\theta_F\\ -\sin\theta_F & \cos\theta_F - \frac{Te^{j\Phi}}{\sqrt{2}}\end{bmatrix}\begin{bmatrix}E_{2i,x}\\E_{2i,y}\end{bmatrix} \quad \text{(B-18)}$$

Solving for E_2 gives:

$$\begin{bmatrix}E_{2i,x}\\E_{2i,y}\end{bmatrix} = \frac{\frac{jTe^{j\Phi}}{\sqrt{2}}}{\left(\cos\theta_F - \frac{Te^{j\Phi}}{\sqrt{2}}\right)^2 + \sin^2\theta_F}\begin{bmatrix}\cos\theta_F - \frac{Te^{j\Phi}}{\sqrt{2}} & -\sin\theta_F\\ \sin\theta_F & \cos\theta_F - \frac{Te^{j\Phi}}{\sqrt{2}}\end{bmatrix}\begin{bmatrix}E_{1i,x}\\E_{1i,y}\end{bmatrix} \quad \text{(B-19)}$$

Solving for E_{3o} gives:

$$\vec{E}_{3o} = \frac{1}{\sqrt{2}}\left(\vec{E}_{1i} + j\vec{E}_{2i}\right) \rightarrow \begin{bmatrix}E_{3o,x}\\E_{3o,y}\end{bmatrix} = \frac{1}{\sqrt{2}}\begin{bmatrix}E_{1i,x}\\E_{1i,y}\end{bmatrix} + \frac{j}{\sqrt{2}}\begin{bmatrix}E_{2i,x}\\E_{2i,y}\end{bmatrix} \quad \text{(B-20)}$$

Replacing E_{2i} from (B-19) into (B-20) gives:

$$\begin{bmatrix}E_{3o,x}\\E_{3o,y}\end{bmatrix} = \frac{1}{\sqrt{2}}\begin{bmatrix}E_{1i,x}\\E_{1i,y}\end{bmatrix} + \frac{j}{\sqrt{2}}\frac{\frac{jTe^{j\Phi}}{\sqrt{2}}}{\left(\cos\theta_F - \frac{Te^{j\Phi}}{\sqrt{2}}\right)^2 + \sin^2\theta_F}\begin{bmatrix}\cos\theta_F - \frac{Te^{j\Phi}}{\sqrt{2}} & -\sin\theta_F\\ \sin\theta_F & \cos\theta_F - \frac{Te^{j\Phi}}{\sqrt{2}}\end{bmatrix}\begin{bmatrix}E_{1i,x}\\E_{1i,y}\end{bmatrix} \quad \text{(B-21)}$$

Rearranging:

$$\boxed{\begin{bmatrix}E_{3o,x}\\E_{3o,y}\end{bmatrix} = \frac{1}{\sqrt{2}}\begin{bmatrix}E_{1i,x}\\E_{1i,y}\end{bmatrix} - \frac{1}{\sqrt{2}}\frac{\frac{Te^{j\Phi}}{\sqrt{2}}}{\left(\cos\theta_F - \frac{Te^{j\Phi}}{\sqrt{2}}\right)^2 + \sin^2\theta_F}\begin{bmatrix}\cos\theta_F - \frac{Te^{j\Phi}}{\sqrt{2}} & -\sin\theta_F\\ \sin\theta_F & \cos\theta_F - \frac{Te^{j\Phi}}{\sqrt{2}}\end{bmatrix}\begin{bmatrix}E_{1i,x}\\E_{1i,y}\end{bmatrix}} \quad \text{(B-22)}$$

For $\theta_F = 0^0$:

$$\begin{bmatrix} E_{3o,x} \\ E_{3o,y} \end{bmatrix} = \frac{1}{\sqrt{2}} \begin{bmatrix} E_{1i,x} \\ E_{1i,y} \end{bmatrix} - \frac{1}{\sqrt{2}} \frac{\frac{Te^{j\Phi}}{\sqrt{2}}}{\left(1-\frac{Te^{j\Phi}}{\sqrt{2}}\right)^2} \begin{bmatrix} 1-\frac{Te^{j\Phi}}{\sqrt{2}} & 0 \\ 0 & 1-\frac{Te^{j\Phi}}{\sqrt{2}} \end{bmatrix} \begin{bmatrix} E_{1i,x} \\ E_{1i,y} \end{bmatrix} \quad \text{(B-23)}$$

Which gives:

$$\begin{bmatrix} E_{3o,x} \\ E_{3o,y} \end{bmatrix} = \frac{1}{\sqrt{2}} \begin{bmatrix} E_{1i,x} \\ E_{1i,y} \end{bmatrix} - \frac{1}{\sqrt{2}} \frac{\frac{Te^{j\Phi}}{\sqrt{2}}}{\left(1-\frac{Te^{j\Phi}}{\sqrt{2}}\right)} \begin{bmatrix} 1 & 0 \\ 0 & 1 \end{bmatrix} \begin{bmatrix} E_{1i,x} \\ E_{1i,y} \end{bmatrix} \quad \text{(B-24)}$$

Rearranging:

$$\begin{bmatrix} E_{3o,x} \\ E_{3o,y} \end{bmatrix} = \frac{1}{\sqrt{2}} \left(1 - \frac{\frac{Te^{j\Phi}}{\sqrt{2}}}{\left(1-\frac{Te^{j\Phi}}{\sqrt{2}}\right)} \begin{bmatrix} 1 & 0 \\ 0 & 1 \end{bmatrix} \right) \begin{bmatrix} E_{1i,x} \\ E_{1i,y} \end{bmatrix} \quad \text{(B-25)}$$

Which is the same as:

$$\boxed{\vec{E}_{3o} = \frac{\vec{E}_{1i}}{\sqrt{2}} \left(1 - \frac{\frac{Te^{j\Phi}}{\sqrt{2}}}{1-\frac{Te^{j\Phi}}{\sqrt{2}}} \right)} \quad \text{(B-26)}$$

Which is the same as the solution found without the MOFR included.